

**Ground states of κ -(ET)₂ Hg(SCN)₂Br and κ -(ET)₂ Hg(SCN)₂Cl
studied by Raman Spectroscopy and Heat Capacity measurements**

by

Nora M. Hassan

A dissertation submitted to The Johns Hopkins University in conformity with the
requirements for the degree of Doctor of Philosophy.

Baltimore, Maryland

August, 2018

© Nora M. Hassan 2018

All rights reserved

Abstract

This work is aimed at studying two isostructural materials κ -(BEDT-TTF)₂Hg(SCN)₂Br (κ -Hg-Br) and κ -(BEDT-TTF)₂Hg(SCN)₂Cl (κ -Hg-Cl), specifically elucidating the mechanism by which the electron-electron interaction gives rise to their exotic ground states. Both materials are quasi-two-dimensional organic Mott insulators on a triangular lattice which makes them highly frustrated systems. κ -Hg-Cl and κ -Hg-Br go through metal to insulator transition (MIT) at 30 K and 80 K. Studying two isostructural materials with almost identical chemical formula and only one atom replaced in the anion layer is almost equivalent to applying hydro-static pressure and thus, is useful in providing information about the effect of certain parameters on the ground states. To elucidate the magnetic ground state we study heat capacity and Raman response of single crystals of these materials. Our low temperature heat capacity measurements suggest a presence of a linear term in the temperature dependence of κ -Hg-Br, which might indicate the existence of gapless spinons. Such linear term couldn't be detected in κ -Hg-Cl, whereas both have almost identical phonon contribution. Here we demonstrate experimentally that new charge degrees of freedom emerge in the molecule-based Mott insulator κ -Hg-Br resulting in quantum dipole

ABSTRACT

liquid state. Electrons localized on molecular dimer lattice sites form electric dipoles which do not order at low temperatures and fluctuate with frequency detected experimentally in our Raman spectroscopy experiments. The heat capacity and Raman scattering response support a scenario where the composite spin and electric dipole degrees of freedom remain fluctuating down to the lowest temperatures. Raman Response of κ -Hg-Cl was very interesting and perplexing; it showed charge order at 30 K where MIT transition takes place, but at very low temperature it crosses over to another phase that seemingly changes the charge symmetry. Few mechanism are suggested but the mechanism by which this re-entrant takes place is still under investigations. Low-frequency Raman measurements were conducted to investigate magnetic excitations in both materials. No signature of magnetic excitation were detected in either materials which eliminates the possibility of anti-ferromagnetic ordering. Magnetic state is very interesting and is still under investigation by many groups active in the field.

Primary Reader: Professor Natalia Drichko

Secondary Reader: Professor Collin Broholm

Acknowledgments

I would like to express my deepest gratitude to my supervisor Professor Natalia Drichko. I wouldn't have made it this far without her support. She was not only a supervisor but an advocate and a friend that stood up for me on many occasions. She gave me advice about life as much as about science. I joined her group with no knowledge in spectroscopy, and she was very proactive in helping me learn and produce high quality data in a new field with a new technique. She directed me when it got overwhelming and was always available and patient to help solve any problems I had. I am impressed by her world class organizational skills and multi-tasking, and I am still trying to learn from her. Without the kind of supervisor and human being she is it would have been very difficult for me to reach the finish line.

I would like to express my deepest gratitude to Professor Nina Markovic who stood up for me during a crucial time of my PhD. I consider myself lucky to have joined her group. She welcomed me into her group even though I was a theoretician with no experimental background. I learned basics of experimental techniques in her lab. Her students and postdocs were my colleagues and mentors who spared no effort to bring me up to speed

ACKNOWLEDGMENTS

with experimental techniques and projects in the lab. I am grateful to Tyler Morgan-Wall; he helped me learn ebeam lithography, Postdoc Janice Wynn Guikema taught me basics of fabrication, Nikolaus Hartman trained me on synthesis and chemical vapor deposition and was the go-to-guy for helping with any problems in the lab, and finally JT Mlack for helping me take over a new project. Other colleagues I was lucky to interact with were Michael Valentine, Weiwei Lin, Allen Scheie and Wesley Fuhrman. All were very friendly, and conversation with them proved very fruitful to my research.

I am also grateful to Professor Collin Broholm, I learned a lot about heat capacity from his suggestions and his group meetings. From his group I interacted with Martin Mourigal who helped with dilution fridge measurements that proved crucial for the current work. I would like to thank my thesis committee members, Professors Oleg Tchernyshyov and Tobias Marriage for their encouragement and suggestions. I am very grateful to my masters' supervisors Professors Eugene Mishchenko and Mikhail Raikh whom I still consult and ask for advice whenever I needed to make an important decision. Their wisdom was very valuable to me.

The best time of my PhD was the time I spent with my best friends who happened to be my roommates, Shirin Jamali and Farah Hug. Shirin was my older and wiser sister; each of us lost a parent while we were roommates. Her strength of spirit and optimistic philosophy towards life was inspirational. I enjoyed the parties and trips we shared together. I and Farah got the most out of Baltimore's culinary scene; I enjoyed the restaurants and political discussions. Both are lifelong friends that I am still in touch with. I also enjoyed Tuesday

ACKNOWLEDGMENTS

dinners at Gertrude's with the condensed matter graduate students; I enjoyed conversations with Jake Mokris, Anirban Ghosh, among many others. I was lucky to have Bose as a friend, Bing Cheng as a trustworthy graduation party planner whom I had very interesting conversations about spectroscopy and career in physics. I was blessed to come across all these people who managed to make my journey through the PhD enjoyable.

Last but not least, I wouldn't have been anywhere near where I am now without my mother's hard work and resolve that I and my siblings get the best education. Her unconventional world view and strength of character gave me the opportunities that many women are deprived of. She encouraged me and my sisters to travel overseas to get an education which is extremely unusual liberal attitude towards daughters in Egypt. Without her encouragement and belief in me I wouldn't have made it or reached any of my goals. To this day I still learn from her and hope someday I will have her wisdom, strength of character, love of life and discipline.

Dedication

This thesis is dedicated to my mother

Contents

Abstract	ii
Acknowledgments	iv
List of Tables	xi
List of Figures	xii
1 Introduction	1
1.1 Research Context	1
1.2 Objective/Motivation	3
1.3 Mott Insulators	5
1.4 Quantum spin Liquids	9
2 Organic Conductors	15
3 Experimental Methods	28
3.1 Raman Spectroscopy	28

CONTENTS

3.1.1	Instrumentation	32
3.1.2	Vibrational Raman	34
3.1.3	Magnetic Raman Scattering	41
3.1.4	Experimental Procedure	49
3.2	Heat Capacity	50
3.2.1	Introduction	50
3.3	Technical Issues	55
3.3.1	Reproducibility	56
3.3.2	Sample Coupling	59
3.3.3	Effect of sample mass on measurements error	62
3.3.4	Selection of measurement parameters	64
3.3.5	Artifacts due to applied magnetic field	66
4	Study of the ground state of κ-Hg-Br	72
4.1	Introduction	72
4.2	Results: Raman scattering data	75
4.2.1	Raman Spectra of Vibrational Modes	75
4.2.2	Low-frequency Raman spectra of κ -Hg-Br and κ -Hg-Cl	79
4.3	Analysis and Discussion	80
4.4	Conclusions	87
5	Ground state of κ-Hg-Cl	91

CONTENTS

5.1	Introduction	91
5.2	Results	93
5.3	Discussion	96
6	Heat Capacity Measurements	102
6.1	Results and Discussion	103
6.1.1	κ -(ET) ₂ Cu ₂ (CN) ₃	103
6.1.2	κ -(ET) ₂ Hg(SCN) ₂ Br	106
6.1.3	κ -(ET) ₂ Hg(SCN) ₂ Cl	109
6.2	Conclusion	112
7	Summary	115
	Bibliography	118
	Vita	128

List of Tables

2.1	Parameters of the Hubbard model adapted from references ^{1,2}	18
2.2	Crystal structure data for κ -Hg-Br and κ -Hg-Cl	24
4.1	List of the parameters used in the formula Eq. 1 SI for the calculations of the line shapes presented in Fig.4.2b of the paper.	90

List of Figures

1.1	Schematic illustration of current research in hard condensed matter physics and where the work presented in this document fits within the field	3
1.2	Schematic illustration of the electron and its properties or degrees of freedom that affects the ground states of materials and phase transitions.	4
1.3	Schematic illustration of the band structure in a Mott insulator and the effect of electron-electron repulsion U on the gap opening.	8
1.4	Adapted from reference. ³ a) Shows different filling and different potential terms (U , V and V') that represent on-site, nearest neighbor and next nearest neighbor repulsion terms. b) Shows the effect of adding dimerization; transfer integrals representing hopping between lattice site are not equivalent anymore where some sites are more coupled than others leading to interesting ground states.	9
1.5	Left panel: schematic illustration of magnetic frustration within Ising model and the resultant degenerate ground state. right panel: It was shown experimentally and theoretically (within Heisenberg mode) that isotropic triangular lattice achieves long range order at 120°	12
1.6	Adapted from reference. ⁴ a) Two spins entangle forming spin singlet . b) Superposition of different configurations of short range spin entanglement. c) Long range entanglement between spins forming spin singlets. d) The creation of spinons, an excitation achieved by the breaking of a valence bond into free spins.	13
1.7	Schematic illustration of a) anisotropic triangular lattice adopted from reference. ⁵ b) ring exchange interaction. c) quantum dipole solid where electric dipole form on each dimer. d) quantum dipole liquid where charge fluctuates are rapid between molecules within a dimer, adopted from reference. ⁶	14

LIST OF FIGURES

2.1	a) The structure of quasi-two dimensional organic conductors, an array of ET molecules form the cation layer along which the conductivity is high. The cation layer alternate with the anion layer and the conductivity along the layer stacking is very low. Ref. , ⁷ b) BEDT-TTF molecule.	18
2.2	a) ab plane of κ -phase organic conductor, adapted from reference; ¹ it shows the alternating anion and cation layers. b) ac plane of κ -phase organic conductor showing that BEDT-TTF molecules are inclined with respect to lattice direction a , adapted from reference; ⁸ grey lines correspond to the anion layer, green circles correspond to the atoms of the anion layer and orange solid lines illustrate the interaction path between the S atoms in the BEDT-TTF layer and the anion layer. c) bc plane of the κ phase showing dimers where every two molecules form one dimers (circled). ¹ d) bc plane of anion layer, adapted from reference. ¹	19
2.3	a) An illustration of bonding and transfer integrals between different molecules in the κ -phase, adopted from reference. ³ b) Adopted from, ⁹ is an illustration of effective transfer integrals and corresponding exchange interaction between lattice sites	20
2.4	Adopted from reference. ³ Phase diagram of charge transfer materials and the effect of frustration and dimerization on the ground states.	21
2.5	Adapted from reference . ¹⁰ Shows the RT plot of both κ -Hg-Cl and κ -Hg-Br.	25
2.6	Adapted from reference . ⁸ RT plot of κ -Hg-Cl under pressure. At a critical pressure the MIT is suppressed.	26
2.7	Adapted from reference . ⁸ Thermal expansion measurements of κ -Hg-Cl.	27
3.1	A model of Raman scattering. A molecule absorbs a photon to a virtual state and then decays to a vibrational excited state by emitting a photon with lower frequency (Stokes lines). Another possibility with lower probability is that a molecule in an excited state absorbs a photon to a virtual state and then decays to the ground state emitting a photon with higher energies (anti-stokes lines). Elastic scattering is represented by the Rayleigh lines. Adapted from reference. ¹¹	30
3.2	How a typical Raman spectrum looks like. Data is plotted as Intensity vs. Raman shift in cm^{-1} . Adapted from reference. ¹¹	31
3.3	The major components of any Raman setup. There is the laser source, a component to disperse the scattered light and a detector. Adapted from . ¹¹	33
3.4	Shows back-scattering setup that shows the polarized incident and scattered light. Adapted from . ¹¹	33
3.5	a) Charge order in κ phase where within a dimer there is a charge rich and a charge poor molecule, adapted from Ref. ¹ b) Vibrational modes ν_2 and ν_3 and their effect on the stretching of the central C=C bonds, from Ref. ¹²	38

LIST OF FIGURES

3.6	a) Charge order in κ phase where the ν_2 is split into two bands ν_{2A} and ν_{2B} . b) A plot of charge vs. Raman shift that shows a linear relation between energy of vibration and charge on an ET molecule. (from Ref. ¹³).	39
3.7	Two-states-jump model copied from Ref. ¹²	40
3.8	Spin waves in an anti-ferromagnet copied from Ref. ¹⁴	42
3.9	Propagation of two-magnon excitation in an anti-ferromagnet, inspired by Ref. ¹⁴	44
3.10	Mechanism of two-magnon excitation due to exchange interaction, From Ref. ¹⁵	45
3.11	a) Calculation of two-magnon band in an isotropic triangular lattice in parallel (bb) and perpendicular (bc) polarization. b) Calculation of two-magnon band in a square lattice of an anti ferromagnetic material. From Ref. ¹⁶	47
3.12	a) Calculation of two-magnon band in parallel polarization and the effect of frustration J'/J on the location of the band. b) Calculation of two-magnon band in perpendicular polarization and the effect of frustration J'/J on the location of the band. From Ref. ¹⁷	48
3.13	From Reference. ¹⁸ Plot of heat capacity of Nickel. It shows different contributions to total heat capacity.	52
3.14	From Reference. ¹⁹ Plot of the setup of the puck/sample holder of the commercial PPMS. The heater increases temperate of the sample and thermometer measures the temperature. The connecting wires act as the only thermal contact with the puck frame (thermal bath).	53
3.15	a) Plot of C_p vs T of κ -(ET) ₂ Cu ₂ (CN) ₃ . The measurements was taken of the same sample at the McQueen lab at zero field and cooled at 0.5 K/min. Two curves (blue and green) show a kink at 6 K that is detected in Ref. ²⁰ The blue curve is taken on warming, the green curse is data taken on cooling. The inset is a closeup at the kink. b) Plot of κ -(ET) ₂ Hg(SCN) ₂ Cl. The blue and red curves are two measurements done at the same instrument with same sample under zero field. The inset on the right is a closeup on data points to have an estimate of random errors (around 10 mJ/mole.K). The inset on the left is a plot of C_p/T^3 vs T of the same measurements. It shows that even at very specific features, the data is very reproducible. . . .	57

LIST OF FIGURES

- 3.16 a) Plot, C_p/T vs T , of two measurements done at IQM PPMS with the same of κ -(ET)₂ Hg(SCN)₂ Cl sample with mass 1.11 mg. The second measurement (red) was re-scaled. The inset is a close up of the phase transition at 30K. b) A plot of C_p/T vs T of two different κ -(ET)₂ Hg(SCN)₂ Br samples. The inset is the raw data of the two measurements before removing the noisy data. c) Plot, C_p/T vs T , of two measurements of two different samples of κ -(ET)₂ Hg(SCN)₂ Cl. One of the measurements was taken at McQueen PPMS (date June 2016) and the other at the IQM PPMS (May 2017), at zero field. First sample was cooled at 0.5 K/min, the data was re-scaled ($\times 0.95$). Second sample was cooled at 0.5K/min in the temperature range 85K to 65K and at 1K/min at other temperatures. The inset is a plot of C_p/T^3 vs T of the feature at around 8K. The comparison shows slight changes at temperatures lower than 8K. 60
- 3.17 Plot of C_p/T vs T of two different measurements of κ -(ET)₂ Hg(SCN)₂ Cl. One of the measurements was taken at McQueen PPMS (date June 2016), blue curve, and the other at the IQM PPMS (May 2017), green curve, at zero field. First sample was cooled at 0.5 K/min. Second sample was cooled at 0.5K/min in the temperature range 85K to 65K and at 1K/min at other temperatures. b) A plot of fit parameters τ_1 and τ_2 , and the sample coupling of the data taken at IQM PPMS, green curve in plot a). c) A plot of fit parameters τ_1 and τ_2 , and the sample coupling of the data taken at McQueen PPMS, blue curve in plot a) 62
- 3.18 a) Plot of percentage of sample heat capacity relative to total heat capacity: Sample heat capacity/Total heat capacity $\times 100$ of κ -(ET)₂ Cu₂ (CN)₃ and κ -(ET)₂ Hg(SCN)₂ Br. The sample masses were 0.3 mg and 0.92 mg. The samples were cooled at 0.1 K/min at zero field. b) Comparison between two measurements of κ -(ET)₂ Cu₂ (CN)₃; red curve is a measurement of a sample of mass 0.38 mg measured in 2015 in McQueen PPMS and cooled at 0.5 K/min. The blue curve is a measurement of a sample of mass 0.2 mg measured in 2016 in IQM PPMS and cooled at 0.1 K/min. The green curve is the 2015 measurement but re-scaled by a factor of 1.17. The inset shows the same measurements but with error bars to show the significant contribution of mass error to error bars. The original data (not re-scaled) agree within the error bars. 64

LIST OF FIGURES

- 3.19 a) Plot of C_p vs T of κ -(ET)₂ Hg(SCN)₂ Br cooled at 0.5K/min in zero field. All measurements were done on the same sample, same addenda and setup at IQM PPMS. The measurements were done consequently of different temperature ranges. The data shows instability due to unknown reasons (I think mainly change in temp rise parameter). The inset is another measurement of κ -(ET)₂ Hg(SCN)₂ cooled at 0.5K/min in zero field. All measurements were done on the same sample, same addenda and setup at IQM. The three measurement were done consequentially at different temperature ranges. The major difference in the quality of the measurement could be due parameters used. b) The plot of C_p vs T of κ -(ET)₂ Hg(SCN)₂ Br is a comparison between two different measurements done on different samples. It is obvious the lack of instability and irreproducibility of some of the features (jumps) that could be attributed to either poor sample coupling or poor choice of parameters. (However, the jump in the blue curve at around 65 K was detected in another measurement of the same material at 0.1K/min and 0.5 K/min but at a much smaller scale, the jump at 120 K was not seen in any other measurement). c) Plot of C_p/T vs T of the phase transition of κ -(ET)₂ Hg(SCN)₂ Cl at 30 K. The plot of raw data to show huge difference between the heat capacity value of the first point and subsequent measurement of the same data point. The inset shows the same plot after the first point was removed. 69
- 3.20 a) Plot of C_p vs T of the phase transition of κ -(ET)₂ Hg(SCN)₂ Cl at 30 K. It compares two different cooling cycles; both measured the same sample with same addenda (was not remounted) on same setup (IQM PPMS) cooled at 10 K/min in zero field. The only difference is the measurements parameters. b) Plot of C_p/T vs T of the phase transition of κ -(ET)₂ Hg(SCN)₂ Cl at 30 K. 70
- 3.21 Plot of C_p vs T of κ -(ET)₂ Hg(SCN)₂ Cl. Same as figure above but without subtracting the first point 70
- 3.22 a) A plot of temperature vs time stamp of the raw data that is later fitted to produce heat capacity values. This figure shows the hypothetical shape of the plot in case of first order phase transition. b) Plot of temperature vs time stamp of κ -(ET)₂ Hg(SCN)₂ Br in the temperature range 70 K-to 120 K to test for first order phase transition. 71
- 3.23 Plot of C_p/T^3 vs T of addenda with and without field. The effect of the field is pronounced. 71

LIST OF FIGURES

- 4.1 (a) Schematic structure of BEDT-TTF based crystal, in the BEDT-TTF-based cation layer the molecule is highlighted in red; (b) Structure of BEDT-TTF layer in (bc) plane of κ -Hg-Cl crystal as determined from X-ray diffraction.¹ BEDT-TTF molecules are bound in dimers as highlighted by circles. These dimer sites form anisotropic triangular lattice. (c) Schematic structure of BEDT-TTF layer in a dimer Mott insulator on an anisotropic triangular lattice formed by $(\text{BEDT-TTF})_2^{+1}$ sites with $S=1/2$ (spins depicted by green arrows) and magnetic exchange between sites J_M and J'_M . The model is relevant to the spin liquid candidate κ -(BEDT-TTF)₂Cu₂(CN)₃ with $J_M/J'_M=0.64$.² (d) Schematic structure of BEDT-TTF layer in case of dipole solid (paired electron crystal²¹). Within $(\text{BEDT-TTF})_2^{+1}$ dimer sites charge-rich and charge-poor molecules are denoted by red and blue colour respectively. The dimer sites thus possess a dipole moment. J_{DC} is a magnetic interaction between spins (marked by green arrows) on neighboring charge-rich molecules. According to Ref.²¹ spins of the nearest neighbor charge-rich sites will form spin-singlets. This situation is related to κ -Hg-Cl. (e) Schematic structure of BEDT-TTF layer in case of the quantum dipole liquid. The charge is fluctuating between the molecules in $(\text{BEDT-TTF})_2^{+1}$ dimers, as denoted by blurry red and blue ovals, leading to electric dipoles fluctuation. Relevant spins also show fluctuations. This situation is related to κ -Hg-Br. 74
- 4.2 (a)-(c) Raman spectra in the region of C=C vibrations of BEDT-TTF: (a) Temperature dependence of the κ -Hg-Cl spectra in the region of ν_2 and ν_3 modes. Note the splitting of ν_2 mode in the dipole solid (charge ordered) state at 8 K with frequencies corresponding to $\text{BEDT-TTF}^{+0.4}$ and $\text{BEDT-TTF}^{+0.6}$. (b) Shape of ν_2 mode calculated by two-sites jump model, see Eq. 3.12 (SI). The upper spectrum is of a static system (ω_{ex}) with bands corresponding to $\text{BEDT-TTF}^{+0.4}$ and $\text{BEDT-TTF}^{+0.6}$ as in dipole solid state of κ -Hg-Cl. Note that on the increase of exchange frequency ω_{ex} the bands widen and move close to each other. The lower two spectra at $\omega_{ex}=30$ and 40 cm^{-1} reproduce the ν_2 shape of κ -Hg-Br at 8 and 35 K correspondingly, taking into account the natural width Γ for the relevant temperature. (c) Temperature dependence of the κ -Hg-Br spectra in the region of ν_2 and ν_3 modes. Note that the ν_2 band does not split but shows some widening at lowest temperature. (d) Temperature dependence of centerfrequency (upper panel) and line width (lower panel) for ν_2 (triangles) and ν_3 (diamonds) modes for κ -Hg-Br. Note that line width of ν_2 for κ -Hg-Br goes through a minimum at around 75 K, while it decreases continuously for ν_3 . (e) BEDT-TTF molecule with marked movements of atoms on ν_2 and ν_3 vibration. 78

LIST OF FIGURES

4.3 (a)-(b) Temperature dependence of low-frequency Raman spectra of (a) κ -Hg-Br and (b) κ -Hg-Cl in A_{1g} symmetry. Phonons are found at similar frequencies for both compounds. In the spectra of κ -Hg-Br a background develops at temperatures below 100 K. Spectra at 300 and 11 K for κ -Hg-Br for B_{1g} symmetry are shown in the inset in (a). The collective mode is observed in B_{1g} with more prominent coupling to the phonons. (c) Temperature dependence of the collective mode in A_{1g} symmetry for κ -Hg-Br determined by extracting phonons from the full Raman spectrum. The inset shows the temperature dependence of the normalized intensity of the collective mode. (d) Temperature dependence of heat capacity for κ -Hg-Cl (red line) and κ -Hg-Br (black line) below 40 K. C_p shows similar temperature dependence for these materials below 30 K. The difference in the behaviour is observed below approximately 6 K. The inset shows low temperature data with linear behaviour of heat capacity for κ -Hg-Br. (e) Raman spectra in B_{1g} polarization at 20 K in the range between 800 and 1100 cm^{-1} with phonons and luminescence background extracted for κ -(BEDT-TTF) $_2$ Cu $_2$ (CN) $_3$ (upper panel) and κ -Hg-Cl and κ -Hg-Br (lower panel). Schematic pictures of the relevant models with different charge distribution are shown. The spectra of the dimer Mott insulator on the triangular lattice κ -(BEDT-TTF) $_2$ Cu $_2$ (CN) $_3$ (upper panel) demonstrate magnetic excitations below approx. 600 cm^{-1} . This feature is absent in the spectra of both κ -Hg-Br (black) and κ -Hg-Cl (red). The increase of intensity in the spectra of κ -Hg-Br below 200 cm^{-1} is due to the collective mode fully shown in panel(a). 88

4.4 (a) Temperature dependence of parameters of ν_2 and ν_3 vibrational modes for κ -Hg-Cl. Blue line in the lower panel shows a fit of the width of ν_3 by $\Gamma(T) = \Gamma_0 + \alpha(e^{\frac{\hbar\omega_0}{k_B T}} - 1)^{-1}$, with $\Gamma_0=5.5 \text{ cm}^{-1}$, $\alpha=15$, $\omega_0=150 \text{ cm}^{-1}$. (b) Temperature dependence of (*bc*) spectra for κ -Hg-Br (upper panel) and κ -Hg-Cl(lower panel). Note a collective mode which appears at low frequencies in the spectra of κ -Hg-Br, similar to *bb* polarization. The phonons are widened by the interaction with the collective mode. (c) Comparison of temperature dependance of heat capacity of κ -Hg-Br and κ -Hg-Cl with that of κ -(BEDT-TTF) $_2$ Cu $_2$ (CN) $_3$ 89

5.1 Different Long range charge order configurations depending on V' and V , from Ref.³ 93

5.2 a) Temperature dependence of ν_2 , the measurement was taken on warming. b) Shows the three states of κ -Hg-Cl: metallic state in red, charged ordered state in green and new re-entrant state in blue. 95

5.3 a) Temperature dependence of the emv-coupled mode at 1400 cm^{-1} . b) Temperature dependence of the low frequency mode at 450 cm^{-1} 96

LIST OF FIGURES

5.4	a) Raman spectra with Lorentzian fits to the peaks. b) Temperature dependence of the frequency and widths of ν_2 , $\nu_{2(A)}$ and $\nu_{2(B)}$ peaks.	97
5.5	a) Fitting the area under the ν_2 , $\nu_{2(A)}$ and $\nu_{2(B)}$ peaks to a polynomial function. b) Fitting the efficiency factors to calculate the ratio of molecules with certain charge.	98
5.6	a) RT plot of κ -Hg-Cl from Ref. ⁸ b) Heat capacity measurement of κ -Hg-Cl under different cooling rates, 0.5K/min (blue) and 10K/min (red)	99
6.1	a) Plot of C_p vs T of κ -(ET) ₂ Cu ₂ (CN) ₃ . There is a kink at 6 K that is detected in Ref. ²⁰ b) Plot of C_p/T vs T^2 , the linear fit is shown in red.	104
6.2	a) Plot of C_p vs T of κ -(ET) ₂ Cu ₂ (CN) ₃ at two fields. b) Plot of $C_p T^{-1}$ vs T^2 at low temperatures. The data was fitted to a line with the slope equal to the lattice contribution, β , and the intercept is the Sommerfeld coefficient, γ	104
6.3	a) Plot of C_p/T vs T of κ -(ET) ₂ Cu ₂ (CN) ₃ at cooling rates: 0.1 K/min (blue), 0.5 K/min (green) and 2 K/min (red). Inset is a plot of C_p/T^3 vs T . b) Plot of C_p/T vs T^2 at cooling rates 0.1 K/min (blue), 0.5 K/min (green) and 2 K/min (red) . No significant difference is detected.	106
6.4	a) Plot of C_p/T vs T of κ -(ET) ₂ Hg(SCN) ₂ Br. Inset is a magnification of the kink at ~ 80 K. b) Plot of $C_p T^{-1}$ vs T^2 at low temperatures. The data was fitted to a line with the slope equal to the lattice contribution, β , and the intercept is the Sommerfeld coefficient, γ	107
6.5	a) Log-Log plot of C_p vs T of κ -(ET) ₂ Hg(SCN) ₂ Br at two fields. b) Plot of $C_p T^{-1}$ vs T^2 at low temperatures. The data was fitted to a line with the slope equal to the lattice contribution, β , and the intercept is the Sommerfeld coefficient, γ	108
6.6	a) Plot of C_p/T vs T of κ -(ET) ₂ Hg(SCN) ₂ Br at cooling rates 2K/min (red) and 0.1K/min (blue). b) Log-Log plot of C_p/T vs T for cooling rates 0.1K/min (blue), 0.5K/min (green) and 2K/min (red). The inset is a plot of C_p/T^3 vs T . c) Low temperature plot of C_p/T vs T^2 . The data was fitted to a line with the slope equal to the lattice contribution, β , and the intercept is the Sommerfeld coefficient, γ	108
6.7	a) Plot of C_p/T vs T of κ -(ET) ₂ Hg(SCN) ₂ Cl. Inset is a magnification of the anomaly at 30K and ~ 80 K. b) Plot of $C_p T^{-1}$ vs T^2 at low temperatures. The data was fitted to a line with the slope equal to the lattice contribution, β , and the intercept is the Sommerfeld coefficient, γ	109
6.8	a) Plot of C_p vs T of κ -(ET) ₂ Hg(SCN) ₂ Cl at cooling rate 10K/min. Measurements were done on cooling (blue) and warming (red). b) Plot of C_p vs T of κ -(ET) ₂ Hg(SCN) ₂ Cl at cooling rate 0.1K/min.	110
6.9	a) Log-Log plot of C_p vs T of κ -(ET) ₂ Hg(SCN) ₂ Cl at two fields. b) Plot of $C_p T^{-1}$ vs T^2 at low temperatures. The data was fitted to a line with the slope equal to the lattice contribution, β , and the intercept is the Sommerfeld coefficient, γ	111

LIST OF FIGURES

- 6.10 a) Plot of C_p/T vs T of κ -(ET)₂ Hg(SCN)₂ Cl at cooling rates 0.5K/min (red) and 10 K/min (blue). The inset is a close up of the anomaly due to phase transition at 30 K. b) Log-Log plot of C_p/T vs T for cooling rates 0.5K/min (red) and 10 K/min (blue). Inset is a plot of C_p/T^3 vs T for cooling rates 0.5K/min (red) and 10K/min (blue). c) Low temperature plot of C_p/T vs T^2 . The data was fitted to a line with the slope equals to the lattice contribution, β , and the intercept is the Sommerfeld coefficient, γ 111
- 6.11 a) Plot of C_p vs T of κ -(ET)₂ Hg(SCN)₂ Cl of the anomaly at 30 K at cooling rates 10K/min (red) and 0.1K/min (back). b) Same plot as a) with the two curves superimposed. 112
- 6.12 a) Plot of C_p/T vs T of κ -(ET)₂ Hg(SCN)₂ Br (blue), κ -(ET)₂ Hg(SCN)₂ Cl (green) and κ -(ET)₂ Cu₂ (CN)₃ (red). b) Plot of C_p/T^3 vs T of all three materials. c) Log-Log plot of C_p vs T of all three materials; the inset is a plot of C_p/T vs T^2 at very low temperatures. 114
- 6.13 a) Plot of C_p/T vs T of κ -(ET)₂ Hg(SCN)₂ Br (blue) and κ -(ET)₂ Cu₂ (CN)₃ (red). b) plot of C_p/T vs T^2 at very low temperatures of both materials cooled at 0.1K/min (left panel) and at 2K/min (right panel). c) Plot of C_p/T^3 vs T of both materials cooled at 0.1K/min (left panel) and at 2K/min (right panel) 114

Chapter 1

Introduction

1.1 Research Context

My research is done within the realm/paradigm of Quantum Materials in hard condensed matter. Quantum materials is rather a new term to include under its umbrella two research fields: systems with topological order and systems with electronic correlations. The two fields were united under one term because both share a theme of emergence where the aggregate properties of a many body system cannot be predicted from a reductionist understanding of the properties of the constituents or electrons, fig. 1.1. This aggregate behavior leads to the manifestation of interesting behavior that on some level have macroscopic properties [e.g. quantized magnetic flux in superconducting vortices and quantized Hall resistance] that are quantum mechanical in sense that they involve Planck's constant.

The two fields are exemplified by two important discoveries: the quantum hall effect

CHAPTER 1. INTRODUCTION

(materials with topological order/states) and high temperature superconductivity (strongly correlated materials). The first field focuses on the study of emergent behavior due to the the geometric properties or nontrivial topology of electronic wave function such as fractional quantum hall effect, topological insulators and topological superconductors to name a few. My research focuses on strongly correlated materials where the Coulomb interaction between electrons couldn't be ignored anymore. To describe these materials models are developed where electron-electron interaction term is added in the Hamiltonian. A very important example of strongly correlated materials is Mott insulators that is represented by the Hubbard model.

Strongly correlated materials have very complex phase diagrams. Electrons in solids have several degrees of freedom: charge, spin, orbital, and topological nature determined by the atomic potential on the crystal lattice structure, as illustrated in Fig. 1.2. These attributes either couple or compete to yield a zoo of degenerate ground states and complex phase diagram. Competing interactions enable the transformation of a material from one phase to another in response to weak change in external stimuli or parameter. At absolute zero, quantum phase transitions takes place because quantum fluctuations become more effective in driving the material into a new ground state. The study of strongly correlated materials leads to the prediction and discovery of new phases of matter. Therefore, the topic is under extensive research theoretically and experimentally with two main objectives:

- Discovery of new ground states or phases of matter
- Construction of phase diagrams to understand the nature and mechanism of these

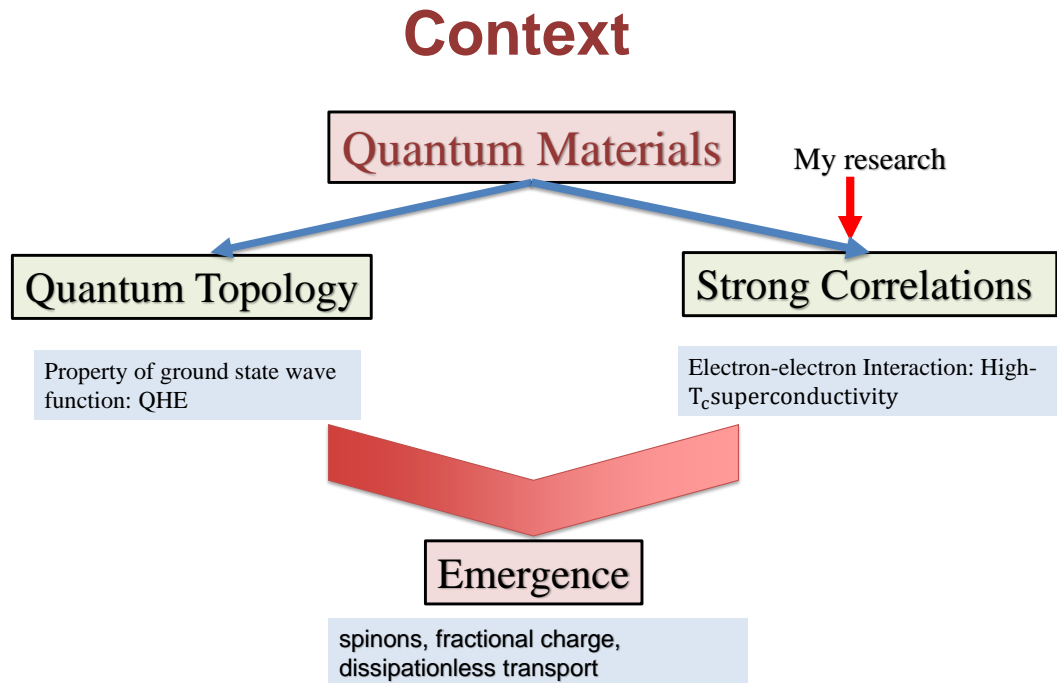


Figure 1.1: Schematic illustration of current research in hard condensed matter physics and where the work presented in this document fits within the field

phases of matter and phase transitions.

My research focuses on Mott insulators, those showing charge order and charge fluctuations/spin liquid behavior. Thus, a brief introduction about Mott insulators and spin liquids would be presented in the following subsections.

1.2 Objective/Motivation

Our motivation is to study the ground state of two isostructural organic materials for two purposes:

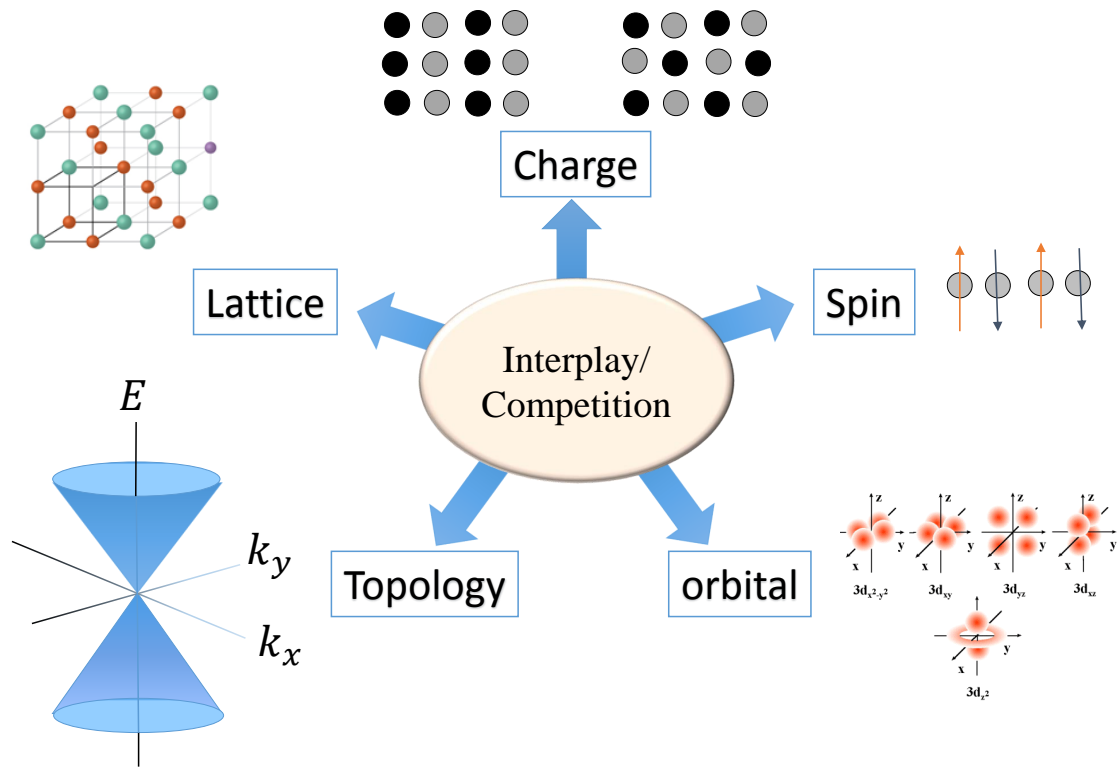


Figure 1.2: Schematic illustration of the electron and its properties or degrees of freedom that affects the ground states of materials and phase transitions.

- 1) Search for quantum spin liquid candidates among BEDT-TTF-based organic conductors
- 2) Understand the mechanism this state is achieved.

κ -Hg-Cl was found to show an unexpected charge ordered state.¹ This was the first record of charge degree of freedom in this type of organic Mott insulators. Generally κ phases are strongly dimerized and do not show charge ordered states. This result motivated the study of its iso-structural compound κ -Hg-Br. Our preliminary heat capacity results of κ -Hg-Br showed signatures of low temperatures gapless excitations that could

CHAPTER 1. INTRODUCTION

be attributed to spinons. The results were very similar to those of the spin liquid candidate κ -(BEDT-TTF)₂Cu₂(CN)₃. That lead to further in depth study of the material and its isostructural material κ -Hg-Cl to understand charge degree of freedom and its influence on magnetic properties. We used Raman spectroscopy to probe the charge degree of freedom and magnetic excitations at low temperatures.

1.3 Mott Insulators

In solid-state physics, transport properties of materials were studied using different models to predict the behavior of charge carriers in solids and give quantitative estimates of resistivity, carrier density, mobility, etc. The simplest model is the free electron model with metals were considered as a non-interacting electron gas where the interaction between the ions and the valence electrons was neglected. Such model showed success with metals but didn't explain the mechanism of insulators. So an improvement was introduced by the nearly free electron approximation where the periodic potential introduced by the ions in a crystal lattice was introduced to the Hamiltonian. In that model, the electrons were represented by Bloch wave functions that have the same periodicity as that of the underlying crystal giving rise to band structure. Energy bands consist of a large number of closely spaced energy levels that can be approximated as a continuum. There are two important bands that determine the electrical conductivity of materials: the conduction band and valence band. The conduction band houses electrons with highest energy that can move

CHAPTER 1. INTRODUCTION

freely in the material and create an electric current under the influence of electric fields. The valence band is the outermost electron orbital of an atom that electrons occupy. The energy difference between the highest occupied energy state of the valence band and the lowest unoccupied state of the conduction band is called the band gap. Materials with large band gap are insulators and those where the conduction and valence bands overlap are metals, in between are semiconductors and semi-metals. However, the band structure failed to explain a subset of insulators that are actually half filled or in other words, are metallic band structure-wise. Such Insulators are called Mott insulators and their behavior is attributed to the electron-electron interaction where the on-site repulsion between electrons, U , opens a gap at the Fermi level forming a full lower Hubbard band and an empty upper Hubbard band with band gap equal to U , see fig. 1.3. Hubbard theory is one of the simplest models to explain and study Mott insulators:

$$H_{Hubbard} = \sum_{ij,\sigma} t(c_{i\sigma}^\dagger c_{j\sigma} + H.c.) + \sum_{ij,\sigma} t'(c_{i\sigma}^\dagger c_{j\sigma} + H.c.) + U \sum_i (n_{i\uparrow} - 1/2)(n_{i\downarrow} - 1/2) \quad (1.1)$$

where t and t' denote the hopping transfer integrals between nearest neighbors and next nearest neighbors and are representations of the degree of overlap between atomic/molecular orbitals on different lattice sites. For $U \gg t, t'$; deep in Mott insulating phase, the Hubbard Model simplifies to Heisenberg Model with $J = 4t^2/U$ and $J' = 4t'^2/U$:

CHAPTER 1. INTRODUCTION

$$H_{Heisenberg} = \sum_{ij} J_{ij} \hat{S}_i \hat{S}_j \quad (1.2)$$

where J_{ij} is the exchange energy between sites i and j , $\hat{S}_i = (S_i^x, S_i^y, S_i^z) = \frac{1}{2} \sum_{\alpha\beta} c_{i\alpha}^\dagger \vec{\sigma}_{\alpha\beta} c_{i\beta}$ is the spin operator on site i and $\vec{\sigma} = (\sigma_x, \sigma_y, \sigma_z)$ is the vector of Pauli matrices.²²

Figure 1.4 from reference³ illustrates a summary of different insulating states on a lattice at $N_e/N = 1/m$ filling where N_e is the number of electrons and N is the number of lattice sites. These models go beyond the band structure and Coulomb interaction due to ions alone and include electron-electron interaction U . The on-site potential U opposes the double occupancy of a state. There is also the coulomb interaction between electrons on nearest neighbor lattice sites V . Figure 1.4 a) shows the case of a half filling with only on-site interaction U , such state represents a Mott insulator. The transfer integral t represents the hopping or kinetic energy of electrons, and the competition between U and t determines whether the material is insulator or metal; as U/t gets larger the materials goes to insulating state.

At $1/2m$ filling, $1/4$ and $1/6$ for example, the charge are not distributed equally on lattice sites leading to symmetry breaking; such charge ordered state/Wigner crystal state is another insulating state due to the interaction between electrons on different lattice sites represented by V . In short, in case of $1/2$ filling, only large on-site repulsion U achieves an insulating state. While in case of $1/4$ and other fillings, both on-site potential U and inter-site potential V cooperate to achieve an insulating state. Extended Hubbard model includes inter-site repulsion term V to model such systems.

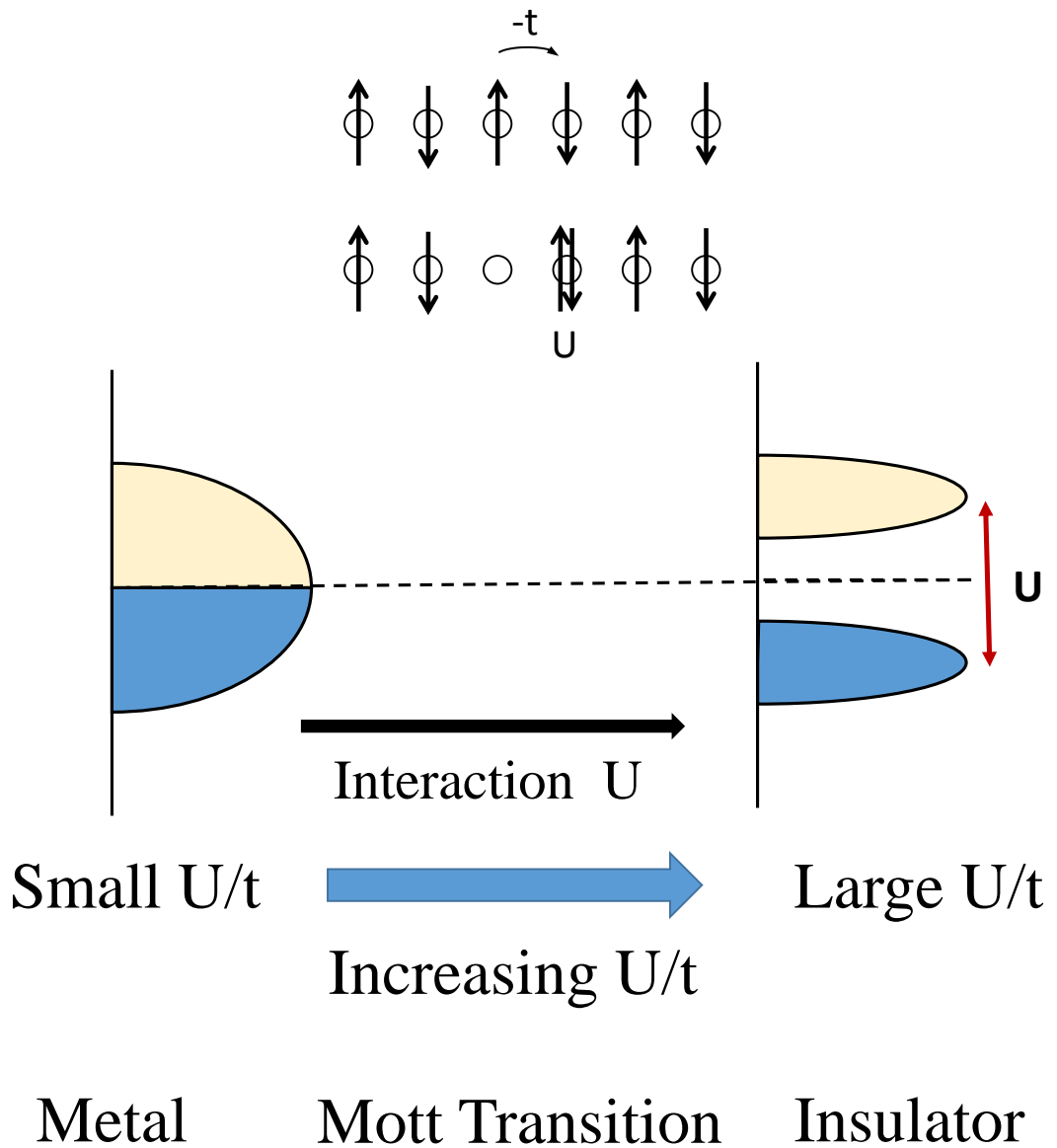


Figure 1.3: Schematic illustration of the band structure in a Mott insulator and the effect of electron-electron repulsion U on the gap opening.

Figure 1.4 b) shows the case when dimerization is included and represented by the transfer integral t_d . In such case the bonds and subsequently hopping between lattice sites are not equivalent. If $1/4$ filling is combined with dimerization we could get two states

CHAPTER 1. INTRODUCTION

depending on the relative value of inter-site interaction V and dimerization parameter t_d . In case $t_d \gg V$, the electrons within a dimer hop easily between sites such that the charge density is equally distributed within the dimer unaffected by the repulsion V due to electrons outside the dimer. In such case, the state is a dimer Mott insulator. In the second case where $V \gg t_d$, the electrons hop easily within a dimer and the effect of V from outside electrons redistributes the charge density within a dimer forming an electric dipole. Ferroelectricity takes place in the latter case where charge order and bond order are achieved to produce spontaneous ordering of electric dipoles below certain critical temperature T_c .

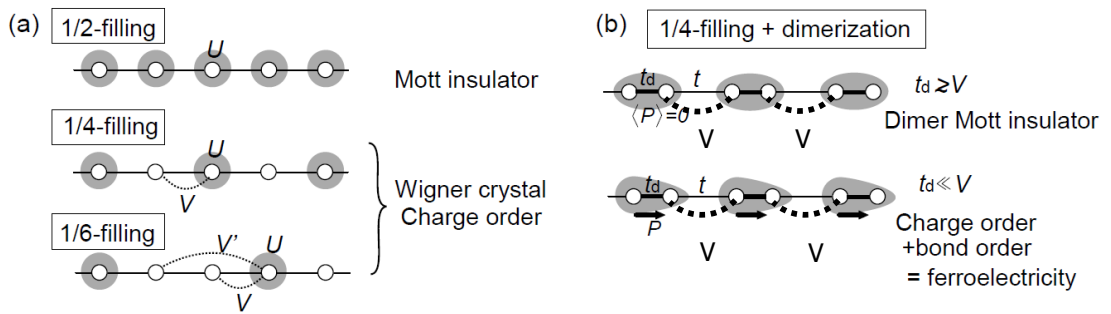


Figure 1.4: Adapted from reference.³ a) Shows different filling and different potential terms (U , V and V') that represent on-site, nearest neighbor and next nearest neighbor repulsion terms. b) Shows the effect of adding dimerization; transfer integrals representing hopping between lattice site are not equivalent anymore where some sites are more coupled than others leading to interesting ground states.

1.4 Quantum spin Liquids

Quantum spin liquids (QSL) is a new state of matter where the spins do not order at zero temperature. This state was first introduced in a published paper by P. W. Ander-

CHAPTER 1. INTRODUCTION

son²³ where the new phase is represented by Resonating Valence Bond (RVB) state. The QSL state became even more interesting when in another paper²⁴ he proposed that RVB state could explain high T_c superconductivity. QSL is a manifestation of magnetic frustration that could take place due to geometric frustration or competing exchange interaction or both. The simplest example is a 2D triangular lattice where the spin interaction is described by Ising model. Because spins has only up or down orientations with anti-ferromagnetic interaction J between spins, it is not possible to have all three spins ordered anti-ferromagnetically with respect to each other, see fig 1.5. As a result, spins tend to fluctuate even at low temperatures and fail to freeze or order. This phenomenon is called magnetic frustration. When the total spin is small, quantum fluctuations could be strong enough to allow spin fluctuations at zero temperature. This ground state is also degenerate; in fig 1.5 there are six different spin configurations that have the same energy. This phase is a disordered state with spatial symmetry. Fig1.6 shows the RVB state that mathematically models a QSL ground state. Fig 1.6 a) shows that every pair of spins entangle to form a spin-0 singlet state. Fig. 1.6 a) illustrates short range entanglement and fig. 1.6 shows long range entanglement where spins are further apart and thus, are more weakly bound. Due to frustration, the spin singlet could be formed of any pair of electrons in the lattice. As a result, the RVB ground state is superposition of all the possible states with each state describing a certain spin singlet configuration. An excitation from the ground state is the creation of a quasi-particle of zero charge and spin $1/2$ called spinon due to the breaking of a valence bond into a free spins. These low energy spinon excitations are considered the

CHAPTER 1. INTRODUCTION

smoking gun of quantum spin liquids.

It was later discovered that on a 2D isotropic triangular lattice that spins achieve long range order. Solutions of the Heisenberg model (spins are allowed to orient in any direction), proved that spins are oriented at 120° to form conventional anti-ferromagnetic state,^{25,26} see fig. 1.5 right panel.

Magnetic frustration is expected to be detected in Mott insulators because they have a localized net spin at each lattice point. Experimentally few QSL were discovered among organic conductors^{20,27-29} where the triangular lattice is anisotropic with exchange interactions J and J' . Theoretical work has been done to propose mechanisms that lead to magnetic frustration in anisotropic triangular lattice giving rise to QSL state. One theory proposed that the interplay of ring exchange and geometric frustration give rise to phase diagram where competition between classical ordered state creates QSL state.⁵ The ring exchange is represented by a permutation operator that permutes four spins around a a plaquette. Fig. 1.7 a) shows a plot of the anisotropic triangular lattice and fig. 1.7b) shows ring exchange on three different configurations of four-site plaquettes.

Another theory relevant to my work is the coexistence of quantum dipole liquid state and coupling between charge and spin.⁶ Some organic conductors exhibit ferro-electricity where electric dipoles exist on each dimer (two identical molecules linked together) and spontaneously order below T_c . Such systems are called quantum dipole solid. When electric dipoles fluctuate and fail to order at zero temperature, the material is called quantum dipole liquid. This fluctuations is due to the continuous motion of charge within a dimer.

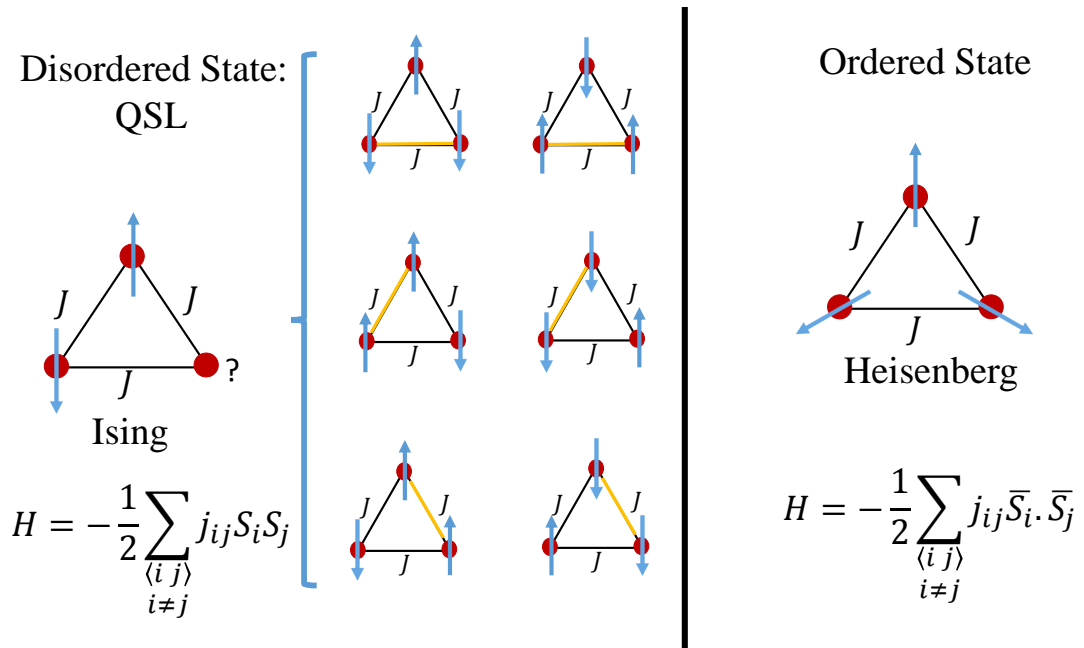


Figure 1.5: Left panel: schematic illustration of magnetic frustration within Ising model and the resultant degenerate ground state. right panel: It was shown experimentally and theoretically (within Heisenberg mode) that isotropic triangular lattice achieves long range order at 120°

Due to the coupling between the charge and spin degree of freedom, spin fail to order too down to zero temperature.

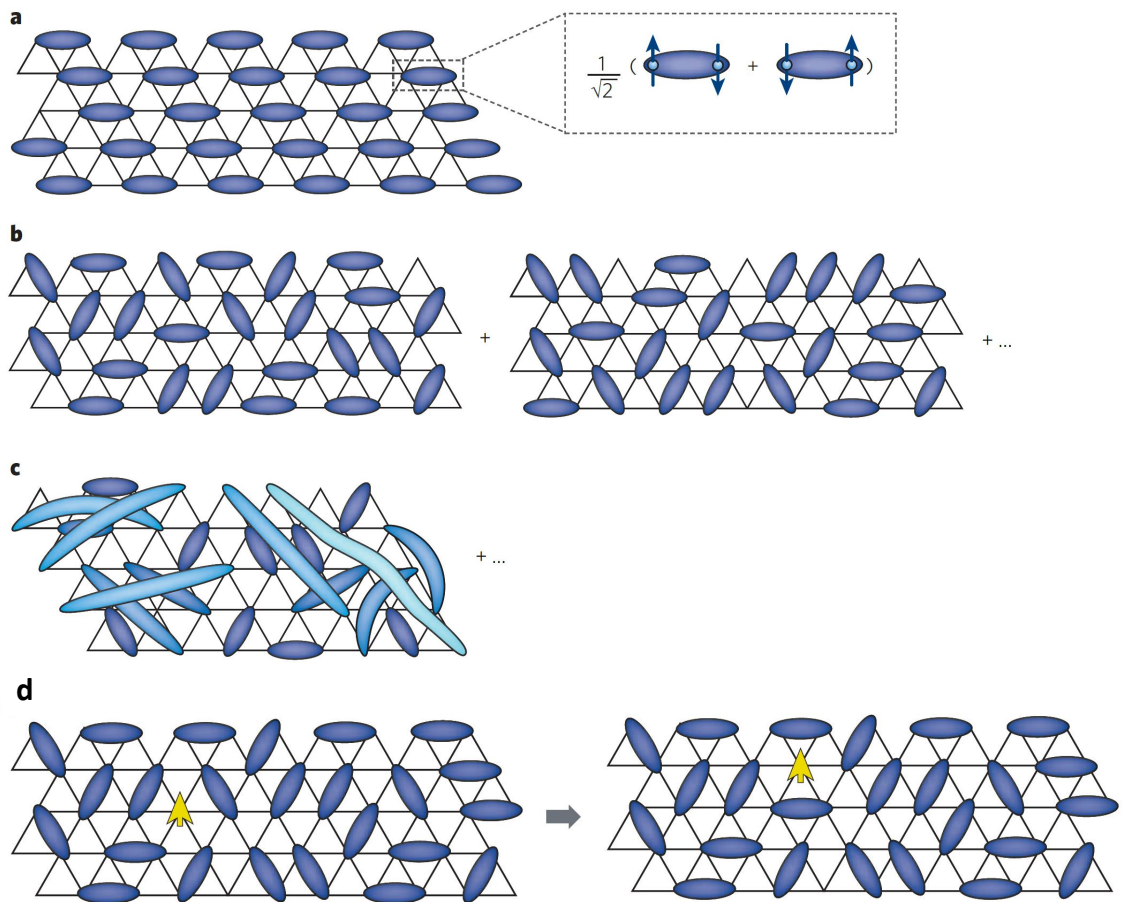


Figure 1.6: Adapted from reference.⁴ a) Two spins entangle forming spin singlet . b) Superposition of different configurations of short range spin entanglement. c) Long range entanglement between spins forming spin singlets. d) The creation of spinons, an excitation achieved by the breaking of a valence bond into free spins.

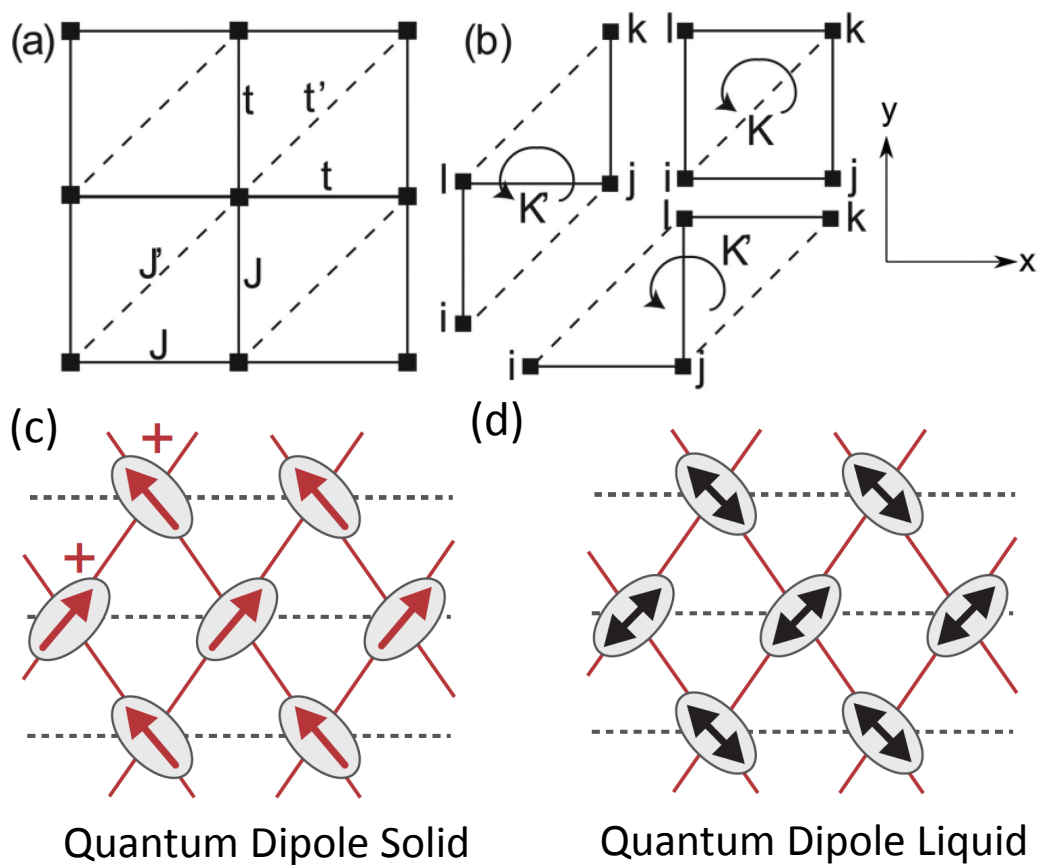


Figure 1.7: Schematic illustration of a) anisotropic triangular lattice adopted from reference.⁵ b) ring exchange interaction. c) quantum dipole solid where electric dipole form on each dimer. d) quantum dipole liquid where charge fluctuations are rapid between molecules within a dimer, adopted from reference.⁶

Chapter 2

Organic Conductors

Organic materials were mainly electrical insulators and with the discovery of the first organic 1D superconductor $(TMTSF)_2PF_6$, organic conductors started to attract a lot of attention.³⁰ Quasi-two dimensional organic conductors caught much attention recently because they were among the first strong candidates of QSL.^{20,27-29} The crystal structure is arranged in alternating layers of cations and anions with the cation layers are formed of the organic BEDT-TTF (ET) molecules, see fig.2.1 b). The conductivity is low in the direction of layer stacking and high in the layer plane and thus, these systems are considered quasi-two dimensional materials, fig.2.1a). Each BEDT-TTF molecule consists of 10 carbon,8 hydrogen and 8 sulfur atoms linked by covalent bonds, see Fig 2.1 b). There are two terminal ethylene groups on both ends of the BEDT-TTF molecule. These ethylene groups are twisted out of the molecular plane which makes the molecule in either an eclipsed or staggered conformation. The charge transfer salts generally exhibit disorder at room

CHAPTER 2. ORGANIC CONDUCTORS

temperature due to the random occurrence of both configurations while at low temperatures the staggered conformation dominates.³¹

The ET molecules within the cation layers could have different arrangements and one of the most interesting arrangement is the κ -phase, fig.2.2 c). In that arrangement, every two molecules form a dimer and every dimer donates one electron to an anion giving rise to a half filled band. Due to this half filling (one hole per lattice site), these materials are expected to be conductors. However, due to the electron-electron interaction, there is an on-site repulsion between electrons, U , that opens a gap (equal to U) at the Fermi level forming a full lower Hubbard band and an empty upper Hubbard band, giving rise to Mott insulating state. Because these materials are insulators with half-filled band, they could act as a model system of 2D triangular or square lattice of localized electrons with spin 1/2 on each lattice site. That model system is interesting because they could give rise to magnetic frustration with specific values of parameters. Fig. 2.3 shows the equivalent 2D lattice with different parameters that control the behavior of the material. Parameter t_d is the transfer integral between two molecules within a dimer, the larger the value of t_d the larger the dimerization. Parameters t_p , t_q and t_B represent transfer integral between nearest neighbor and next nearest neighbor dimers. The effective transfer integrals are calculated as follows:

$$t = t_p + t_q \quad (2.1)$$

$$t' = t_b/2 \quad (2.2)$$

CHAPTER 2. ORGANIC CONDUCTORS

Figure 2.3 shows the effective transfer integrals on the 2D lattice and how they affect the geometry of the lattice; if $t'/t \ll 1$, the lattice is square with little frustration. However; if $t'/t \sim 1$, the lattice is isotropic triangular lattice. Values of t'/t in between 0 and 1 give rise to anisotropic triangular lattice with varying degrees of geometric frustration. Magnetic frustration could be achieved through the interplay of geometric frustration and additional interactions between spins such as ring exchange. In the simplest case where geometric frustration is only included, the value of exchange interactions J and J' are calculated as follows:

$$J \approx 4t/U \quad (2.3)$$

$$J' \approx 4t'/U \quad (2.4)$$

Figure 2.4 is a phase diagram that shows the effect of transfer integrals, and electron-electron interactions U and V on the behavior of the organic charge transfer materials.³ The right axis in green shows the effect of dimerization, t_d , on the the ground state; as the dimerization increase, the ground state moves towards anti-ferromagnetic Mott insulator. As dimerization become less effective or in other words, t_d become smaller, the state is pushed towards charge ordering and ferro-electricity. The top axis in red shows the effect of frustration; in less dimerized materials, frustration is expected to push the system form charge ordered state to exotic metal state. In more dimerized systems, frustration drives Mott anti-ferromagnetic state to Spin liquid state. Few materials are given as examples on the diagram in fig. 2.4 for each of these ground states. Such phase diagrams show the

CHAPTER 2. ORGANIC CONDUCTORS

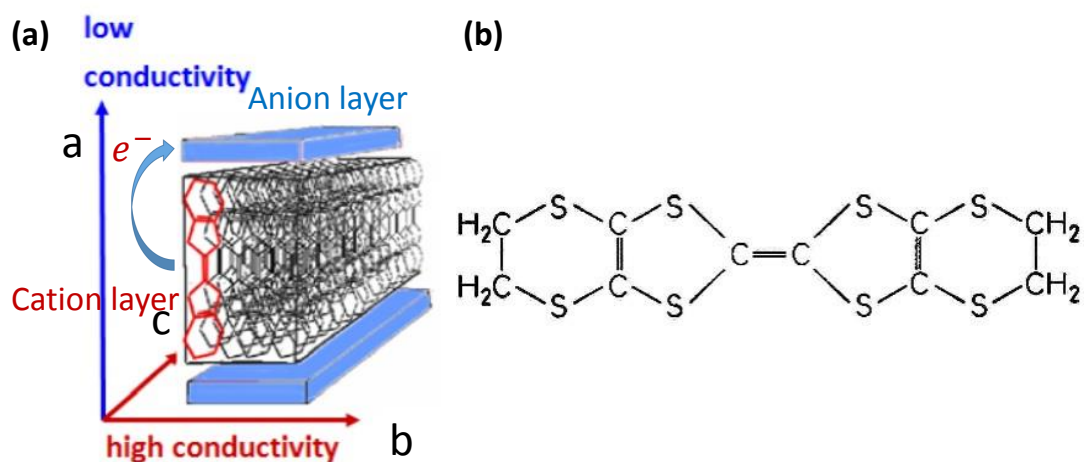


Figure 2.1: a) The structure of quasi-two dimensional organic conductors, an array of ET molecules form the cation layer along which the conductivity is high. The cation layer alternate with the anion layer and the conductivity along the layer stacking is very low. Ref. ,⁷ b) BEDT-TTF molecule.

richness of these materials where different phases or competition between ground states could be probed by applying hydro-static or chemical pressure (the substitution of one atom with another that has same chemical properties). Table 2.1 shows calculated transfers integrals for different materials using Density functional theory calculations (DFT) and the corresponding predicted ground state.

Table 2.1: Parameters of the Hubbard model adapted from references^{1,2}

Compound	t'/t	U/t	Ground state
κ -(BEDT-TTF) ₂ Cu[N(CN) ₂]Br	0.42	5.1	Superconductor
κ -(BEDT-TTF) ₂ Cu[N(CN) ₂]Cl	0.44	5.5	Antiferromagnet
κ -(BEDT-TTF) ₂ Cu ₂ (CN) ₃	0.83	7.3	Spin Liquid
κ -(BEDT-TTF) ₂ Cu(SCN) ₂	0.58	6.0	Superconductor
κ -(BEDT-TTF) ₂ Hg(SCN) ₂ Cl (300 K)	0.80	5.1	Metal
κ -(BEDT-TTF) ₂ Hg(SCN) ₂ Cl (50 K)	0.84	4.37	Quantum dipole solid?
κ -(BEDT-TTF) ₂ Hg(SCN) ₂ Br			Spin Liquid

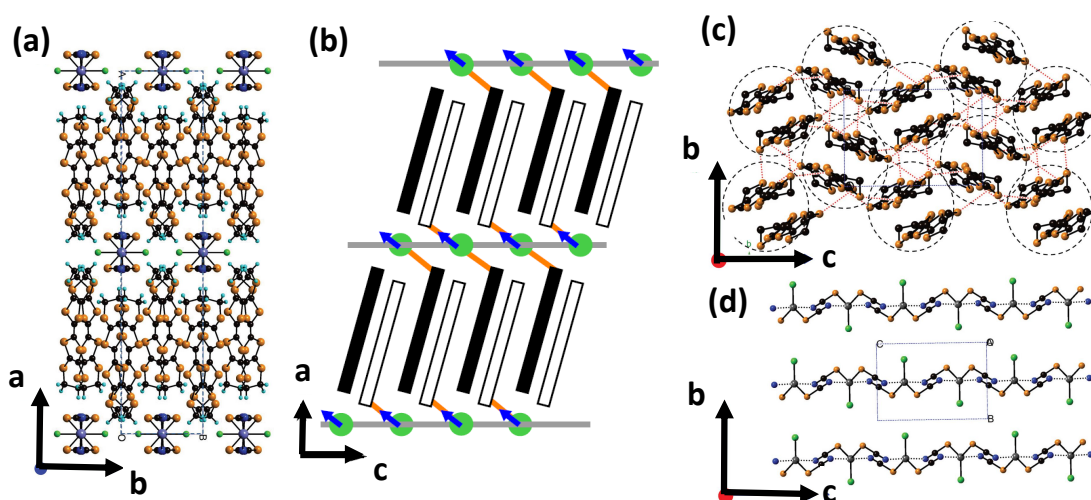


Figure 2.2: a) ab plane of κ -phase organic conductor, adapted from reference;¹ it shows the alternating anion and cation layers. b) ac plane of κ -phase organic conductor showing that BEDT-TTF molecules are inclined with respect to lattice direction a , adapted from reference;⁸ grey lines correspond to the anion layer, green circles correspond to the atoms of the anion layer and orange solid lines illustrate the interaction path between the S atoms in the BEDT-TTF layer and the anion layer. c) bc plane of the κ phase showing dimers where every two molecules form one dimers (circled).¹ d) bc plane of anion layer, adapted from reference.¹

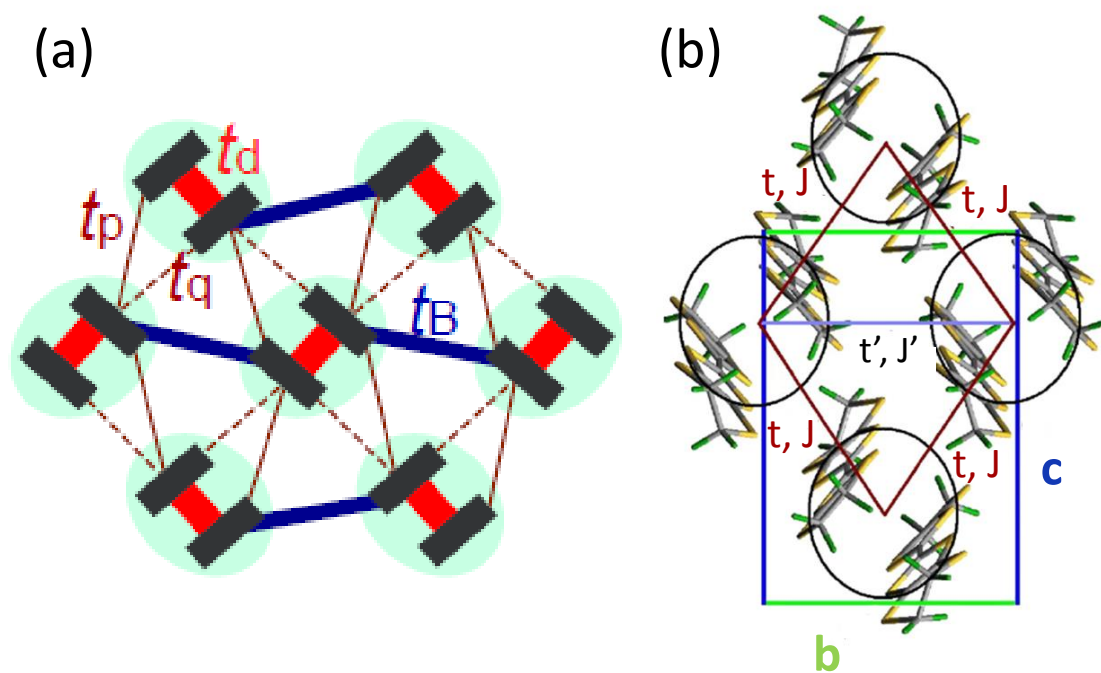


Figure 2.3: a) An illustration of bonding and transfer integrals between different molecules in the κ -phase, adopted from reference.³ b) Adopted from,⁹ is an illustration of effective transfer integrals and corresponding exchange interaction between lattice sites

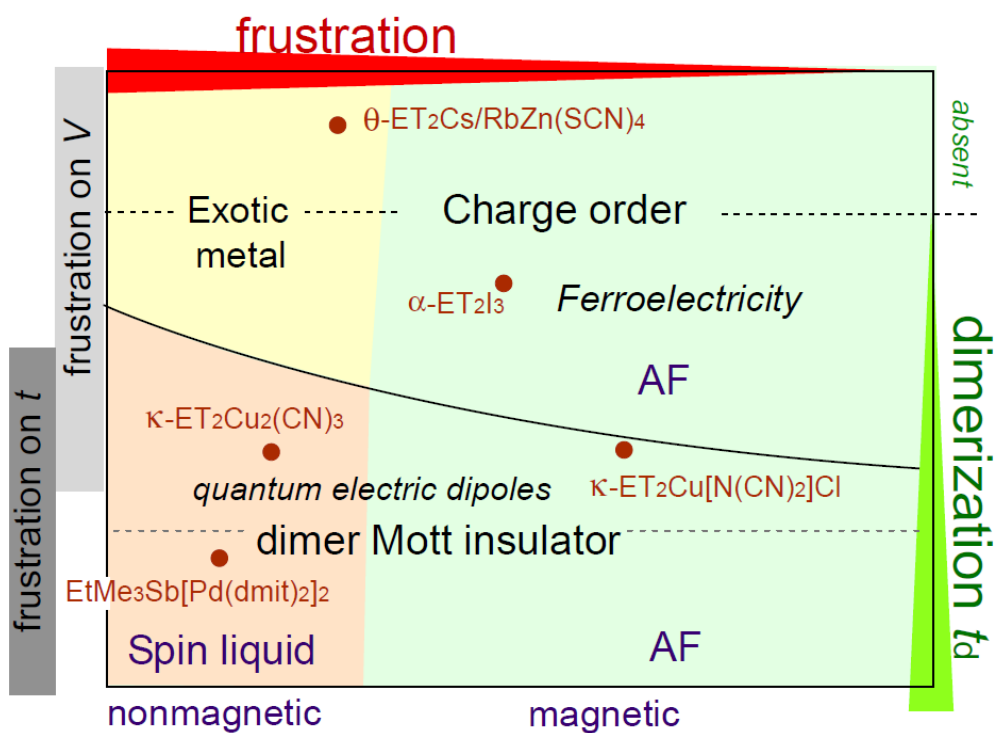


Figure 2.4: Adopted from reference.³ Phase diagram of charge transfer materials and the effect of frustration and dimerization on the ground states.

Materials under Study: κ -(ET)₂ Hg(SCN)₂ Br and κ -(ET)₂ Hg(SCN)₂ Cl

In this work I focused on the study of two isostructural Mott insulators that could be accurately modeled by a 2D triangular lattice of dimers. Crystal structures of the studied materials, κ -Hg-Br and κ -Hg-Cl were published in references .^{1,32} In Table 2.2 information about crystal structure of both structures is presented. It shows that the volume of the unit cell for κ -Hg-Br compound is somewhat larger than κ -Hg-Cl. The effect of replacing Br atom with the smaller atom Cl, called chemical substitution/pressure, is equivalent to applying hydrostatic pressure on κ -Hg-Br. Therefore, studying both materials could give us clues on the effect of pressure on transfer integrals and subsequent change of the ground state. Subsequently, helping us understand mechanism of exotic new ground states. Theoretical calculations of the electronic structure are necessary to complement experimental results and help devise models to better understand the mechanism of novel ground states.

The organic conductor κ -Hg-Br shows quite different behavior from its iso-structure κ -Hg-Cl even though they have almost identical crystal structure. Figure 2.5 shows the RT plot of both materials. κ -Hg-Br goes through metal to insulator phase transition (MIT) at 80 K while κ -Hg-Cl transitions at 30K. Figure 2.6 shows the effect of hydrostatic pressure on the RT curve of κ -Hg-Cl. It proves that applying pressure suppresses the MIT transition and at a certain critical pressure the material stays metallic. Such behavior could explain why the MIT temperature of κ -Hg-Br is higher than that of κ -Hg-Cl. However, there are

CHAPTER 2. ORGANIC CONDUCTORS

still a lot of unknowns about these materials. First, magnetic properties are still under investigation due to some contradicting results; κ -Hg-Cl was claimed to go through anti-ferromagnetic transition at around 27 K³³ but subsequent measurements failed to detect such transition.³⁴ It was speculated that it could form a spin singlet ground state but no experimental proof until now. Reference³⁵ claimed that κ -Hg-Br showed weak ferromagnetism below 20K arising from disorder. Mechanism and order of phase transition of both materials are still under debate. Even though it is agreed that κ -Hg-Cl becomes insulator due to charge order, the order of transition is under debate. Reference⁸ claims that κ -Hg-Cl goes through first order phase transition based on thermal expansion measurements, see fig. 2.7, and the existence of hysteresis in RT plots. However, we didn't find any evidence on 1st order phase transition from long pulse heat capacity measurements neither does reference³³ see such hysteresis in RT measurements. Similarly κ -Hg-Br is still under investigations to understand the the mechanism and order of the phase transition. Reference³⁵ claims that the phase transition is 1st order based on their heat capacity measurements while our measurements failed to show such 1st order transition. The mechanism by which κ -Hg-Br transitions from metallic to insulating state is still under investigation too; no Charge order or pronounced structural change could account for the phase transition and thus, it is not a simple Mott transition. It is suggested that charge and magnetic fluctuations could account for MIT transition.¹⁰ All these experiments prove that both these materials are very interesting and more experimental and theoretical studies are needed.

κ -Hg-Cl is unusual that it is a charge ordered κ phase material. Also, according to

CHAPTER 2. ORGANIC CONDUCTORS

theoretical calculations, κ -Hg-Br is expected to show high frustration with $j'/j = 0.83$ and this is a potentially good starting point for obtaining a spin liquid behavior. Thus, it is imperative to study the charge degree of freedom of these materials generally not probed or well understood with other non-spectroscopic measurements. Also, a lot of theoretical models are being developed that study the effect of charge order and its coupling with spin to understand exotic phases of matter. Our objective is to characterize κ -Hg-Br compound and understand its ground state behavior. We have performed heat capacity measurements to probe excitations at very low temperatures. Also, Raman measurements were taken to study if the compound shows a charge degree of freedom similar to that of κ -Hg-Cl. Magnetic excitations were also probed by taking low-frequency Raman measurement of the compound. The aims for studying these two systems can be summarized as follows:

- κ -Hg-Cl is a known charge ordered material. We wanted to study charge degree of freedom for a κ -phase.
- κ -Hg-Br was not studied, and was interesting as a potential spin liquid.

Table 2.2: Crystal structure data for κ -Hg-Br and κ -Hg-Cl

Formula	κ -(ET) ₂ Hg(SCN) ₂ Br (κ -Hg-Br) ³²	κ -(ET) ₂ Hg(SCN) ₂ Cl (κ -Hg-Cl) ¹
Space group	<i>C</i> 2/ <i>c</i>	<i>C</i> 2/ <i>c</i>
<i>a</i> (Å)	37.09(1)	36.9564
<i>b</i> (Å)	8.338(3)	8.2887(2)
<i>c</i> (Å)	11.738(5)	11.7503(3)
α (deg)	90	90
β (deg)	89.71	90.067
γ (deg)	90	90
<i>V</i> (Å ³)	3441 (2)	3564.29
<i>Z</i>	4	4

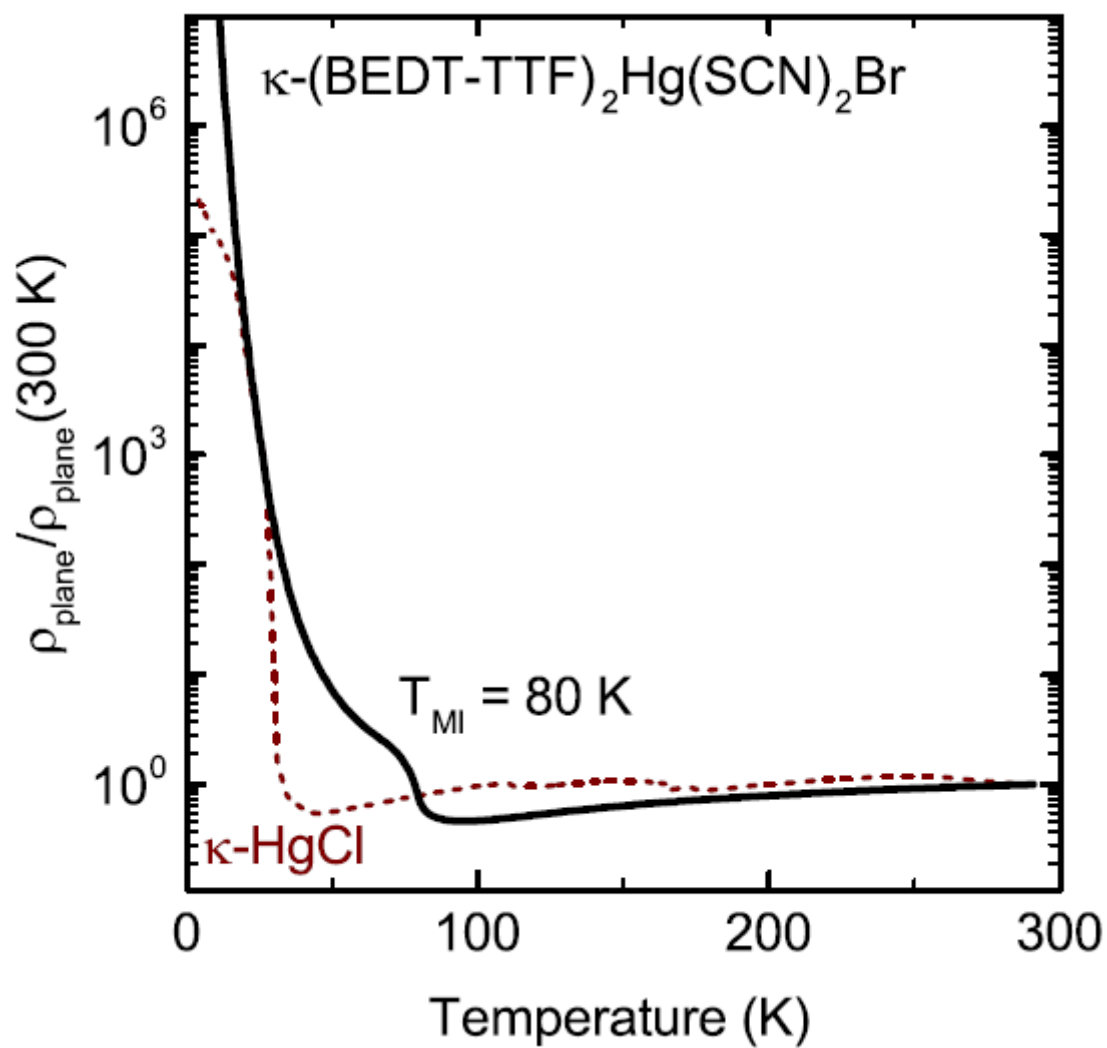


Figure 2.5: Adapted from reference .¹⁰ Shows the RT plot of bothe $\kappa\text{-Hg-Cl}$ and $\kappa\text{-Hg-Br}$.

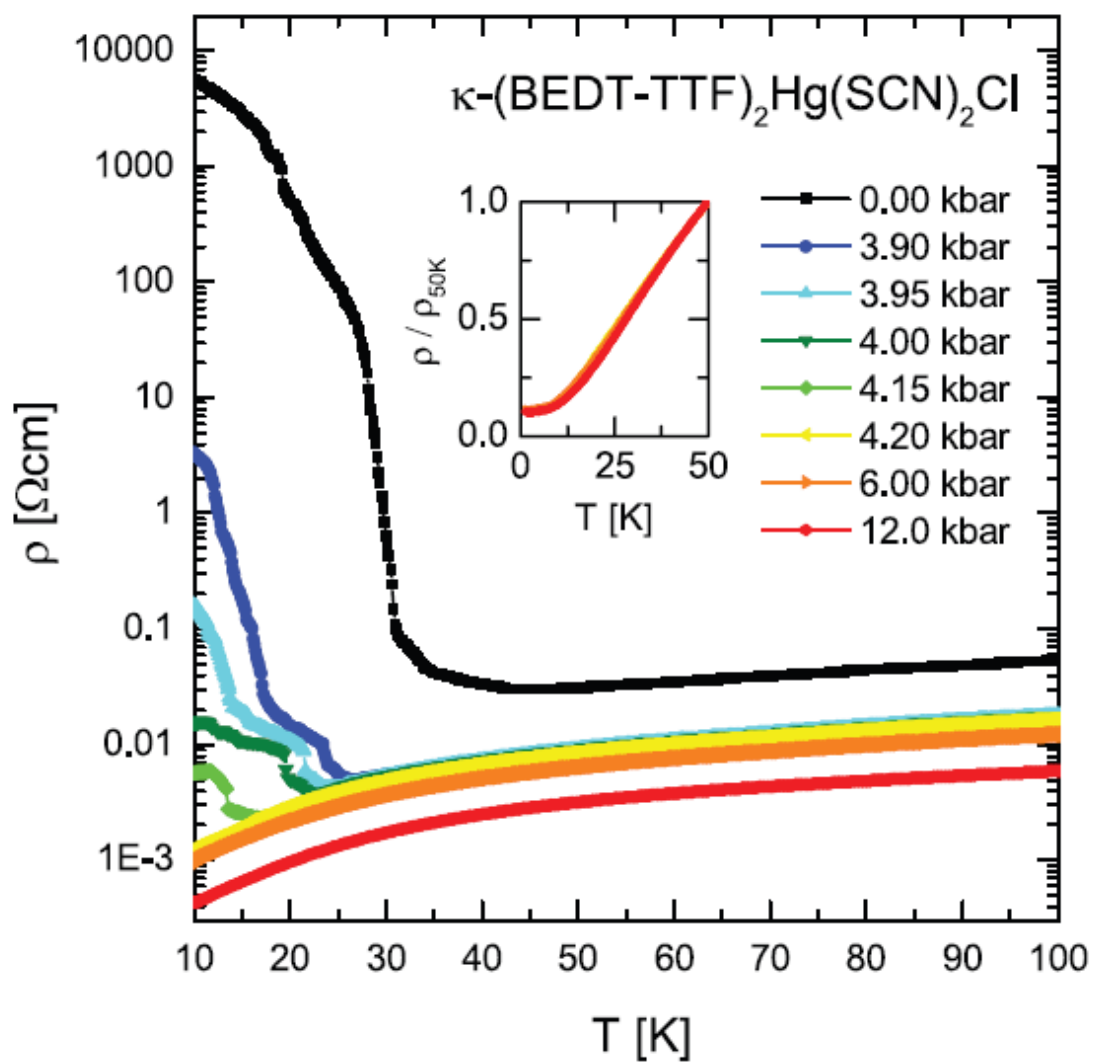


Figure 2.6: Adapted from reference .⁸ RT plot of $\kappa\text{-Hg-Cl}$ under pressure. At a critical pressure the MIT is suppressed.

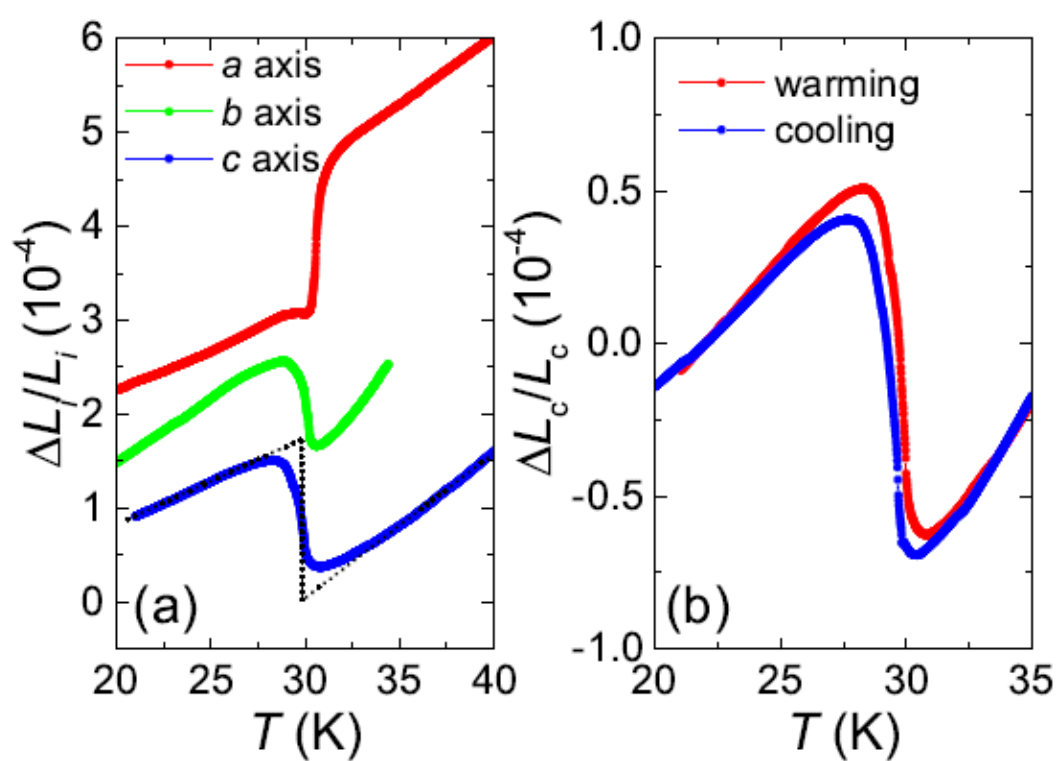


Figure 2.7: Adapted from reference .⁸ Thermal expansion measurements of κ -Hg-Cl.

Chapter 3

Experimental Methods

3.1 Raman Spectroscopy

One way of characterizing and understanding behavior of materials is through light-matter interaction. Different properties of materials could be probed by varying the frequency/energy and polarization of light and analyzing the scattered radiation. For example, elastic x-ray could be used to probe crystal structure while inelastic x-ray (Resonant inelastic X-ray scattering (RIXS)) is used to investigate the electronic structure of atoms, and in X-ray magnetic circular dichroism (XMCD), the polarization is used to probe spin and orbital magnetic moment of an atom. Raman relies on inelastic scattering of monochromatic light during which energy is transferred between photons and the sample and as a result the scattered radiation has different frequency. Generally, electromagnetic waves in the visible, near infrared, or near ultraviolet range interacts and probes molecular vibrations, phonons

CHAPTER 3. EXPERIMENTAL METHODS

or other excitations in the system. Therefore, results of Raman spectroscopy measurements are very rich; we can probe electronic excitations, vibrational modes of molecules and magnetic excitations.

When using Raman spectroscopy, a monochromatic beam of electromagnetic radiation is focused on the sample and the intensity of the scattered radiation is measured as a function of its wavelength. Fig.3.1 shows a model for the dispersion of light by molecules; a photon is absorbed by the molecule to be excited to a virtual state and then decays to a new vibrational state emitting a photon of different energy. By measuring the frequency of the scattered photon, the energy absorbed by the excitation could be calculated and plotted as excitation spectrum. Fig.3.2 shows Raman spectrum plotted as Intensity vs Raman shift or Raman wave number ω , expressed in cm^{-1} , which is the difference in frequency between the scattered light and the incident electromagnetic radiation:

$$\omega = \omega_S/c - \omega_I/c \quad (3.1)$$

Peaks in the spectrum represent excitations. Location of bands give information about the energy scale of the excitations under study, and the polarization dependence provide information about the symmetry of molecular vibrations and magnetic excitations. Raman Spectrum consists of the Rayleigh line which is due to elastic scattering contribution, Stokes lines and anti-Stokes lines due to the inelastic scattering. Stokes lines are generally more intense because lower vibrational levels are more populated than higher levels and thus, are the ones that we probe in our experiment.

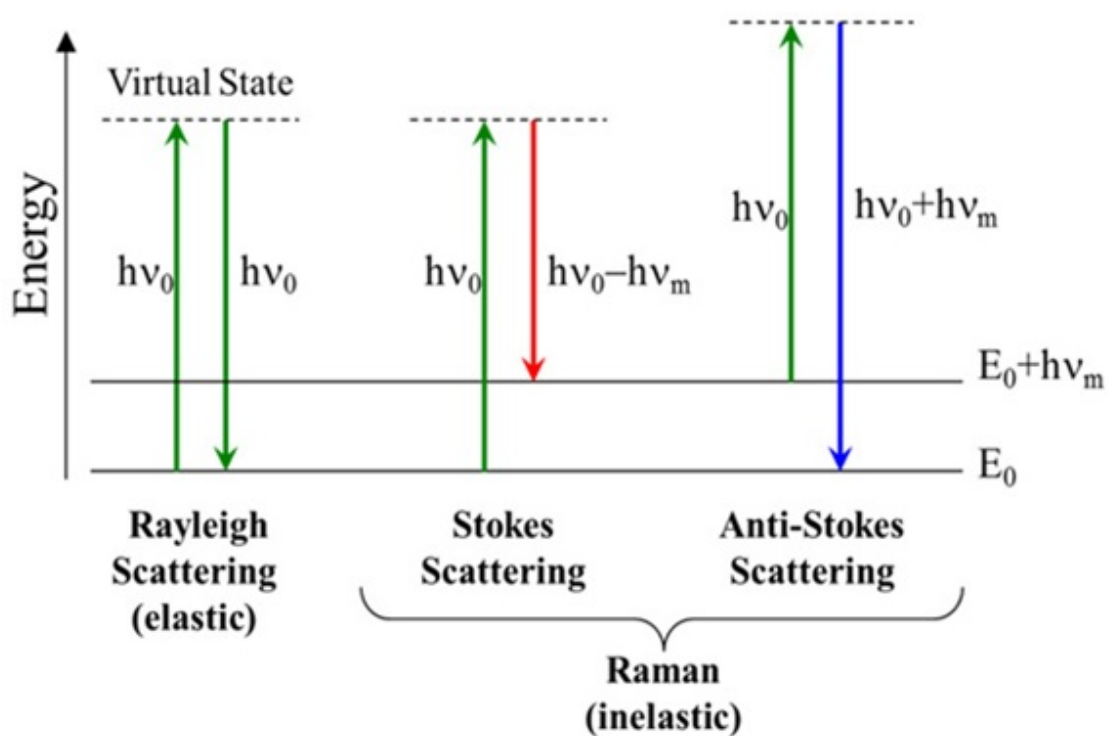


Figure 3.1: A model of Raman scattering. A molecule absorbs a photon to a virtual state and then decays to a vibrational excited state by emitting a photon with lower frequency (Stokes lines). Another possibility with lower probability is that a molecule in an excited state absorbs a photon to a virtual state and then decays to the ground state emitting a photon with higher energies (anti-stokes lines). Elastic scattering is represented by the Rayleigh lines. Adapted from reference.¹¹

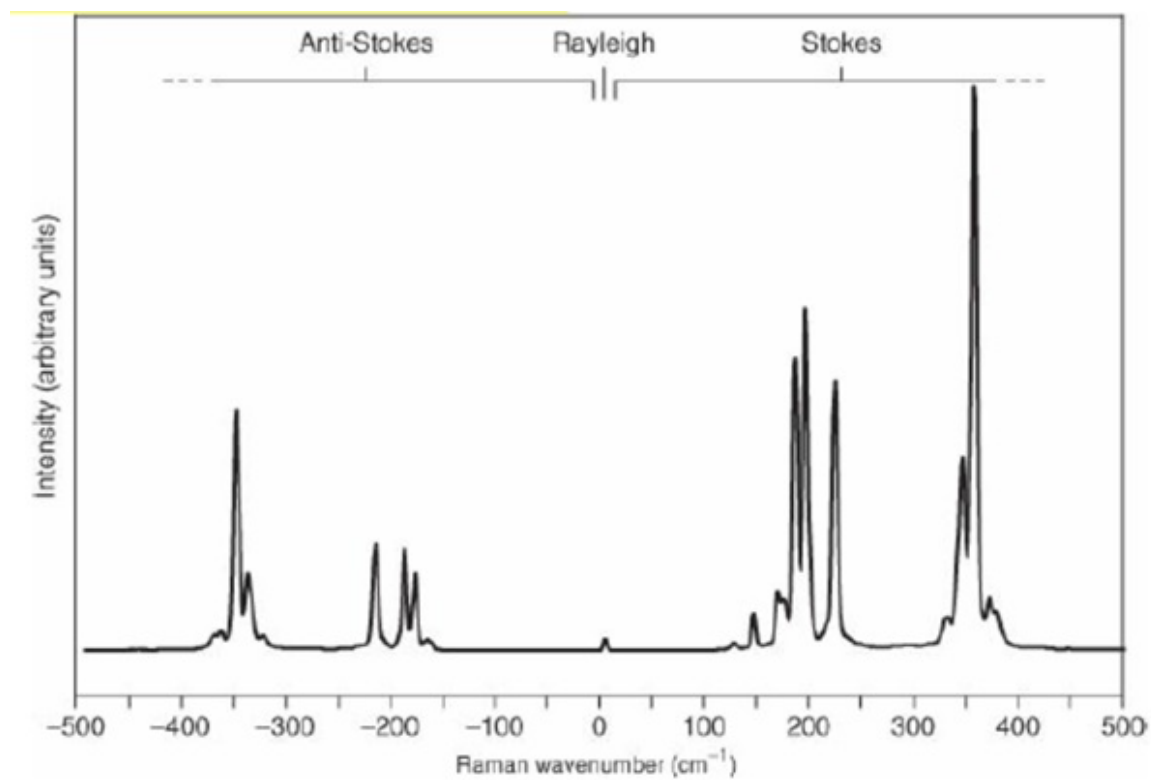


Figure 3.2: How a typical Raman spectrum looks like. Data is plotted as Intensity vs. Raman shift in cm^{-1} . Adapted from reference.¹¹

3.1.1 Instrumentation

The setup of Raman spectroscopy instruments is shown in fig. 3.3. The major components of a Raman setup are a laser source, a dispersive component and a detector. The laser is a source of polarized and coherent EM waves. The dispersive component is used to separate and resolve different frequencies spatially on a detector. A multi-channel detector such as a CCD (Charge Coupled Device) was used in our experiments. Raman setups are more complex with the involvement of many optical pieces to direct, filter and change the beam size. We used commercial spectrometer Horiba Jobin Yvon T64000 that could measure low frequencies as low as 5 cm^{-1} (0.8 meV). $\text{Ar}^+ \text{Kr}^+$ laser was used where it has 10 excitation lines from 467 nm to 647 nm. To cool down samples we used Janis cold finger micro cryostat that could go down to 4 K.

In Raman spectroscopy, there are few ways to setup the sample; we used the pseudo-Brewster angle geometry where the incident EM waves are incident on the sample at Brewster's angle. Depending on the polarization of the incident, scattered radiation and symmetry of the excitation, certain modes could be singled out to investigate. Character tables are used to determine the polarization of incident and scattered radiation to detect the mode of interest.

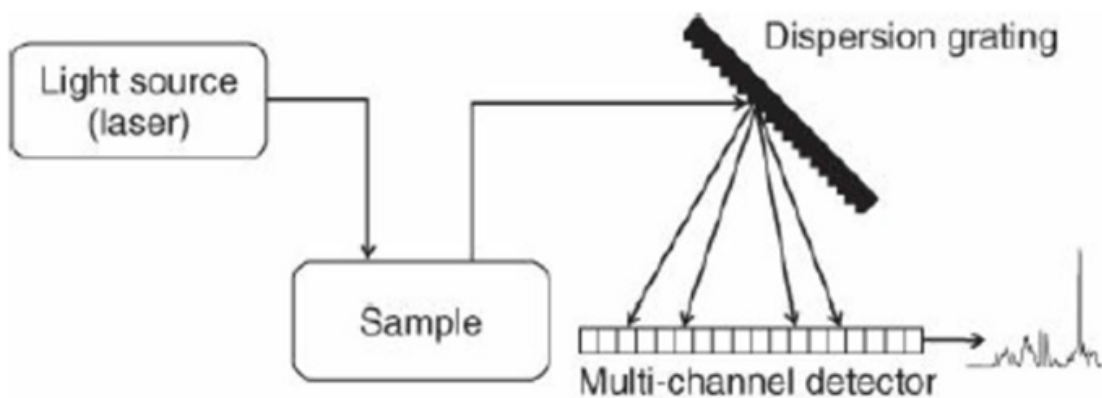


Figure 3.3: The major components of any Raman setup. There is the laser source, a component to disperse the scattered light and a detector. Adapted from .¹¹

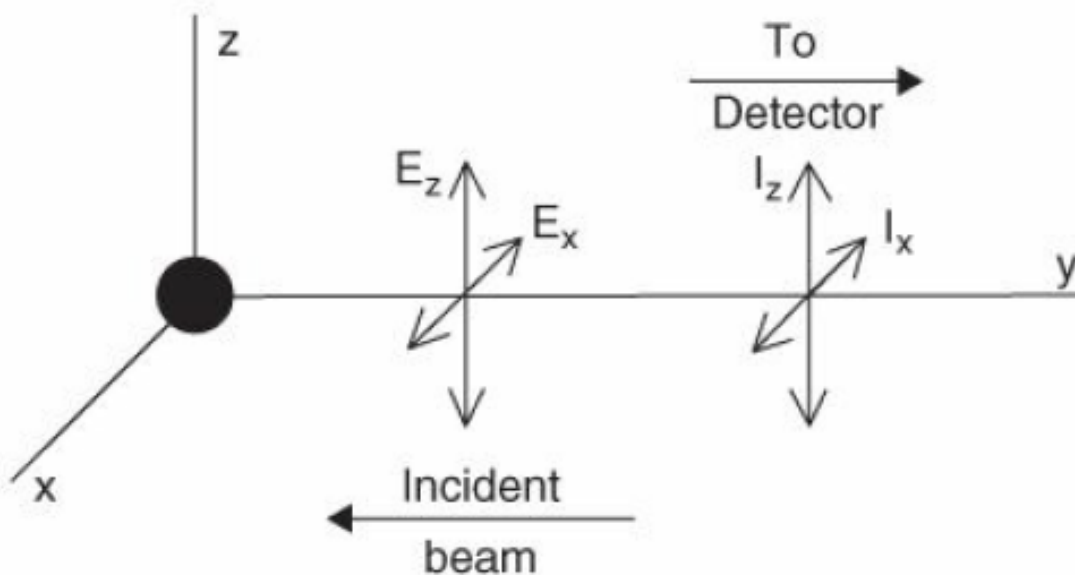


Figure 3.4: Shows back-scattering setup that shows the polarized incident and scattered light. Adapted from .¹¹

3.1.2 Vibrational Raman

According to classical theory, vibrational Raman scattering can be explained as the scattered radiation due to the change in the polarizability of the molecule as it vibrates under the influence of the oscillating electric field. When a molecule is positioned in an electrical field, an electrical dipole moment is induced. The relation between this induced dipole moment and the electrical field can be expressed as follows:¹¹

$$\mathbf{p} = \alpha \cdot \mathbf{E} + (1/2) \cdot \beta \cdot \mathbf{E}^2 + (1/6) \cdot \gamma \cdot \mathbf{E}^3 \quad (3.2)$$

where α , β and γ are the polarizability, hyper-polarizability and 2nd hyper-polarizability tensors. since $\alpha \gg \beta, \gamma$, the electric dipole could be simplified to:

$$\mathbf{p} = \alpha \cdot \mathbf{E} \quad (3.3)$$

Because the electric field is caused by an oscillating EM wave, the electric field vector can be written as

$$\mathbf{E} = \mathbf{E}_o \cdot \cos(2\pi\nu_o \cdot t) \quad (3.4)$$

where t is time and ν_o is the frequency of the EM radiation. The polarizability tensor α depends on the shape and dimensions of the chemical bonds as they change during a vibration. Therefore, the polarizability tensor α is dependent on the normal coordinate Q of the molecule. As a result, the polarizability could be expanded as Taylor series in

CHAPTER 3. EXPERIMENTAL METHODS

coordinates Q

$$\alpha = \alpha_o + \sum_k \left(\frac{\partial \alpha}{\partial Q_k} \right)_o + \frac{1}{2} \sum_{k,l} \left(\frac{\partial^2 \alpha}{\partial Q_k \partial Q_l} \right)_o \cdot Q_k \cdot Q_l + \dots \quad (3.5)$$

Q_l and Q_k are normal coordinates that change in the k^{th} and l^{th} normal vibrational modes with frequencies ν_k and ν_l . To a first approximation where all vibrational modes are independent of each other, cross terms could be ignored and only the first two terms are retained. Therefore, the equation could be reduced to:

$$\alpha_\nu = \alpha_o + \alpha'_\nu \cdot Q_\nu \quad (3.6)$$

where $\alpha'_\nu = \frac{\partial \alpha}{\partial Q_\nu}$ is the derivative of the polarizability tensor to the normal coordinate Q_ν .

If we assumed that to a first approximation the normal coordinates are those of a harmonic oscillator, the normal coordinate as a function of time can be written as:

$$Q_\nu = Q_{\nu o} \cdot \cos(2\pi \cdot \nu_\nu \cdot t + \phi_\nu) \quad (3.7)$$

where $Q_{\nu o}$ is the amplitude of vibration and ϕ_ν is the phase angle. By substitution, we get:

$$\mathbf{p} = \alpha_o \cdot \mathbf{E}_o \cdot \cos(2\pi \nu_o \cdot t) + \alpha'_o \cdot \mathbf{E}_o \cdot Q_{\nu o} \cdot \cos(2\pi \nu_o \cdot t) \cdot \cos(2\pi \nu_\nu t + \phi_\nu) \quad (3.8)$$

CHAPTER 3. EXPERIMENTAL METHODS

Applying the trigonometric formula $\cos(A) \cdot \cos(B) = 1/2[\cos(A + B) + \cos(A - B)]$ we get:

$$\begin{aligned} \mathbf{p} = & \alpha_o \mathbf{E}_o \cos(2\pi\nu_o t) \\ & + 1/2\alpha'_o \mathbf{E}_o Q_{\nu_o} \cos[2\pi(\nu_o + \nu_\nu)t + \phi_\nu] \\ & + 1/2\alpha'_o \mathbf{E}_o Q_{\nu_o} \cos[2\pi(\nu_o - \nu_\nu)t - \phi_\nu] \end{aligned} \quad (3.9)$$

Therefore, the induced dipole moment as a function of the vibrational frequencies of the incident radiations ν_o and of the molecule ν_ν is:

$$\mathbf{p} = \mathbf{p}(\nu_o) + \mathbf{p}(\nu_o + \nu_\nu) + \mathbf{p}(\nu_o - \nu_\nu) \quad (3.10)$$

where the first term is the elastic Rayleigh scattering, second term and third terms are Raman anti-Stokes and Stokes scattering. From equation 3.9, it is obvious that Raman effect only takes place when the change in polarizability with respect to coordinates is not zero; i.e.:

$$\alpha'_\nu = \left(\frac{\partial \alpha}{\partial Q_\nu} \right)_o \neq 0 \quad (3.11)$$

In reality, with more complex molecules, the polarizability term is a tensor that relates the dipole moment vector and the applied electric field. Certain tensor elements are probed when the incident and scattered are in certain polarization. Therefore, the symmetry of the molecule and vibrational mode determine the polarizability tensor and the choice of incident and scattered polarization of radiation. In our experiments, more emphasis was

CHAPTER 3. EXPERIMENTAL METHODS

placed on the temperature dependence of shape and width of Raman bands rather than their symmetry analysis. Below, I will explain what feature we were interested in and how we used Raman to probe it.

Raman Spectroscopy of BEDT-TTF molecules

Raman spectroscopy was used to probe the charge degree of freedom for κ -Hg-Br and κ -Hg-Cl. In other words, we are interested in the charge dynamics on the BEDT-TTF molecule within the cation layer. As mentioned in Chapter 2, charge order arises in 1/4 filled systems where charge is not distributed equally among lattice sites leading to broken symmetry. In the metallic state both κ -Hg-Cl, and κ -Hg-Br have uniform charge across molecules where holes are exchanged between molecules and dimers. As κ -Hg-Cl goes through MIT, charge disproportionation takes place where one molecule is charge rich and the other is charge poor within the dimer, see Fig 3.5 a). To investigate such change in the charge configuration, we probe certain vibrational modes of BEDT-TTF molecule.

BEDT-TTF is a flat molecule of 26 atoms with D_{2h} symmetry. It has 72 vibrational modes, few of which are of interest to us. The two modes we investigated were ν_2 and ν_3 , see Fig. 3.5 b). ν_2 was of particular importance to us because it is charge sensitive; this is a result of the lengthening of the central C=C bond of the molecule when more charge occupy the highest occupied molecular orbital (HOMO). The on-molecule charge is probed by measuring the frequency of the central C=C molecular bond vibration which changes by $\sim -140 \text{ cm}^{-1}$ when the charge state changes from (BEDT-TTF)⁰ to (BEDT-TTF)⁺¹.^{13,36}

CHAPTER 3. EXPERIMENTAL METHODS

Vibrational mode ν_3 however, doesn't couple to the HOMO but we follow its temperature dependence at 1470 cm^{-1} to emphasize that changes detected in ν_2 are due to charge effects only and not due to structural effects that can change the behavior of ν_3 with temperature.

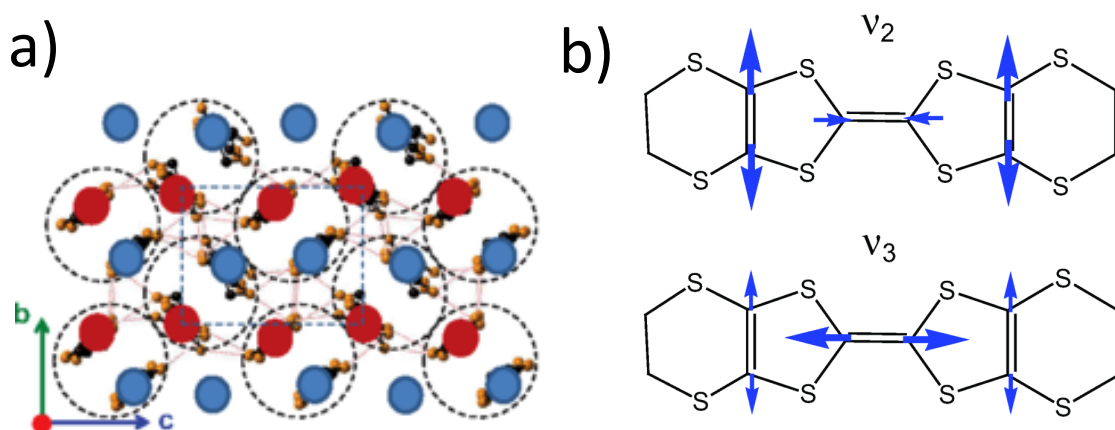


Figure 3.5: a) Charge order in κ phase where within a dimer there is a charge rich and a charge poor molecule, adopted from Ref.¹ b) Vibrational modes ν_2 and ν_3 and their effect on the stretching of the central C=C bonds, from Ref.¹²

Fig. 3.6 shows the effect of charge order on the shape of the vibrational band ν_2 . In the metallic phase ν_2 is at $\sim 1490\text{ cm}^{-1}$ and as the material is cooled down through the transition temperature, the BEDT-TTF molecules differentiate into charge rich and charge poor molecules. This charge ordering is manifested by the splitting of the ν_2 band into two bands at 1506 cm^{-1} and 1475 cm^{-1} . There is a linear relation, determined experimentally in Ref.,¹³ between the charge on the molecule and the location of the band, see fig. 3.6. Therefore, the charge rich molecule in κ -Hg-Cl at band location 1475 cm^{-1} has charge $+0.6e$ and charge poor molecule at band location 1506 cm^{-1} has charge $+0.4e$.

We used the two-state-jump model¹² to fit our Raman spectra to get an estimate of the jump rate between molecules within a dimer. The calculations of the shape of the ν_2 band

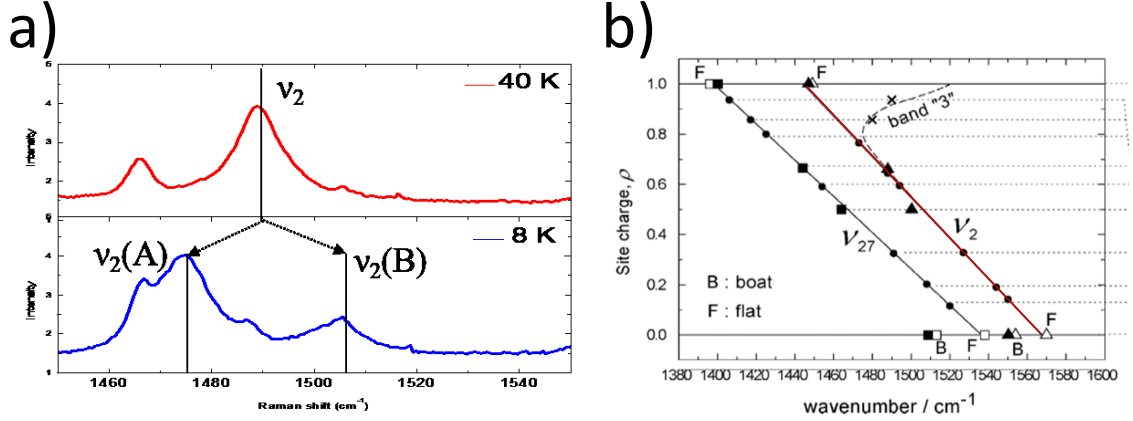


Figure 3.6: a) Charge order in κ phase where the ν_2 is split into two bands ν_{2A} and ν_{2B} . b) A plot of charge vs. Raman shift that shows a linear relation between energy of vibration and charge on an ET molecule. (from Ref.¹³).

are done using Eq. 3.12. According to the model, the shape of the ν_2 depends on ω_{EX} , the frequency of the jumps between the two states $\text{BEDT-TTF}^{+0.4}$ and $\text{BEDT-TTF}^{+0.6}$. Fig, 3.7 shows that ω_{EX} is ~ 0 in charge ordered state κ -Hg-Cl but as the frequency increases, the bands get closer and eventually at very high frequency they merge forming one broad peak. The shift of the bands from the averaged band parameter $\Delta = 16 \text{ cm}^{-1}$ is obtained using vibrational spectra in the ordered phase of κ -Hg-Cl. Γ is the natural width of the vibrational bands experimentally demonstrated in our measurements by the width of ν_3 .

$$I(\omega) \propto \text{Re} \left[\begin{pmatrix} a_R & a_P \end{pmatrix} \begin{pmatrix} i(\omega - (\omega_{1/2} - \Delta)) + \omega_{EX}/2 + \Gamma/2 & -\omega_{EX}/2 \\ -\omega_{EX}/2 & i(\omega - (\omega_{1/2} + \Delta)) + \omega_{EX}/2 + \Gamma/2 \end{pmatrix} \right] \quad (3.12)$$

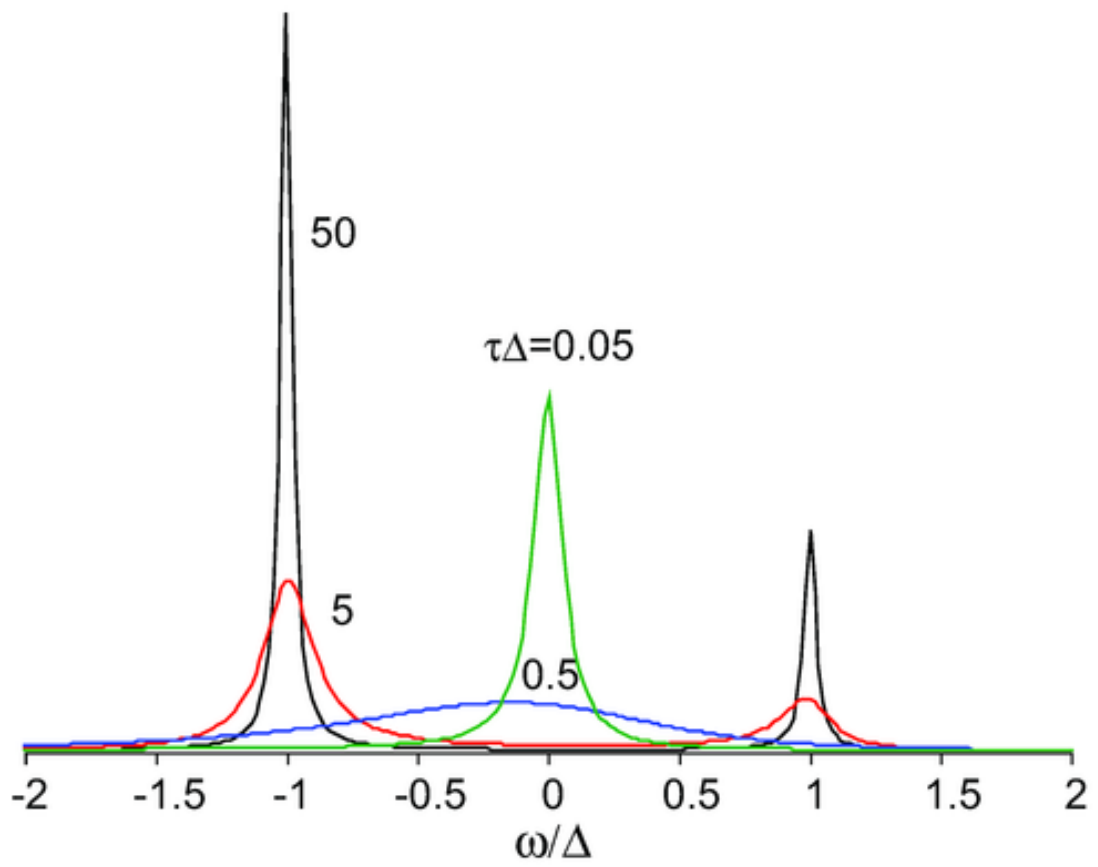


Figure 3.7: Two-states-jump model copied from Ref.¹²

3.1.3 Magnetic Raman Scattering

In last section, I introduced how inelastic Raman scattering probes molecular vibration. In this section, I will discuss how Raman scattering probes magnetic behavior of materials. In an Anti-ferromagnet, the ground state is an ordered state where every unpaired electron spin in the outermost atomic/molecular energy level is oriented opposite to the spin of electrons on nearest neighbor sites. Raman can probe low energy excitations and those excitations come in the form of spin waves, see fig. 3.8. Those waves are low energy propagating disturbances in the long range order of spin. These collective excitations are quantized to form quasi-particles called magnon. Magnons carry a certain amount of energy ω and momentum \mathbf{q} , and have spin-1. Raman scattering can not detect magnons directly; inelastic scattering probes electric dipole transitions by changing the polarizability of the molecule. Therefore, magnons are detected indirectly through two mechanisms:

- 1) spin-orbit coupling (first order magnetic scattering; main mechanism of one-magnon scattering).
- 2) Exchange interaction (2nd order magnetic scattering; main mechanism of two-magnon scattering).

The first mechanism is not relevant to my work because organic conductors have very weak spin-orbit coupling and in addition to that, 1st order magnetic scattering has lower intensity than two-magnon scattering. In the two-magnon interaction, two spins are exchanged leaving the system at an excited state. Because the momentum introduced by Raman radiation is very small $K_I - K_S \approx 0$ and total momentum is conserved, the two-

CHAPTER 3. EXPERIMENTAL METHODS

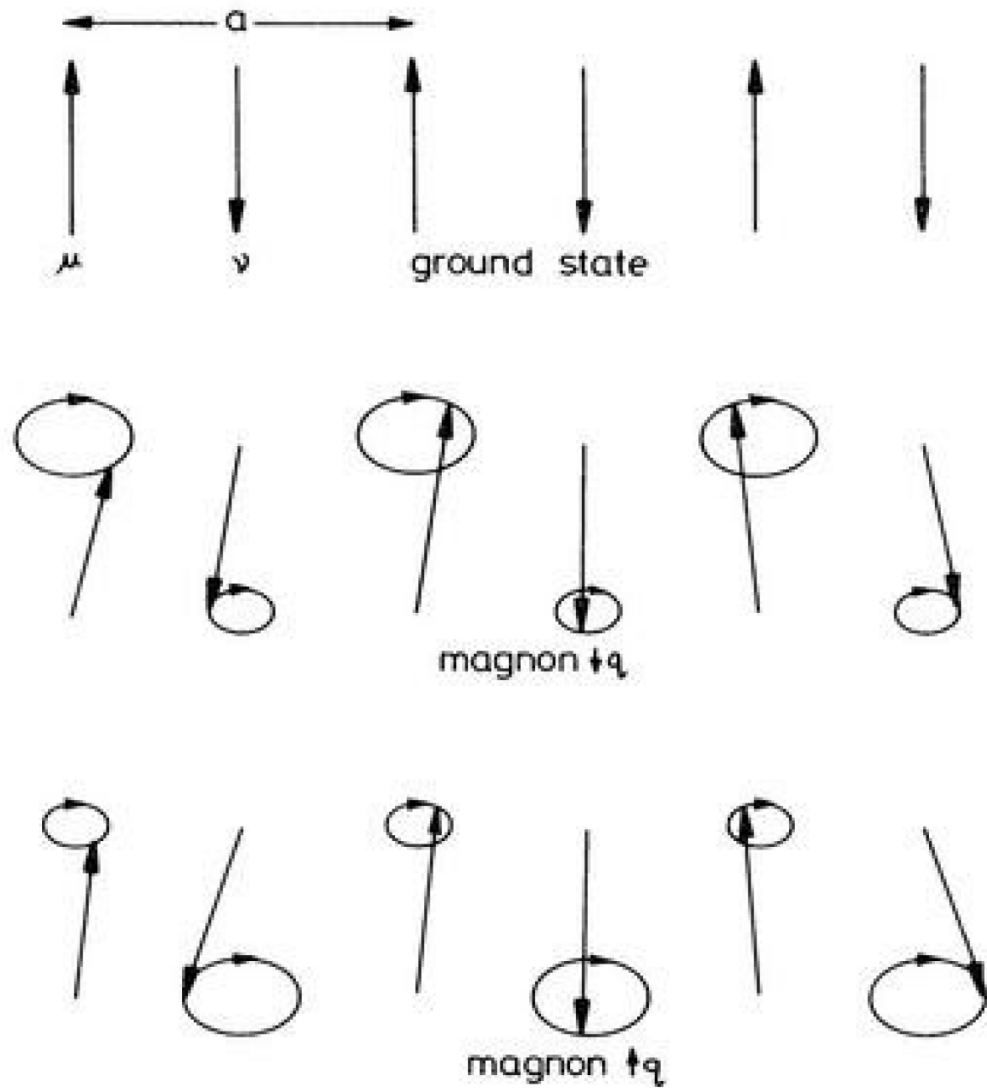


Figure 3.8: Spin waves in an anti-ferromagnet copied from Ref.¹⁴

magnon process is simply the propagation of two identical magnons in opposite directions, assuming one magnetic site per primitive cell. Fig. 3.9 shows the mechanism and how the spin exchange takes place in opposite directions producing two magnon excitations with the same energy but opposite momentum:

CHAPTER 3. EXPERIMENTAL METHODS

$$\omega_I - \omega_S = 2\omega_{\mathbf{q}} \quad (3.13)$$

$$\mathbf{K}_I - \mathbf{K}_S = q_1 + q_2 \approx 0 \quad (3.14)$$

Fig. 3.10 shows the mechanism of spin exchange in detail. The spin exchange takes place between electrons on nearest neighbors ions. In the initial state two electrons are in the ground state $|\mu_+(\mathbf{r}_1)\nu_-(\mathbf{r}_2)\rangle$ where $|\mu\rangle$ and $|\nu\rangle$ are one-electron orbitals on nearest neighbor ions μ and ν and $+$, $-$ subscripts indicate spin components of $+1/2$ and $-1/2$. Spin up electron on μ state is excited by the electric field in the exciting EM wave to higher energy state $|p\rangle$ through electric dipole transition without changing its spin/total angular momentum. Then the spin up electron hops to orbital $|p'\rangle$ on the second ion, due to electron-electron coulomb repulsion, the spin down electron hops to higher energy level in the first ion orbital μ . The spin up electron on state p' then transitions to lower energy orbital and loses energy to produce scattered Raman radiation. As a result of this process, the electrons flip their positions on different ions without changing their spins with final state $|\mu_-(\mathbf{r}_2)\nu_+(\mathbf{r}_1)\rangle$. Such process can be expressed through the transfer matrix element:

$$\langle \nu_+(\mathbf{r}_1) | e^{\hat{\mathbf{E}}_S \cdot \mathbf{r}_1} | p'_+(\mathbf{r}_1) \rangle \left\langle p'_+(\mathbf{r}_1) \mu_-(\mathbf{r}_2) \left| \frac{e^2}{4\pi\epsilon_0} |\mathbf{r}_1 - \mathbf{r}_2| \right| \nu_-(\mathbf{r}_2) p_+(\mathbf{r}_1) \right\rangle \langle p_+(\mathbf{r}_1) | e^{\hat{\mathbf{E}}_I \cdot \mathbf{r}_1} | \mu_+(\mathbf{r}_1) \rangle \quad (3.15)$$

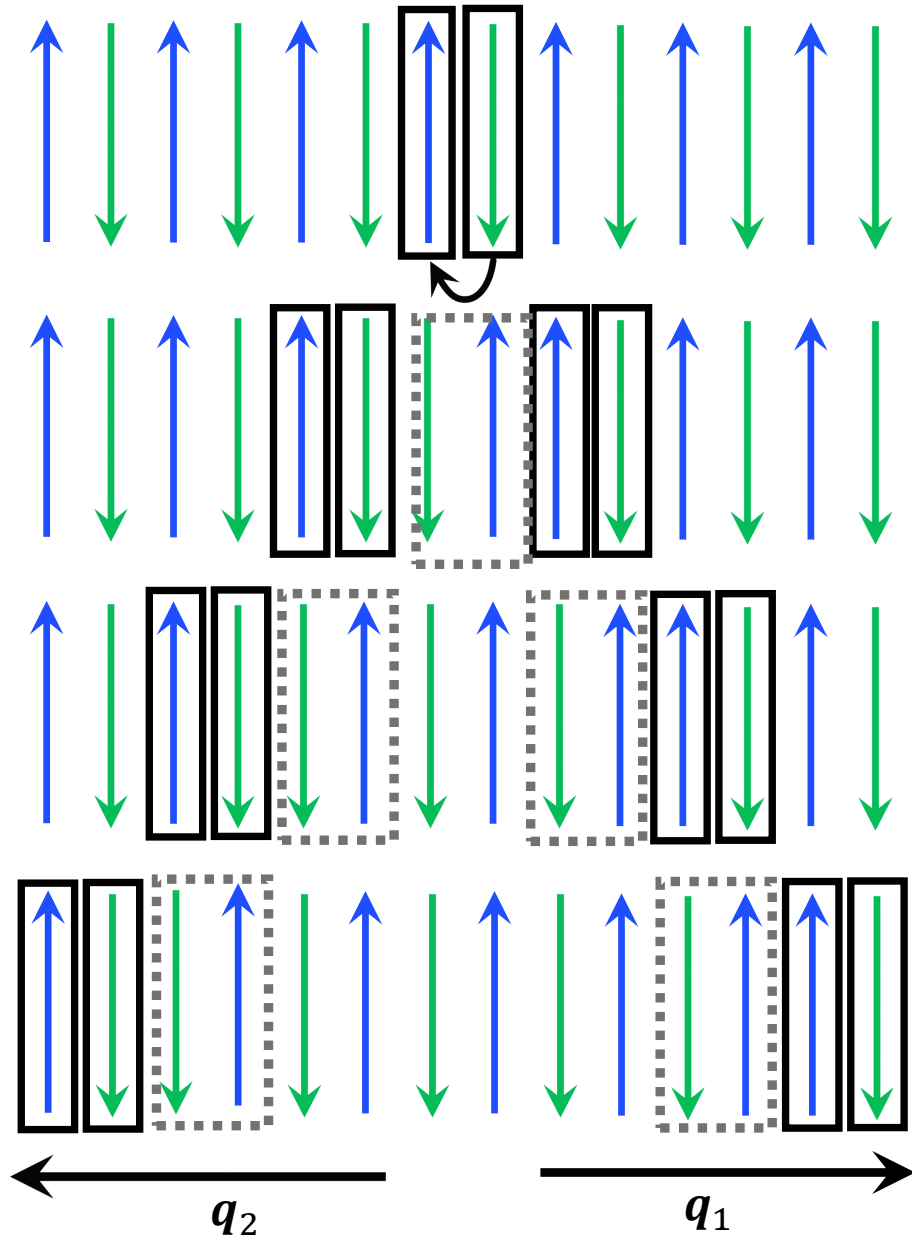


Figure 3.9: Propagation of two-magnon excitation in an anti-ferromagnet, inspired by Ref.¹⁴

where the first and last terms represent the electric-dipole transition of spin up electron from states $|p'\rangle$ to $|\nu_+\rangle$ and from $|\mu_+\rangle$ to $|p_+\rangle$. The middle term represents the exchange

due coulomb repulsion between electrons.

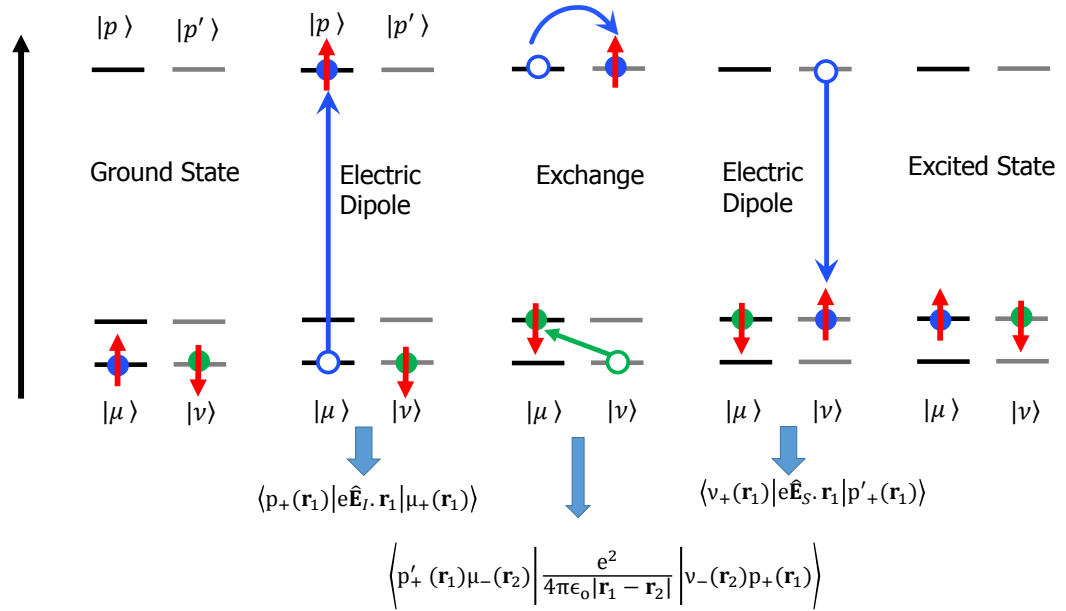


Figure 3.10: Mechanism of two-magnon excitation due to exchange interaction, From Ref.¹⁵

Two-magnon scattering is generally shown in Raman spectrum as a broad peak. The intensity of the band doesn't reflect the two-magnon density of states but rather is a weighted average. This is because of the electric dipole transition term in the transfer matrix, see eq. 3.15. This implies that some two-magnon states will not contribute to the Raman intensity because the corresponding dipole transition is not probed by the polarization of incident and scattered light. The shape and location of two-magnon bands are determined by the magnon interaction. For example, in a 1D chain of spins with anti-ferromagnetic interactions within Ising model, the spin flip of one electron would cost an energy of $2JzS$ where z is the number of nearest neighbor, S is the spin and J is the exchange interaction energy

CHAPTER 3. EXPERIMENTAL METHODS

between spins. Therefore, the cost of spin flip of two non-interacting spins is $4JzS = 4J$. However, in case of two-magnon scattering, the process could be viewed as the flip of two interacting spins and the energy would be $2J(2zS - 1) = 2J$, a reduction in the energy of the two-magnon excitation compared to twice the energy of single magnon. The location of the band corresponds to the excitation energy of two-magnon process.

In 2D magnetic lattices, the interactions get more complicated and generally complex models are tested where more terms are included in the Hamiltonian that includes, next nearest neighbors and ring exchange. Such models are studied to predict the shape, location and polarization dependence of two-magnon band in Raman spectrum. Also, few theoretical calculations^{16,17} were done to study the effect of frustration on the polarization dependence/symmetry and energy of two-magnon bands. In a model of 2D lattice with nearest neighbor interaction J and next nearest interaction J' , theoretical calculations were performed,^{16,17} where the ratio J'/J is increased from 0 (square lattice) to 1 (isotropic triangular lattice). It was shown theoretically and experimentally^{16,37} that in 2D anti-ferromagnetic square lattice, two-magnon band shows strong polarization dependence where the density of states is much more pronounced in cross polarization, B_{1g} mode, than in parallel polarization, A_{1g} mode, see fig. 3.11 b) and 3.12. Such strong polarization dependence decreases as J' increases from 0 to J , see Fig.3.11 a) and 3.12. So in frustrated systems, two-magnon excitations appear in Raman spectrum in the A_{1g} mode too. Also, the two-magnon peak position changes from $3J$ to $3J/2$ by changing $J' = 0$ to $J' = J$. In particular, frustration-driven spectral downshift was observed experimen-

CHAPTER 3. EXPERIMENTAL METHODS

tally.^{16,17} The general trend observed is that spectral softening progressively develops as the system becomes more frustrated. Including other interaction terms in the Hamiltonian such as the ring exchange may predict the broadening of the spectrum due to the increase in low-energy excitations.^{16,17}

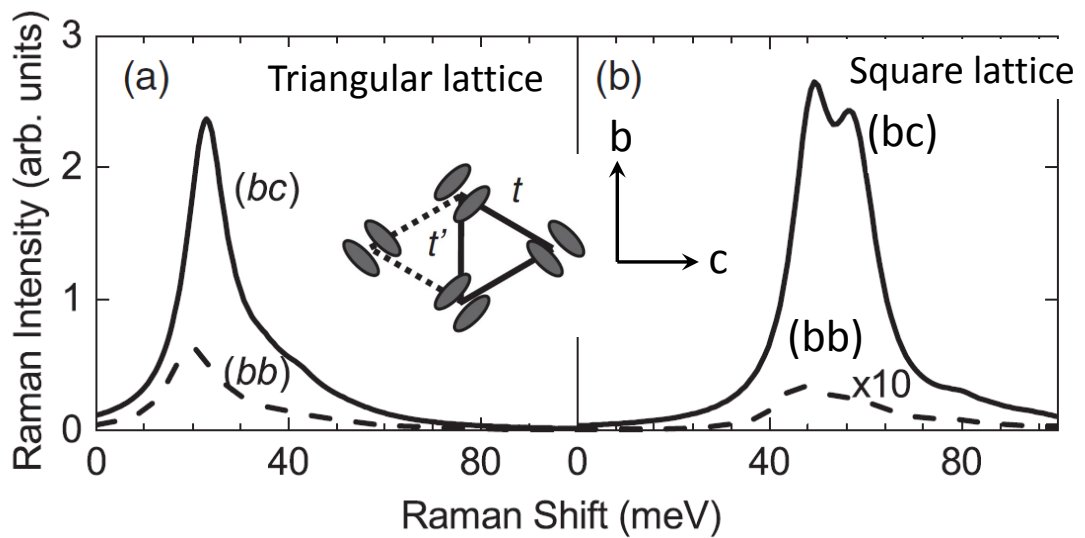


Figure 3.11: a) Calculation of two-magnon band in an isotropic triangular lattice in parallel (bb) and perpendicular (bc) polarization. b) Calculation of two-magnon band in a square lattice of an anti ferromagnetic material. From Ref.¹⁶

CHAPTER 3. EXPERIMENTAL METHODS

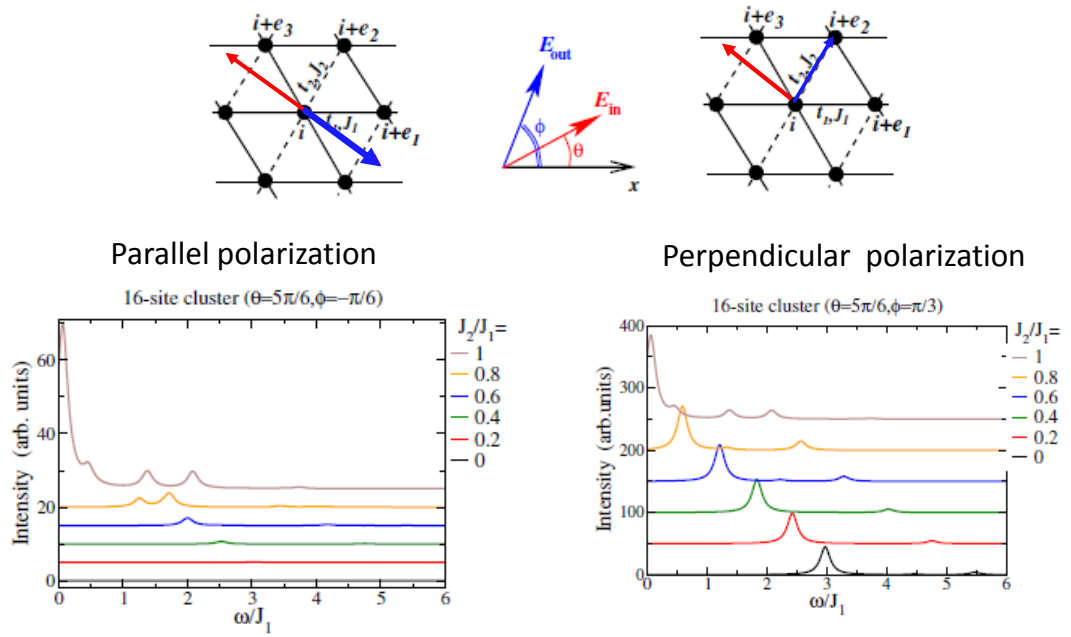


Figure 3.12: a) Calculation of two-magnon band in parallel polarization and the effect of frustration J'/J on the location of the band. b) Calculation of two-magnon band in perpendicular polarization and the effect of frustration J'/J on the location of the band. From Ref¹⁷

3.1.4 Experimental Procedure

Single crystals of κ -(BEDT-TTF)₂Hg(SCN)₂Cl (κ -Hg-Cl) and κ -(BEDT-TTF)₂Hg(SCN)₂Br (κ -Hg-Br) were prepared by electrochemical oxidation of the BEDT-TTF solution in 1,1,2-trichloro-ethane (TCE) at a temperature of 40° C and a constant current of 0.5 μ A. A solution of Hg(SCN)₂, [Me₄N]SCNCl, and dibenzo-18-crown-6 in 1:0.7:1 molar ratio in ethanol/TCE was used as supporting electrolyte for the κ -Hg-Cl preparation. For the κ -Hg-Br preparation, a supporting electrolyte Hg(SCN)₂/[Me₄N]SCN1.5KBr/ dibenzo-18-crown-6 in 1:0.4:1 molar ratio was used. The composition of the crystal was verified by electron probe microanalysis and X-ray diffraction.

Raman scattering was measured in pseudo-Brewster angle geometry using T64000 triple monochromator spectrometer equipped with the liquid N₂ cooled CCD detector. For the measurements in the 5-400 cm⁻¹ range T64000 in triple monochromator configuration was used, for the measurements in the range 80-2000 cm⁻¹ single monochromator configuration with the edge filter option was used. Spectral resolution was 2 cm⁻¹. Lines of Ar⁺-Kr⁺ Coherent laser at 514.nm and 647 nm where used for excitation. Laser power was kept at 2 mW for the laser probe size of approximately 50 by 100 μ m. This ensured that laser heating of the sample was kept below 2 K, as was proved by observing the temperature of ordering transition in κ -Hg-Cl. Measurements at temperatures down to 10 K were performed using Janis ST500 cold finger cryostat. Samples were cooled from 300 K with cooling rates between 0.2 and 0.5 K/min. Samples were glued on the cold finger of the cryostat using GE varnish. The experiments were performed on at least 6 samples to

CHAPTER 3. EXPERIMENTAL METHODS

ensure reproducibility of the results. A few wave numbers spread in the width of ν_2 band at low temperatures for κ -Hg-Br was associated with a weak strain originating from GE varnish, all the other parameters of the spectra were reproducible within the error bar of the measurements. The crystals were oriented using polarization-dependent Raman scattering measurements. For the measurements, electrical vector of excitation e_L and scattered e_S light were polarized along b and c axes. Our notations of polarizations refer to the structure and symmetry of the BEDT-TTF layer, to make an easy comparison to the calculations which refer to D_{4h} ³⁸ without losing the information about the symmetry of the real crystal. Thus A_{1g} symmetry corresponds to the were measurement in (b, b) and (c, c) geometries, and B_{1g} corresponds to (b, c) and (c, b) geometries (xy) . All spectra were corrected by the Bose-Einstein thermal factor. Intensity of the collective mode was calculated as $I(T) = \int_0^{200 \text{ cm}^{-1}} \chi''(\omega) d\omega$

3.2 Heat Capacity

3.2.1 Introduction

Heat capacity (symbol C) is a measurable physical quantity and is defined as the ratio of the heat transferred to or removed from an object to the resulting temperature change.³⁹

$$C_V = (\partial Q / \partial T)_V \quad (3.16)$$

CHAPTER 3. EXPERIMENTAL METHODS

$$C_P = (\partial Q / \partial T)_P \quad (3.17)$$

where the subscripts denotes at constant pressure or constant volume. The unit of heat capacity is joule per kelvin (J/K) and that of specific heat used throughout the document is $mJ/K.mole$

Heat capacity measurements of organic conductors were taken to study phase transitions and understand the different contributions to density of states and excitations of the material. The behavior of the heat capacity as a function of temperature has generally three contributions; lattice contributions due to phonons, electronic contribution and magnetic contributions. A typical plot of heat capacity is shown in figure 3.13 that shows the different contributions to the total heat capacity.

Debye model and Eisenstein models were developed to estimate the phonons contribution to the specific heat in solids. Debye's model treats the vibrations of the atoms in the lattice as phonons in a box while Einstein's model treats the atoms in a crystal as many 3D non-interacting quantum harmonic oscillators with the same frequency. The Debye model correctly predicts the T^3 dependence of the heat capacity at low temperature. Both models recover the Dulong-Petit law at high temperatures. In metals, the main low-temperature contribution to the heat capacity comes from the electrons and is calculated by different methods such as Sommerfeld's free electron model. The electron contribution to the heat capacity is proportional to T , which dominates the Debye contribution ($\sim T^3$) at low temperatures.

What we measure experimentally is heat capacity at constant volume C_P . We used

CHAPTER 3. EXPERIMENTAL METHODS

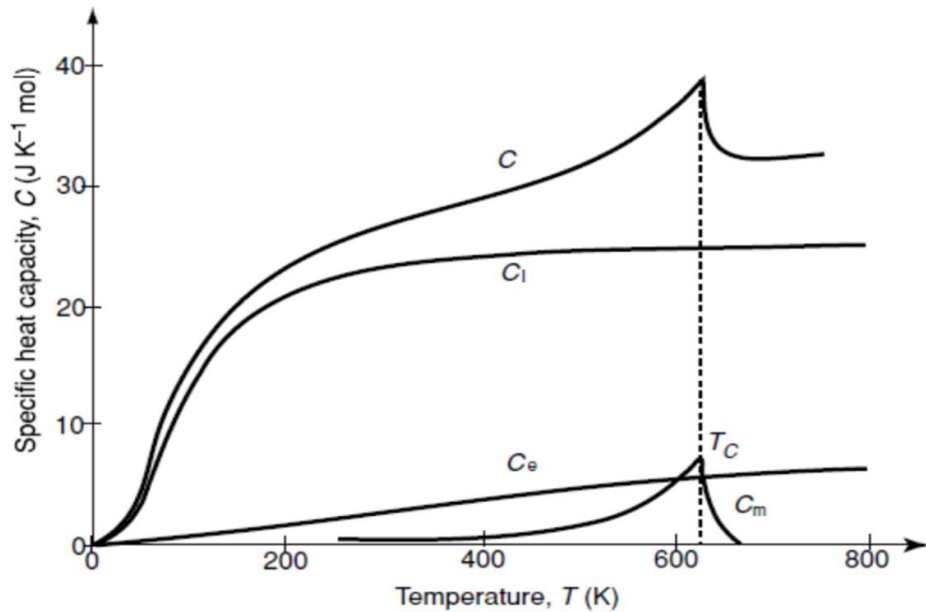


Figure 3.13: From Reference.¹⁸ Plot of heat capacity of Nickel. It shows different contributions to total heat capacity.

Quantum device PPMS where the relaxation method is the basis of operation to measure the heat capacity. The set up of the puck is shown in figure 3.14. The PPMS relaxation calorimeter consists of a 3 mm x3 mm alumina platform attached to a heat sink puck using eight thin wires. A thin film RuO heater and a temperature sensor (Cernox sensorTM from Lakeshore Cryotronics) are attached to the back of the platform. The platform has a well controlled thermal link to a constant temperature heat sink, at temperature T_o through the eight thin wires. A radiation shield fits over the top of the puck.¹⁹

The basic operation is as follows: A heater current is applied and the thermometer resistance is recorded at 4ms intervals. The heater voltage is recorded to compute the heater power. A measurement cycle to measure one data point of heat capacity consists of a heating period followed by a cooling period. The platform is heated to temperature

CHAPTER 3. EXPERIMENTAL METHODS

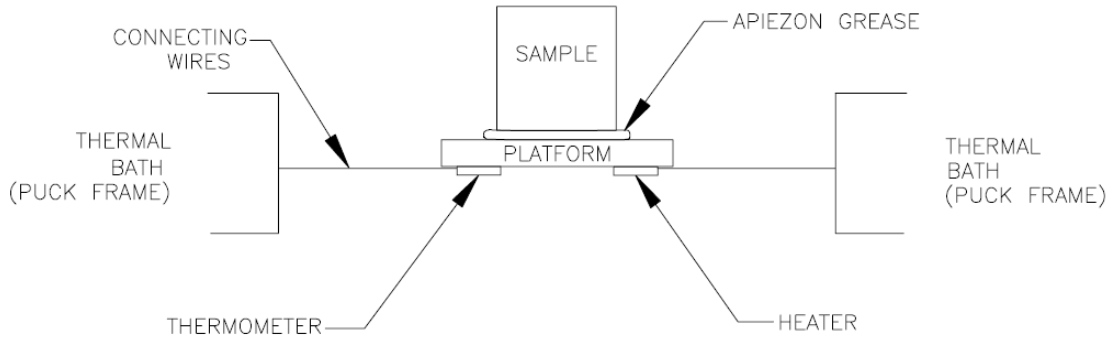


Figure 3.14: From Reference.¹⁹ Plot of the setup of the puck/sample holder of the commercial PPMS. The heater increases temperature of the sample and thermometer measures the temperature. The connecting wires act as the only thermal contact with the puck frame (thermal bath).

$T = T_0 + \delta T$ and then allowed to relax back to T_0 . The value δT of heating can be varied and is one of the parameters of the measurements. Typically, "short pulses" technique is used (all figures below is of measurements done at short pulses), with $\delta T = 0.5 - 3\%$ of T_0 . For identification of 1st order phase transitions "long pulse" technique is used, with $\delta T > 50\%$ of T_0 . The obtained data on the temperature of sample as a function of time is fitted by two models to extract information about heat capacity. The fit is made by the software during the measurement.

Two models were used to fit the raw data and calculate the heat capacity. The simple model is used if there is a very good contact between the sample and platform and thus, have the same temperature at any point in time. In the simple model, the temperature T of the platform as a function of time t is:

$$C_{total}dT/dt = -K_w(T - T_b) + P(t) \quad (3.18)$$

CHAPTER 3. EXPERIMENTAL METHODS

When the power input is discontinued, the temperature decay of the platform $T(t)$ can be described by:

$$T(t) = T_0 + \delta T e^{-t/\tau} \quad (3.19)$$

where C_{total} is the total heat capacity of the sample and sample platform; K_w is the thermal conductance of the supporting wires; T_b is the temperature of the thermal bath (puck frame); and $P(t)$ is the power supplied by the heater (P_o during heating and zero during cooling). The solution of this equation is given by exponential functions with a characteristic time constant τ equal to C_{total}/K . δT should be small so that the thermal conductivity between platform and heat sink (K_1) and C_{total} can be considered T independent.

If thermal contact between sample and platform K_2 is poor such that the condition $K_2 \gg K_1$ is not satisfied, then the two-tau model is used. Temperature decay can be expressed as two exponential terms:

$$C_{platform} = (dT_p)/dt = P(t) - K_w(T_p(t) - T_b) + K_g(T_s(t) - T_p(t)) \quad (3.20)$$

$$C_{sample} = (dT_s)/dt = -K_g(T_s(t) - T_p(t)) \quad (3.21)$$

$$T(t) = T_0 + A e^{-t/\tau_1} + B e^{-t/\tau_2} \quad (3.22)$$

where $\tau_1 = C_{pl}/K_1$, $\tau_2 = C_{sample}/K_2$; C_{pl} is the heat capacity of the platform and

CHAPTER 3. EXPERIMENTAL METHODS

addenda, K_1 is the thermal conductivity between the platform and heat sink, K_2 is the thermal conductivity between the sample and the platform, and C_{pl} is the heat capacity of the sample. However, this model is valid only when the sample coupling, defined as $100 \times (K_2/(K_1 + K_2))$ is close to 100. The program uses least-square fitting algorithm to determine which model fits the data better.

In all models, what is measured is the total heat capacity of the sample plus platform. However, we are interested in the heat capacity of the sample only. Thus, before measuring heat capacity of the sample, we measure heat capacity of the platform plus grease (Apizone N), called addenda heat capacity, and then add the sample and do a second measurement with the sample mounted on the platform. The PPMS program automatically subtracts the addenda heat capacity from the total heat capacity to find that of the sample. The amount of grease should be enough to achieve good thermal contact between the sample and the platform without constituting too much of the signal. Also, we preferred to have a flat morphology of the grease to lower the effect of change in heat capacity. This could have large effect especially that our samples are very small. All heat capacity measurements were measured in $mJ/mole.K$.

3.3 Technical Issues

There are many technical issues that can render the data inaccurate measurements of heat capacity. These were the problems faced during our measurements of heat capacity.

CHAPTER 3. EXPERIMENTAL METHODS

- Reproducibility
- Sample coupling
- Effect of mass sample mass on measurement error
- Selection of measurement parameters
- Artifacts due to applied magnetic field

3.3.1 Reproducibility

Our first aim was to reproduce published heat capacity results of κ -(ET)₂ Cu₂ (CN)₃ and calculate lattice and spinon excitation contribution to confirm that we could get high quality heat capacity results using the relaxation method on a commercial setup and with small sample size (mass is 0.38 mg). For each of the newly studied materials we repeated measurements on a number of crystals to estimate the error in measurements due to electronics, fits and to investigate and exclude sample dependence. Figure 3.15 shows two measurements of the same crystal (κ -(ET)₂ Cu₂ (CN)₃) done on the same setup immediately one after the other. Measurements were done after sample was cooled at 0.5K/min at zero magnetic field. Both measurements show exactly the same result with the kink at 6 K found in literature.²⁰ Also, the measurement could be used to have an estimate of errors due instrumentation instability at zero field and random errors of heat capacity. The inset shows that there could be a negligible shift of the kink that could be due to either data sampling or due to the fact that on cooling the temperature needs more time to stabilize or reach the set

CHAPTER 3. EXPERIMENTAL METHODS

point. Figure 3.15 b) is a measure of the κ -(ET)₂ Hg(SCN)₂ Cl. The blue and red curves were taken on warming the same sample at the same conditions. The measurements were taken consecutively. They show no difference and good reproducibility. The inset on the right is a close up on one data point and rough estimate of the random error is around 10 mJ/mole.K with ideal sample coupling and parameters.

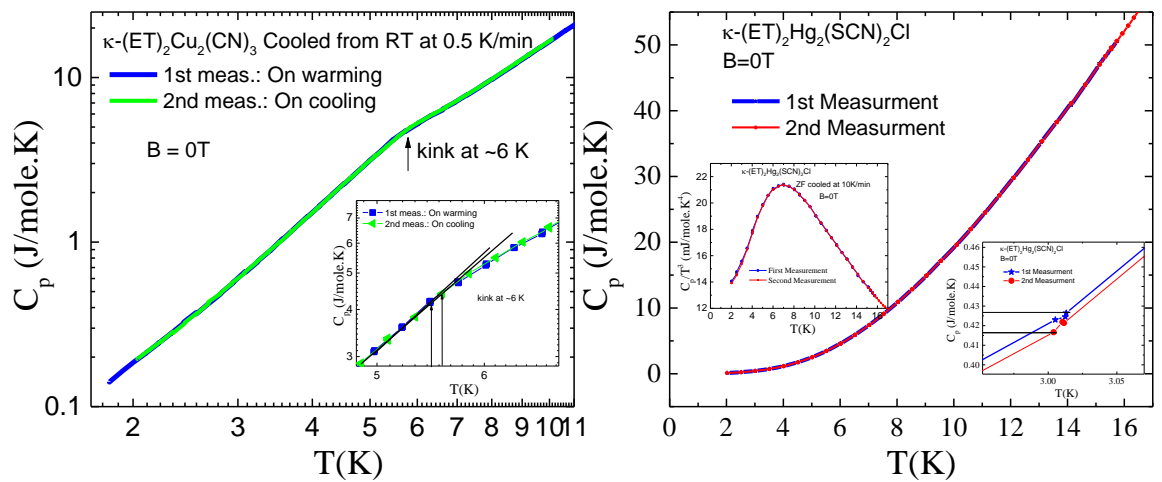


Figure 3.15: a) Plot of C_p vs T of κ -(ET)₂ Cu₂ (CN)₃. The measurements was taken of the same sample at the McQueen lab at zero field and cooled at 0.5 K/min. Two curves (blue and green) show a kink at 6 K that is detected in Ref.²⁰ The blue curve is taken on warming, the green curve is data taken on cooling. The inset is a closeup at the kink. b) Plot of κ -(ET)₂ Hg(SCN)₂ Cl. The blue and red curves are two measurements done at the same instrument with same sample under zero field. The inset on the right is a closeup on data points to have an estimate of random errors (around 10 mJ/mole.K). The inset on the left is a plot of C_p/T^3 vs T of the same measurements. It shows that even at very specific features, the data is very reproducible.

We also checked reproducibility by comparing measurements done with the same sample but different addendas under the same conditions (same field and cooling rate). This introduced a larger error that could be attributed to features that are sample dependent, or sample coupling or measurement parameters, or setup dependent if different instruments

CHAPTER 3. EXPERIMENTAL METHODS

were used. Fig. 3.16 a) Is a plot, C_p/T vs T , of two measurements done at IQM PPMS with the same of κ -(ET)₂ Hg(SCN)₂ Cl with mass 1.11 mg. The measurements were taken with different addenda (i.e sample remounted). The result are reproducible with larger errors at phase transitions. The large error at phase transitions could be due to instability of the system or less favorable parameters or bad sample coupling; all are discussed below.

Fig. 3.16 b) is a comparison between two measurement of two samples of κ -(ET)₂ Hg(SCN)₂ Br; two samples of masses 0.8 mg (blue curve) and 0.6 mg (black curve) were measured on the same setup (IQM PPMS). Both samples were zero field cooled at 0.5K/min. The figure is a plot of C_p/T vs T at 0 Tesla; no factor was multiplied to either measurements to superimpose on each other. There is a pronounced difference between both measurements in the temperature range 15K to 35K. Looking closely at the parameters of the measurements, it looks like the first measurement (blue curve) has worse values for the "sample coupling" than that of the second measurement which could be cause for such difference. Also, The first measurement has a pronounced instability of values manifested in the zigzag shape of data points where the first measurements gives a vastly different values from subsequent repetitions of one data point, see inset.

Figure 3.16 c) is a plot two measurements of different samples of κ -(ET)₂ Hg(SCN)₂ Cl; The first measurement, blue curve, was taken for a sample of mass 0.56 mg and was cooled in zero field at 0.5 K/min at the McQueen PPMS. The second measurement, green curve, was taken of a sample of mass 1.11 mg at the IQM PPMS and was cooled at 1K/min from RT to 85 K and from 65K to 2K, and at 0.5K from 85K to 65K. The plot is of C_p/T vs T .

CHAPTER 3. EXPERIMENTAL METHODS

There is good reproducibility until around 25K where the quality of the first measurement (blue) starts to deteriorate. The inset is a plot of C_p/T^3 vs T because this features shows changes and differences that needs to be studied. The red curve is just the green curve multiplied by a factor of 1.05 to superimpose it on the data taken at McQueen PPMS. A comparison between the blue curve (McQueen PPMS data) and the red curve (IQM PPMS data) shows that there is a slight difference at temperatures less than 8K. However, such difference can't be attributed to true behavior because a comparison between cooling rates in chapter 6 shows no difference in that region. In conclusion, comparing different measurements (after accounting for mass error by multiplying by a factor) of the same sample whether taken at same or different setups, or with same or different parameters will in general give good reproducibility of general features but wouldn't be useful for detecting very small features.

3.3.2 Sample Coupling

Sample coupling was one of the most important parameters to watch while taking the measurement and the most challenging source of problems. The poor coupling will affect the the fitting of data points and subsequently the heat capacity value. Poor thermal coupling could be due to poor mounting of sample or a problem with the sample reaching thermal equilibrium in short time compared to measurement time. Fitting difficulties can also arise when the heat capacity of the sample is not large compared to the platform and this could explain the problems taking place at higher temperature where the sample heat

CHAPTER 3. EXPERIMENTAL METHODS

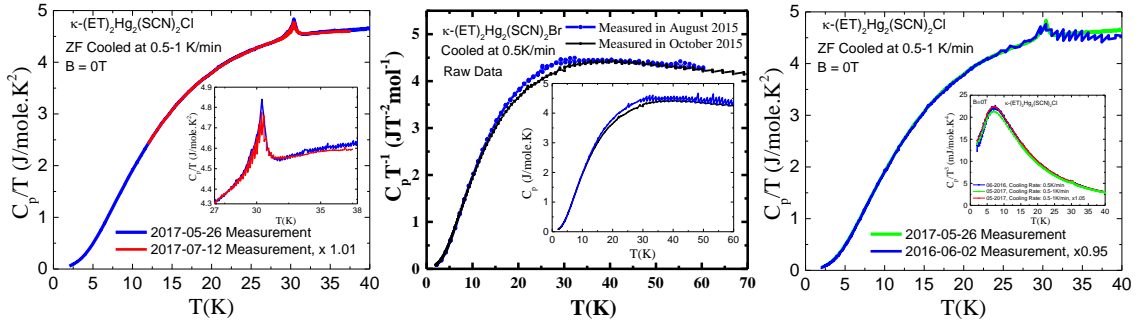


Figure 3.16: a) Plot, C_p/T vs T , of two measurements done at IQM PPMS with the same of κ -(ET)₂Hg(SCN)₂ Cl sample with mass 1.11 mg. The second measurement (red) was re-scaled. The inset is a close up of the phase transition at 30K. b) A plot of C_p/T vs T of two different κ -(ET)₂Hg(SCN)₂ Br samples. The inset is the raw data of the two measurements before removing the noisy data. c) Plot, C_p/T vs T , of two measurements of two different samples of κ -(ET)₂Hg(SCN)₂ Cl. One of the measurements was taken at McQueen PPMS (date June 2016) and the other at the IQM PPMS (May 2017), at zero field. First sample was cooled at 0.5 K/min, the data was re-scaled (x 0.95). Second sample was cooled at 0.5K/min in the temperature range 85K to 65K and at 1K/min at other temperatures. The inset is a plot of C_p/T^3 vs T of the feature at around 8K. The comparison shows slight changes at temperatures lower than 8K.

capacity percentage is less than 10%. Generally, 100% is considered perfect coupling and anything less than 90% is considered poor sample coupling. It was difficult to achieve good sample coupling because we are restricted with the amount of Apieson N grease. We didn't want the addenda to contribute to the bulk of the signal (even though that was always the case due to the very small size). Also, the samples are fragile and so we couldn't press it hard on grease. In addition to that, we didn't want to change the morphology of the grease to a flatter shape that could greatly affect the addenda and as a result introduce features that could be mistaken for true behavior. Generally, it was noticed that multiple flat pieces of a sample is much better than bulky ones because they have better coupling and faster to reach thermal equilibrium.

CHAPTER 3. EXPERIMENTAL METHODS

During the measurement, the software calculates sample coupling as one of the parameters. If the coupling values are bouncing around in synchronization with whether it fits it with 1 tau or 2 taus models, then the sample has borderline poor sample coupling. Sample coupling can be tested at room temperature or temperatures higher than the range of interest before the measurement starts. We tested and compared coupling at 260 K and 10 K. Even though the coupling was 100 at the temperatures tested, it was not enough to verify good coupling. A good strategy would be measuring few temperatures to have a better idea on the noise to signal ratio. Fig. 3.17 a) is a plot of C_p/T vs temperature; it shows a comparison between good and poor quality of data. The blue curve shows the measurement of a sample of κ -(ET)₂ Hg(SCN)₂ Cl with mass 0.56 mg. The green curve shows the heat capacity of a sample of κ -(ET)₂ Hg(SCN)₂ Cl with mass 1.11 mg. The quality of the blue curve is much worse (larger noise) at temperatures above 20K. One of the reasons that could account to such bad quality is poor coupling (in addition to smaller mass and less data points). Fig. 3.17 b) and c) are plots of the sample coupling, time constants tau 1 and tau 2 of the first measurement shown in green curve and second measurement in blue curve. Even though the sample coupling of the first measurement (green curve in fig a) goes to lower values at high temperatures (to around 80%) than that of the second measurement (blue curve in figure a) that doesn't go lower than 90%, the quality of the measurement is much better.

CHAPTER 3. EXPERIMENTAL METHODS

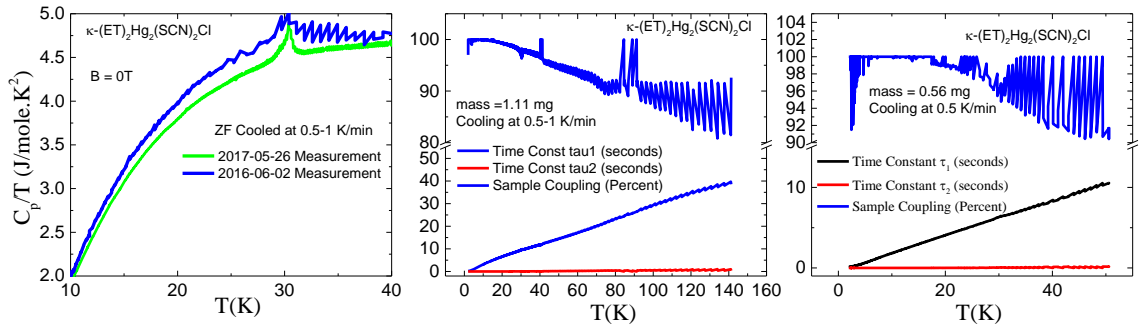


Figure 3.17: Plot of C_p/T vs T of two different measurements of κ -(ET)₂Hg(SCN)₂Cl. One of the measurements was taken at McQueen PPMS (date June 2016), blue curve, and the other at the IQM PPMS (May 2017), green curve, at zero field. First sample was cooled at 0.5 K/min. Second sample was cooled at 0.5K/min in the temperature range 85K to 65K and at 1K/min at other temperatures. b) A plot of fit parameters, τ_1 and τ_2 , and the sample coupling of the data taken at IQM PPMS, green curve in plot a). c) A plot of fit parameters, τ_1 and τ_2 , and the sample coupling of the data taken at McQueen PPMS, blue curve in plot a)

3.3.3 Effect of sample mass on measurements error

We mostly worked with very small samples because organic conductors crystals generally have masses less than 1 mg. There are two effects associated with small sample mass:

- Heat capacity of the sample is a small percentage of the total heat capacity measured.
- Error bar on the measurement of the mass itself is relatively large.

Because the heat capacity measured by the instrument is the total heat capacity of the sample plus the sample holder (called addenda), small sample mass means that the relative heat capacity value with respect to the total heat capacity is very small. Fig. 3.18 shows the sample heat capacity percentage (sample heat capacity/Total heat capacity) of different

CHAPTER 3. EXPERIMENTAL METHODS

measurements. As shown the value is not constant; the general behavior with organic samples was that the percentage was highest in the temperature range $T=10\text{K}$ to $T=30\text{K}$. Generally, the sample heat capacity rarely reaches 70% with much smaller contribution at higher temperature. At higher temperatures the sample heat capacity is less than 10 percent of the total heat capacity with the remaining 90 percent due to addenda. Random errors in addenda will have significant effect on the quality of the sample heat capacity if the fractional heat capacity is small relative to the total heat capacity. That means that random errors are going to dominate and thus, we cannot see any weak features. This could explain the higher noise at higher temperatures. The system will be more tolerant of poor coupling when the sample is a larger fraction of the total heat capacity.

The heat capacity error calculated by the program is a combination of the random error due to fitting accuracy and error due to inaccuracy in mass measurement. The latter overwhelms the total error and could be exaggerating the error. Fig 3.18 b) is a plot of C_p vs T of raw data of two different measurements of $\kappa\text{-(ET)}_2\text{Cu}_2(\text{CN})_3$ cooled at 0.5K/min (red curve) and 0.1 K/min (blue curve). The green curve is a representation of the same measurement shown by red curve but multiplied by a factor 1.17. That proves that that the large difference between the red and blue curve is due to error in mass measurements that could be compensated for by multiplying the data by a constant factor. Generally the measurement with the smallest mass (0.2 mg) required to be multiplied by the largest factor (x 1.17) showing that an error in mass could be as large as 20%. The inset shows the same figure but with error bars; the two curves agree within error bars. As mentioned earlier

CHAPTER 3. EXPERIMENTAL METHODS

the error bars are partly due to error in mass measurements which could reach 20%; therefore, by multiplying a measurements by a constant factor we managed to compare different measurements.

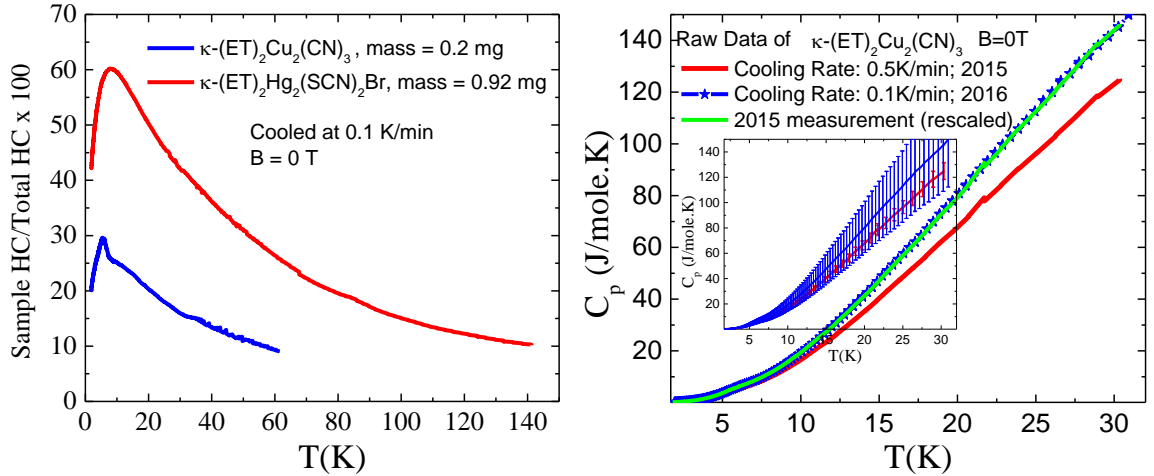


Figure 3.18: a) Plot of percentage of sample heat capacity relative to total heat capacity: Sample heat capacity/Total heat capacity x100 of κ -(ET)₂ Cu₂ (CN)₃ and κ -(ET)₂ Hg(SCN)₂ Br. The sample masses were 0.3 mg and 0.92 mg. The samples were cooled at 0.1 K/min at zero field. b) Comparison between two measurements of κ -(ET)₂ Cu₂ (CN)₃; red curve is a measurement of a sample of mass 0.38 mg measured in 2015 in McQueen PPMS and cooled at 0.5 K/min. The blue curve is a measurement of a sample of mass 0.2 mg measured in 2016 in IQM PPMS and cooled at 0.1 K/min. The green curve is the 2015 measurement but re-scaled by a factor of 1.17. The inset shows the same measurements but with error bars to show the significant contribution of mass error to error bars. The original data (not re-scaled) agree within the error bars.

3.3.4 Selection of measurement parameters

There are few parameters that could be changed to improve quality of the data, some are:

- Number of data points; that determines the resolution. if fine features or phase transi-

CHAPTER 3. EXPERIMENTAL METHODS

tions are expected to be seen at a certain temperature, it is imperative to take many data points.

- The temperature rise; this could be set in terms of temperature percentage (for example 5% of the current temperature) or in terms of absolute temperature (for example 5 K). Generally, it is better to follow recommended values. It could be that higher values are better for features like phase transitions, see Fig. 3.20.
- Time of measurements; i.e the time it takes for the heating and cooling cycles in terms of time constant. Also, it is better to follow recommended values. No need for any values longer than 3 tau.

It seems that at phase transitions the measurement parameters are important for the quality of data. Figure 3.20 shows two sets of measurements of the phase transition of the same sample of κ -(ET)₂ Hg(SCN)₂ Cl (mass 0.93 mg) at 30 K. The measurements were done on the same setup (IQM PPMS) and same addenda (no remounting). The 2nd cooling cycle was measured by heating the sample to 2% of the temperature while the first set was measured by heating to 1% of the temperature. Also, more data points were taken which I think had more effect to get high resolution data. If the temperature rise values were chosen very high (more than 5% or 2K), the data fit by the program would be inaccurate and values given for capacity heat would be inaccurate. We used very high temperature rise (over 5K) to do long pulse measurement. The commercial software is not appropriate to fit such data to produce heat capacity data. So there are two uses for such data:

CHAPTER 3. EXPERIMENTAL METHODS

- First, to check for first order phase transition; we use the raw data which is a plot of temperatures against time to look at the pattern of the heating cycle and cooling cycle in the temperature range of interest. If first order transition takes place in the temperature range, signatures of latent heat should be seen in the heating and cooling cycles. Fig. 3.22 shows the difference between two hypothetical long pulse measurements, the figure on the left is what is expected if no first order phase transition is taking place. The figure on the right shows that first order phase transition takes place at the time when the heater is on but the temperature is not rising with time. Same is happening in the cooling cycle. This is because heat is absorbed as latent heat in first order phase transition rather than in raising the temperature of the sample.
- Second, to take measurements similar to short pulse measurements but with faster and better results, the raw data have to be processed by a new program introduced in ref.¹⁹

3.3.5 Artifacts due to applied magnetic field

Figure 3.23 shows the addenda under different fields. The plot is of C_p/T^3 vs T because that is the feature that showed the most change with field while measuring samples. We wanted to check if it is a real feature or an artifact. It is expected to have a magnetic field effect on the addenda but the effect should not be as large. Also, it was interesting that the maximum effect is in the same temperature range (3K to 10 K) that we observe a change

CHAPTER 3. EXPERIMENTAL METHODS

in the heat capacity of the sample. This makes us suspect that the effect could be due to the addenda even though the addenda effect should have been subtracted in theory. However, the change in the morphology of the addenda changes its value, and even though extreme care was taken to not change grease morphology when we mounted the sample, there could be slight change that isn't entirely subtracted. The effect could be further magnified by the fact that heat capacity of samples were consistently much smaller than that of addenda .

In conclusion, measuring heat capacity of organic conductors is tricky because they generally have very small masses. As a result of the presented tests and other recommendation from literature,^{19,40} I summarize the following recommendations for heat capacity measurements of organic insulator samples using Quantum Design PPMS:

- Sample should be measured at room temperature to make sure it is well mounted and produces good results at high temperature before cooling down.
- Addenda measurements should be done at zero field before turning on the field.
- Most problems are due to either the sample is too small or is poorly coupled to the platform. Because our samples are generally very small on the limit of what could be measured in this setup, many measurements suffered from low quality data.
- Too much grease may produce a poor measurement of the addenda resulting in an inaccurate sample heat capacity measurement. The grease used depends on the samples size and geometry; the grease should be spread out in a thin layer over the area that would be in contact with the sample. Also, samples should be mounted with care

CHAPTER 3. EXPERIMENTAL METHODS

to insure that the amount of grease doesn't change.

CHAPTER 3. EXPERIMENTAL METHODS

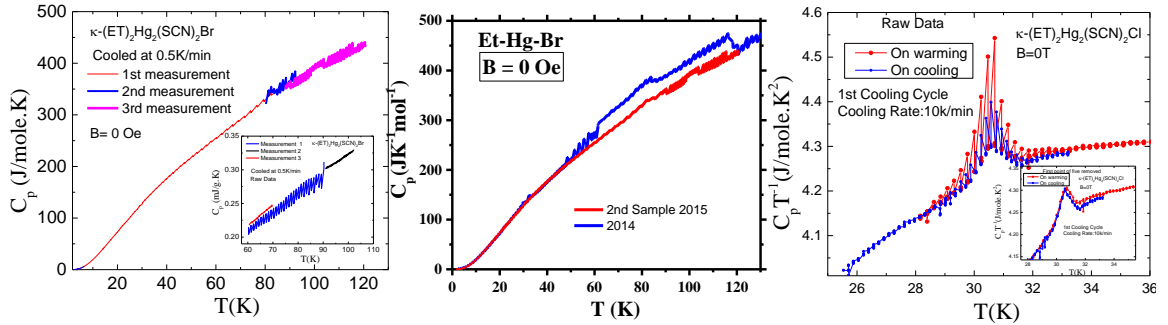


Figure 3.19: a) Plot of C_p vs T of κ -(ET)₂ Hg(SCN)₂ Br cooled at 0.5K/min in zero field. All measurements were done on the same sample, same addenda and setup at IQM PPMS. The measurements were done consequentially of different temperature ranges. The data shows instability due to unknown reasons (I think mainly change in temp rise parameter). The inset is another measurement of κ -(ET)₂ Hg(SCN)₂ cooled at 0.5K/min in zero field. All measurements were done on the same sample, same addenda and setup at IQM. The three measurement were done consequentially at different temperature ranges. The major difference in the quality of the measurement could be due parameters used. b) The plot of C_p vs T of κ -(ET)₂ Hg(SCN)₂ Br is a comparison between two different measurements done on different samples. It is obvious the lack of instability and irreproducibility of some of the features (jumps) that could be attributed to either poor sample coupling or poor choice of parameters. (However, the jump in the blue curve at around 65 K was detected in another measurement of the same material at 0.1K/min and 0.5 K/min but at a much smaller scale, the jump at 120 K was not seen in any other measurement). c) Plot of C_p/T vs T of the phase transition of κ -(ET)₂ Hg(SCN)₂ Cl at 30 K. The plot of raw data to show huge difference between the heat capacity value of the first point and subsequent measurement of the same data point. The inset shows the same plot after the first point was removed.

CHAPTER 3. EXPERIMENTAL METHODS

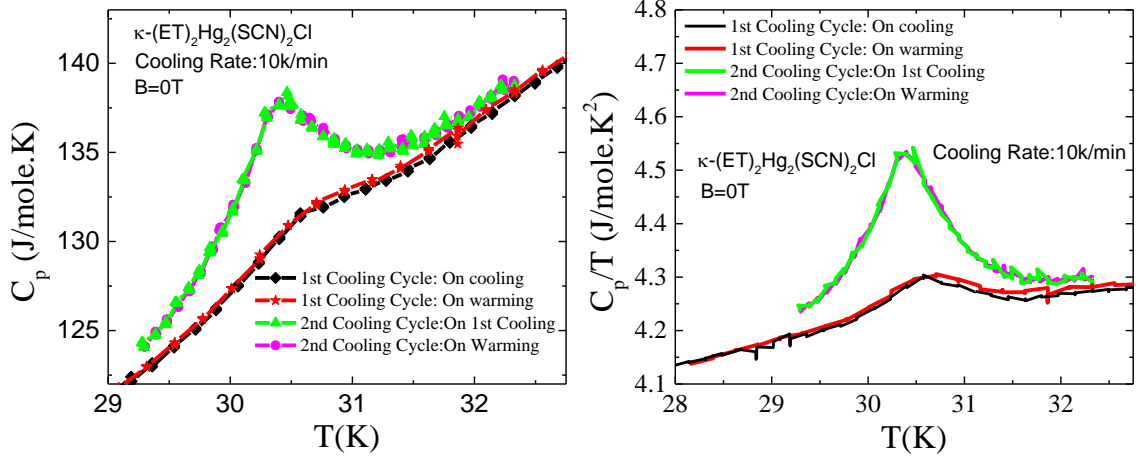


Figure 3.20: a) Plot of C_p vs T of the phase transition of κ -(ET)₂ Hg(SCN)₂ Cl at 30 K. It compares two different cooling cycles; both measured the same sample with same addenda (was not remounted) on same setup (IQM PPMS) cooled at 10 K/min in zero field. The only difference is the measurements parameters. b) Plot of C_p/T vs T of the phase transition of κ -(ET)₂ Hg(SCN)₂ Cl at 30 K.

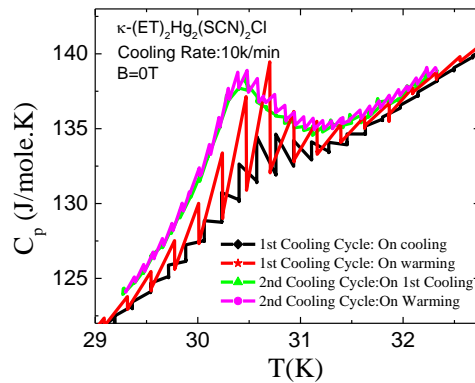


Figure 3.21: Plot of C_p vs T of κ -(ET)₂ Hg(SCN)₂ Cl. Same as figure above but without subtracting the first point

CHAPTER 3. EXPERIMENTAL METHODS

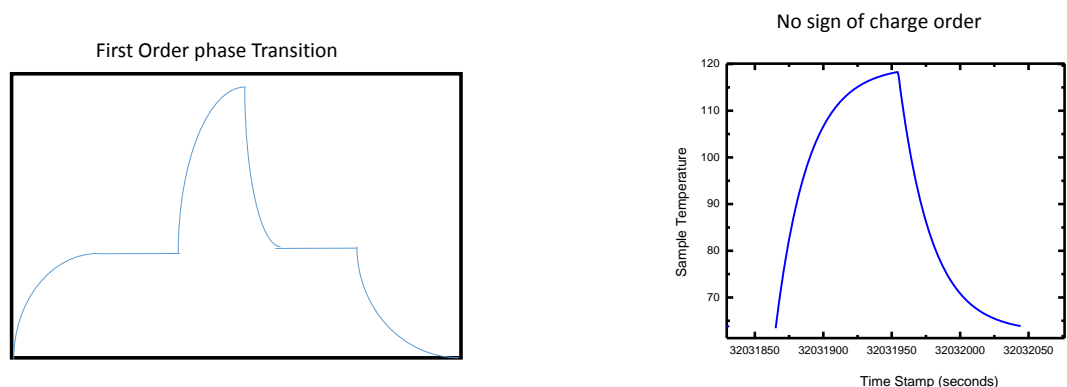


Figure 3.22: a) A plot of temperature vs time stamp of the raw data that is later fitted to produce heat capacity values. This figure shows the hypothetical shape of the plot in case of first order phase transition. b) Plot of temperature vs time stamp of κ -(ET)₂ Hg(SCN)₂ Br in the temperature range 70 K-to 120 K to test for first order phase transition.

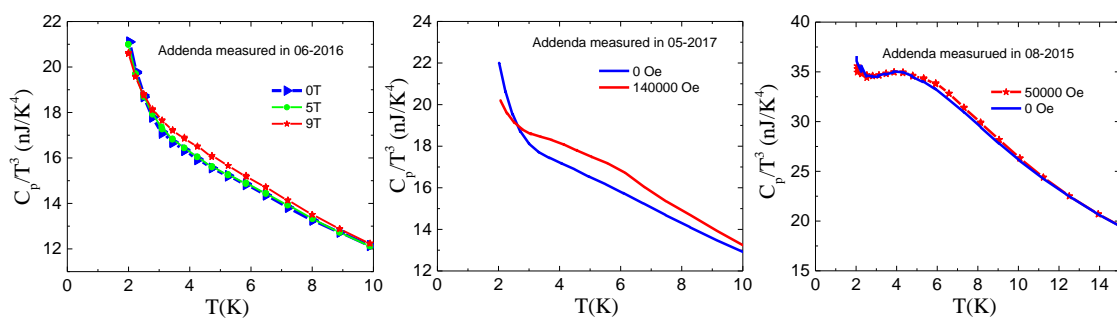


Figure 3.23: Plot of C_p/T^3 vs T of addenda with and without field. The effect of the field is pronounced.

Chapter 4

Study of the ground state of κ -Hg-Br

4.1 Introduction

Recently a number of groups have shown theoretically how fluctuating dipolar degree of freedom can appear in molecular-based Mott insulators, and lead to a spin liquid state in presence of charge-spin coupling. Among suggested model systems are quasi-two-dimensional BEDT-TTF molecule-based Mott insulators^{6,41} and optical lattices of dipolar molecules.⁴² In quantum paraelectrics fluctuations of electric dipoles are observed in the vicinity of a ferroelectric transition.⁴³ A quantum dipole liquid in an antiferroelectric on a triangular lattice was recently reported for $\text{BaFe}_{12}\text{O}_{19}$,⁴⁴ but it is a band insulator and thus non-magnetic. A quantum dipole liquid in a Mott insulator is a new paradigm for quantum states of matter which brings together quantum paraelectrics and spin liquids.

In this work we discuss a new experimental realization of the quantum dipole liquid

CHAPTER 4. STUDY OF THE GROUND STATE OF κ -HG-BR

state in a layered organic crystal κ -(BEDT-TTF)₂Hg(SCN)₂Br based on molecule BEDT-TTF¹. It is a Mott insulator, and in a presence of charge-spin coupling may be a new spin liquid candidate. Electronic and magnetic phenomena observed in this class of materials are defined by the properties of the molecular-based cation layers (Fig 4.1 a). In a Mott insulator of this origin, electrons are localized on lattice sites of dimers (BEDT-TTF)₂⁺¹ with S=1/2 per site. These dimer sites form layers which can be represented by two-dimensional anisotropic triangular lattice (see Fig. 4.1 c). In most of such compounds the dimers have an inversion center and thus zero electric dipole moment. Frustration of the lattice, competing electronic correlations and magnetic interactions can lead to charge distributed non-symmetrically between the two molecules in a dimer,^{6,21} producing a dipole. This can lead to a broken symmetry ground state, so called “paired electron solid”²¹ or “quantum dipole solid”⁶ where the dipoles order forming a ferroelectric state (Fig.4.1 d).²¹ In contrast to a displacive ferroelectric, a change in the underlying lattice is not necessary in this case. It was suggested,⁶ that dipoles can fluctuate in a quantum dipole liquid (Fig.4.1 e) and be an explanation of the spin liquid state observed in a triangular lattice κ -(BEDT-TTF)₂Cu₂(CN)₃. However, the evidence for fluctuating quantum dipoles in this material remains elusive.^{45,46}

Here we elucidate properties of the quantum dipole liquid state in a triangular lattice Mott insulator^{1,32} (Fig.4.1 b) κ -(BEDT-TTF)₂Hg(SCN)₂Br (κ -Hg-Br) (T_{MI} = 80 K^{10,47}) by a comparison to an isostructural compound κ -(BEDT-TTF)₂Hg(SCN)₂Cl (κ -Hg-Cl) which

¹bis(ethylenedithio)tetrathiafulvalene

CHAPTER 4. STUDY OF THE GROUND STATE OF κ -HG-BR

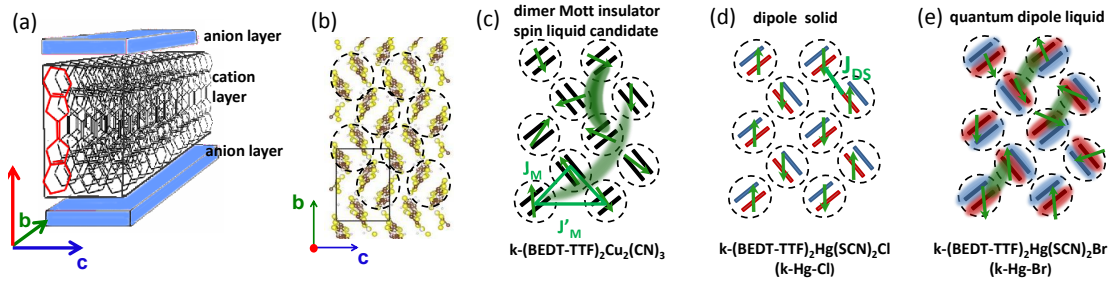


Figure 4.1: (a) Schematic structure of BEDT-TTF based crystal, in the BEDT-TTF-based cation layer the molecule is highlighted in red; (b) Structure of BEDT-TTF layer in (bc) plane of κ -Hg-Cl crystal as determined from X-ray diffraction.¹ BEDT-TTF molecules are bound in dimers as highlighted by circles. These dimer sites form anisotropic triangular lattice. (c) Schematic structure of BEDT-TTF layer in a dimer Mott insulator on an anisotropic triangular lattice formed by $(\text{BEDT-TTF})_2^{+1}$ sites with $S=1/2$ (spins depicted by green arrows) and magnetic exchange between sites J_M and J'_M . The model is relevant to the spin liquid candidate κ -(BEDT-TTF)₂Cu₂(CN)₃ with $J_M/J'_M=0.64$.² (d) Schematic structure of BEDT-TTF layer in case of dipole solid (paired electron crystal²¹). Within $(\text{BEDT-TTF})_2^{+1}$ dimer sites charge-rich and charge-poor molecules are denoted by red and blue colour respectively. The dimer sites thus possess a dipole moment. J_{DC} is a magnetic interaction between spins (marked by green arrows) on neighboring charge-rich molecules. According to Ref.²¹ spins of the nearest neighbor charge-rich sites will form spin-singlets. This situation is related to κ -Hg-Cl. (e) Schematic structure of BEDT-TTF layer in case of the quantum dipole liquid. The charge is fluctuating between the molecules in $(\text{BEDT-TTF})_2^{+1}$ dimers, as denoted by blurry red and blue ovals, leading to electric dipoles fluctuation. Relevant spins also show fluctuations. This situation is related to κ -Hg-Br.

shows signatures of a quantum dipole solid below 30 K,^{1,47} and suggest what parameter may control their ground state.

4.2 Results: Raman scattering data

4.2.1 Raman Spectra of Vibrational Modes

We first use Raman molecular vibrational spectroscopy to follow the distribution of charge on the lattice of these systems through the metal-insulator transition. The on-molecule charge is probed by measuring the frequency of the central C=C molecular bond vibration (ν_2) (Fig.4.2 e), which changes by $\sim -140 \text{ cm}^{-1}$ when the charge state changes from $(\text{BEDT-TTF})^0$ to $(\text{BEDT-TTF})^{+1}$.^{13,36} This is a result of a lengthening of the central C=C bond of the molecule when more charge occupy the highest occupied molecular orbital (HOMO). To emphasize the changes due to charge effects we also follow the temperature dependence of the ν_3 mode at 1470 cm^{-1} (Fig. 2) which involves C=C deformations but is known not to be coupled to the HOMO. It stays a narrow single line through the measured temperature range for both materials.

For κ -Hg-Cl a single ν_2 band at about 1490 cm^{-1} is observed in the high temperature metallic state, while in the insulating state below $T_{CO}=30 \text{ K}$ ν_2 is split into two bands at 1475 and 1507 cm^{-1} (see Fig.4.2 a). The difference in frequencies of the two modes is much higher than expected for a structural phase transition, but corresponds to charges redistributed within the $(\text{BEDT-TTF})_2^{+1}$ dimer as $+0.4e$ on one molecule, and $+0.6e$ on the other^{1,13} which breaks the inversion symmetry in a $(\text{BEDT-TTF})_2^{+1}$ dimer creating an electric dipole. This result confirms that the ground state of κ -Hg-Cl is an order of electric dipoles localized on $(\text{BEDT-TTF})_2^{+1}$ dimer sites,¹ so-called dipole solid.⁶

CHAPTER 4. STUDY OF THE GROUND STATE OF κ -HG-BR

In contrast, for κ -Hg-Br a single ν_2 mode observed in the whole studied temperature range suggests a symmetric dimer with both molecules carrying half a hole (BEDT-TTF)^{+0.5} on average. However, the width of ν_2 band shows abnormal behaviour on cooling. Line widths of phonons are determined by decay mechanism,⁴⁸ disorder and dynamics of the lattice and charge system. For example, a width of ν_3 vibrational band of BEDT-TTF molecule is determined by decay processes into lower-frequency modes and decreases down to about 5 cm⁻¹ at 10 K (see Fig.4.2 d). In contrast, the width of ν_2 goes through a minimum of 16 cm⁻¹ at around 80 K, and increases again up to 20 cm⁻¹ at 10 K (see Fig.4.2 c,d). This behaviour of ν_2 band excludes possibility of structural changes or structural disorder as its origin. Another possible reason for an increased line width which we will consider is charge fluctuations.^{12,49}

In the spectra of κ -Hg-Br ν_2 mode hardens on cooling similar to κ -Hg-Cl. At temperatures between 150 and 100 K we observe a small change of a slope of the temperature dependence of the position of the ν_2 mode. This change occurs still in the metallic state.¹⁰ The change is close to the size of an error with which we determine parameters of the bands. Here the size of triangle/rhombus with which the data are plotted depict the size of the error bars. A similar change of a hardening slope was also noted, for example, for κ -(BEDT-TTF)₂Cu[N(CN)₂]Br in Ref.⁵⁰ A reason for the small change of hardening behaviour could be the following (i) As mentioned in Ref.,⁵⁰ hardening depends on the compression of the lattice, thus changes in the latter can define it. At this point no such precise temperature dependence of the crystal structure has been measured. (ii) While there

CHAPTER 4. STUDY OF THE GROUND STATE OF κ -HG-BR

is a good understanding of the dependence of the frequency of ν_2 mode on the charge distribution on the lattice in the insulating state, at this point it is not clear how this frequency would change due to interactions of this phonon with itinerant electrons. These interactions can be a reason for the change of behaviour.

We used Eq. 1 to reproduce ν_2 line shapes for low temperature κ -Hg-Cl and κ -Hg-Br and also some line shapes which are not present in experimental data, however illustrate the evolution of the line shape in the “two-sites jump model”. The results of our calculations are presented in Fig.4.2b. Parameters for which the calculations are done are listed in the Table 4.1.

In Fig.4.4a we present temperature dependence of parameters of ν_3 and charge-sensitive ν_2 vibrations for κ -Hg-Cl. ν_3 band shows normal hardening on cooling and a decrease of the width, with the temperature dependence coinciding with that for κ -Hg-Br. If no coupling to electronic or magnetic excitations is present, the main process which defines relaxation of a phonon excited state is scattering on lower frequency phonons with frequency denoted here ω_0 . Respectively, a decrease of a line width of a phonon on cooling is determined by a thermal population of the phonon levels ω_0 involved in the scattering process: $\Gamma(T) = \Gamma_0 + \alpha(e^{\frac{\hbar\omega_0}{k_B T}} - 1)^{-1}$, where Γ_0 is temperature-independent scattering rate defined by disorder, and α is a probability of the decay.^{48,50} A decrease of the width of ν_3 is described well by this formula with $\omega_0=150 \text{ cm}^{-1}$, which suggest the most probable decay processes. Our results coincide with that for κ -(BEDT-TTF)₂Cu[N(CN)₂]Br in Ref.⁵⁰

The width of the charge-sensitive ν_2 in the spectra of κ -Hg-Cl decreases below that of

CHAPTER 4. STUDY OF THE GROUND STATE OF κ -HG-BR

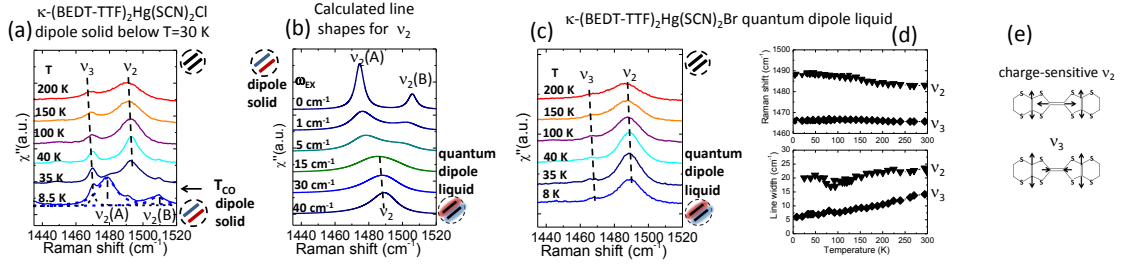


Figure 4.2: (a)-(c) Raman spectra in the region of C=C vibrations of BEDT-TTF: (a) Temperature dependence of the κ -Hg-Cl spectra in the region of ν_2 and ν_3 modes. Note the splitting of ν_2 mode in the dipole solid (charge ordered) state at 8 K with frequencies corresponding to $\text{BEDT-TTF}^{+0.4}$ and $\text{BEDT-TTF}^{+0.6}$. (b) Shape of ν_2 mode calculated by two-sites jump model, see Eq. 3.12 (SI). The upper spectrum is of a static system (ω_{ex}) with bands corresponding to $\text{BEDT-TTF}^{+0.4}$ and $\text{BEDT-TTF}^{+0.6}$ as in dipole solid state of κ -Hg-Cl. Note that on the increase of exchange frequency ω_{ex} the bands widen and move close to each other. The lower two spectra at $\omega_{ex} = 30$ and 40 cm^{-1} reproduce the ν_2 shape of κ -Hg-Br at 8 and 35 K correspondingly, taking into account the natural width Γ for the relevant temperature. (c) Temperature dependence of the κ -Hg-Br spectra in the region of ν_2 and ν_3 modes. Note that the ν_2 band does not split but shows some widening at lowest temperature. (d) Temperature dependence of centerfrequency (upper panel) and line width (lower panel) for ν_2 (triangles) and ν_3 (diamonds) modes for κ -Hg-Br. Note that line width of ν_2 for κ -Hg-Br goes through a minimum at around 75 K, while it decreases continuously for ν_3 . (e) BEDT-TTF molecule with marked movements of atoms on ν_2 and ν_3 vibration.

κ -Hg-Br on cooling down to approximately 40 K, and then shows a weak increase till the compound reaches the ordering transition at 30 K, and decreases again below the transition as expected in the ordered state.

4.2.2 Low-frequency Raman spectra of κ -Hg-Br and κ -Hg-Cl

In Fig. 4.2 and 4.4 we present temperature dependence of the Raman scattering spectra for κ -Hg-Br and κ -Hg-Cl compounds for A_{1g} and B_{1g} symmetry in the spectral region between 25 and 400 cm^{-1} . It shows that (i) Similar to A_{1g} for κ -Hg-Br, the background feature due to the collective mode at about 40 cm^{-1} appears also in spectra of κ -Hg-Br in B_{1g} symmetry channel. (ii) The low frequency phonons in κ -Hg-Br B_{1g} spectra remain broad, which can be explained by an interaction of these phonons with the collective mode. This is in contrast with spectra of κ -Hg-Cl and κ -Hg-Br in A_{1g} polarization, where at low frequencies narrow phonon modes are superimposed on the collective mode background. (iii) Some drop of intensity in κ -Hg-Cl spectra between 35 and 7 K is due to an opening of a gap due to an ordering transition.

Polarization dependence is an important way to characterize excitations observed in Raman scattering.³⁸ For D_{4h} symmetry a clear separation of A_{1g} (x^2+y^2), B_{1g} (x^2-y^2), and B_{2g} (xy) polarization is expected for electronic and magnetic excitations. Spectra of some materials can be mapped on D_{4h} symmetry and understood within it even if the symmetry of the unit cell is lower. A good example is the antiferromagnetically ordered organic compound κ -(BEDT-TTF)₂Cu[N(CN)₂]Cl, where in a monoclinic unit cell (BEDT-TTF)₂⁺¹ dimers form a weakly frustrated square lattice, and two-magnon Raman excitations in that material follow the symmetry selection rules expected for D_{4h} .

CHAPTER 4. STUDY OF THE GROUND STATE OF κ -HG-BR

In the materials studied in this work, the symmetry of the unit cell is monoclinic as well, however it was shown¹ that the $(\text{BEDT-TTF})_2^{+1}$ dimers in (bc) plane form slightly anisotropic triangular lattice. For D_{3h} point group Raman-active symmetries cannot be fully separated by selecting polarizations. It was shown by numerical calculations, too, that magnetic excitations on a triangular lattice lose their anisotropy between A_{1g} and B_{1g} ,^{17,51} a similar change is expected for electronic excitations. This explains the presence of the collective mode in spectra of κ -Hg-Br in A_{1g} , B_{1g} (xy), and $x^2 - y^2$ which would exist as B_{2g} only in D_{4h} .

On the other hand, polarization dependence of phonons follows the full symmetry of the lattice. Our experimental data suggest that the coupling to the collective mode is larger for B_{1g} phonons than for A_{1g} . This fact can be a realization of the expected anisotropy of the electronic excitation.

4.3 Analysis and Discussion

We estimate the effects of charge fluctuations on the shape of the ν_2 vibration using "two-site jump" model^{12,49} presented by Eq. 1. In this model, we consider $+0.6e$ and $+0.4e$ charged molecules observed in the ordered state of κ -Hg-Cl as two static species. They are characterized by frequencies of ν_2 vibrations $\nu_2[\text{BEDT-TTF}^{+0.4}] = 1475 \text{ cm}^{-1}$ and $\nu_2[\text{BEDT-TTF}^{+0.6}] = 1507 \text{ cm}^{-1}$. Their natural width Γ depends on temperature through the lifetime of the measured excited state and is expected to be the same as that of ν_3 . The

CHAPTER 4. STUDY OF THE GROUND STATE OF κ -HG-BR

system can jump between these two states with a frequency of $\omega_{EX}=1/\tau$, where τ is a life time of each state defined by the exchange. As an exchange rate ω_{EX} between these two states increases, the shape of the resulting spectra changes as shown in Fig.4.2 c. The two original bands get wider, move together and at high enough rate ω_{EX} merge into single band. The calculated spectrum at $\omega_{EX}=0$ reproduces the doublet shape of ν_2 for κ -Hg-Cl at 8.5 K (Fig.4.2 a,b). The spectra calculated for $\omega_{EX} = 40$ and 30 cm^{-1} reproduce the shape of the ν_2 band in κ -Hg-Br spectra, where the width of ν_2 increases from 16 to 20 cm^{-1} on cooling below 80 K and the band gains slight asymmetry (Fig.4.2 b,c). These results suggest that in κ -Hg-Br charges fluctuate between two molecules in a dimer with frequency ω_{EX} which slightly decreases on cooling. In other words, electric dipoles in κ -Hg-Br fluctuate with this frequency, forming a quantum dipole liquid state.

Apart from the difference in the ν_2 band behaviour, the phonon Raman spectra of κ -Hg-Br and κ -Hg-Cl are very similar (Fig.4.3 a,b,e), since the compounds possess very similar crystal structural. On cooling, all the bands narrow down to $5\text{-}7 \text{ cm}^{-1}$, including the low frequency lattice phonons, which are well distinguished in low temperature spectra in Fig.4.3 a,b below approximately 100 cm^{-1} . In the spectra of κ -Hg-Br the somewhat widened by few wavenumbers phonons, some of them demonstrating so-called Fano shape, are superimposed on a much wider background band observed in A_{1g} and B_{1g} symmetries (see A_{1g} symmetry spectra in Fig.4.3, B_{1g} symmetry in Fig. SI). This asymmetric feature with a maximum around 40 cm^{-1} (see spectra with phonons extracted in Fig.4.3 c) with the width at half maximum of about 40 cm^{-1} gains intensity below 100 K, when κ -Hg-Br

CHAPTER 4. STUDY OF THE GROUND STATE OF κ -HG-BR

enters the insulating state, and shows weak softening at the lowest temperature. Apparently, this wide feature observed only in κ -Hg-Br spectra originates from a different scattering channel than phonons. Potential other scattering channels are electronic or magnetic excitations on a triangular lattice of $(\text{BEDT-TTF})_2^{1+}$ dimers. On a triangular lattice polarizations of electronic or magnetic excitations cannot be completely disentangled to elucidate the origin of the excitations, in contrast to a square lattice.³⁸

Magnetic excitations are expected in the Raman response of a Mott insulator with ordered spins or even spins developing short range correlations.^{16,37,38,52} In Mott insulators based on $(\text{BEDT-TTF})_2^{+1}$ dimers magnetic excitations are observed both in Raman spectra of an antiferromagnetically ordered state on a square lattice³⁷ and in a spin liquid candidate on triangular lattice κ - $(\text{BEDT-TTF})_2\text{Cu}_2(\text{CN})_3$ (see Fig.4.3 e). The spectra of the latter show a continuum of magnetic excitations below 600 cm^{-1} , as marked in the spectra in Fig 3 e by a shaded area. The position of the continuum is defined by the value of J and geometry of the lattice.³⁸ For κ - $(\text{BEDT-TTF})_2\text{Cu}_2(\text{CN})_3$ it is in agreement with Hubbard-model-based calculations for the magnetic response of $S=1/2$ on a anisotropic triangular lattice with $J_M=250\text{ K}$.¹⁶

It is clear at this point, that magnetic interactions in a dipole solid, and possibly quantum dipole liquid would be re-normalized in comparison to a simple $(\text{BEDT-TTF})_2^{+1}$ dimer Mott insulator with charge symmetrically distributed on a dimer. Ref.⁶ suggests a re-normalization and a decrease of J in a quantum dipole liquid compared to a simple dimer Mott insulator, however without estimating J values. A simple argument suggests that in a

CHAPTER 4. STUDY OF THE GROUND STATE OF κ -HG-BR

dipole solid magnetic interactions occur between charge-rich molecules of the neighboring dimers, while in a simple Mott insulator the interactions are between dimer lattice sites, as is schematically shown in Fig.4.3 e. An estimate provided by a tight-binding approximation as $J = \frac{4t^2}{U}$, where t is a transfer integral, and U is on-molecule Coulomb repulsion, yields the value of about $J_{DS} = 80 K$ for a dipole solid, considerably smaller compared to $J_M = 250 K$ ²⁹ for a simple dimer Mott insulator, where the on-dimer U defines magnetic interactions. Here the Coulomb repulsion parameters, as well as transfer integrals are estimated from the optical conductivity spectra,⁵³ and the difference is produced mainly by a variation between the values of U in these two models. Lower J would result in a lower ordering temperature, and a spectrum of magnetic excitation shifting to lower frequencies. However, the maximum of the observed background is around 40 cm^{-1} is found below the expectant J_{DS} value, which is too low in frequency below the expected J_{DS} value to interpret it as purely magnetic excitations.

Another possibility is an assignment of this mode as a collective excitation associated with dipole fluctuations. Dipole fluctuations with frequency of about $\omega_{EX} = 40 \text{ cm}^{-1}$ are detected through the line shape analysis of charge-sensitive vibrations. If these fluctuations are a collective phenomena, we would expect a collective mode at about 40 cm^{-1} . The low-frequency mode observed in κ -Hg-Br thus is a good candidate for a collective response of dipole fluctuations. Optically detected collective modes associated with charge fluctuations are found in the metallic state close to a charge ordering metal-insulator transition in organic conductors^{54,55} and in under-doped high temperature cuprate superconductors.⁵⁶ In

CHAPTER 4. STUDY OF THE GROUND STATE OF κ -HG-BR

an insulating state, the closest analogy would be a soft mode close to the transition into the ferroelectric state in displacive ferroelectrics such as SrTiO_3 . To the best of our knowledge a collective mode due to fluctuations of electric dipoles in a Mott insulator is observed by ground state spectroscopy for the first time here. A comparatively small width of the band, as well as its increase in intensity and low-frequency shift below $T_{MI}=80$ K distinguishes it from a Boson peak observed in glasses⁵⁷ and supports an interpretation in terms of a fluctuating system of dipoles versus charge glass. An absence of glassy behavior is also supported by low frequency dielectric response of κ -Hg-Br.¹⁰

Fluctuations of electric dipoles coupled to $S=1/2$ spins on a triangular lattice of $(\text{BEDT-TTF})_2^{+1}$ dimers have been suggested as a mechanism for spin-liquid behaviour.^{6,41} Ref.⁴¹ discusses the coupling between the dipole and magnetic degrees of freedom within the Kugel-Khomskii model, showing an analogy between the fluctuating dipole liquid and orbital liquid.^{4,58} This model suggests that at a certain frustration J'/J and spin-charge coupling K values, spin order in a system is destabilized, and would produce mixed spin-charge excitations. To understand if the collective mode observed by us in κ -Hg-Br originates purely in dipole fluctuations or in mixed charge-spin excitations theoretical calculations of the excitation spectrum for such a system would be of great importance.

Our heat capacity data suggest the presence of itinerant excitations in κ -Hg-Br but not in κ -Hg-Cl. The heat capacity C_p of κ -Hg-Br and κ -Hg-Cl was measured in the temperature range between 40 K and 100 μK . The temperature dependence of heat capacity for these compounds is overlapping within the error of the measurements in the temperature range

CHAPTER 4. STUDY OF THE GROUND STATE OF κ -HG-BR

above 6 K (Fig.4.3 d), but for the feature at 30 K in the temperature dependence for the C_p of κ -Hg-Cl indicating the charge order transition. The heat capacity $C_p = \beta T^3 + \gamma T$ of both compounds shows basically same bosonic contribution $\beta = 19.0 \pm 2.5 \text{ mJ K}^{-4} \text{ mol}^{-1}$. This is natural, since it is determined predominantly by phonons and vibrations of BEDT-TTF molecules which are very similar for the studied compounds. The difference between the two materials appears below about 6 K, where for κ -Hg-Br C_p shows a linear term $\gamma = 13.8 \pm 3.1 \text{ mJK}^{-2} \text{ mol}^{-1}$ (inset in Fig.4.3 d). Spinon excitations can produce the linear term in heat capacity^{20,59} and thus suggest a spin-liquid behaviour of κ -Hg-Br. For κ -Hg-Cl $\gamma = 0$ within the precision of our measurements.

An order of electric dipoles represented by κ -Hg-Cl does not necessary imply magnetic order.⁶ However, an approach of Ref.²¹ which includes antiferromagnetic interactions as a driving force for the charge order on a frustrated dimer lattice suggests a spin singlet ground state. A single phase transition observed at 30 K can be an evidence of simultaneous electric dipole ordering and singlet formation in κ -Hg-Cl. On the other hand, the temperature of spin ordering can be lower than that of the charge order, as is observed in one-dimensional materials, and suggested by calculations.⁶⁰ Since heat capacity is found not to be always sensitive to magnetic phase transitions in these two-dimensional materials, see for example,⁶¹ further studies such as NMR are necessary to identify the magnetic ground state of κ -Hg-Cl. Paired electron crystal proposed as a ground state of κ -Hg-Cl¹ can be regarded as a variation of valence bond solid.^{4,21} In these terms, the quantum dipole liquid in κ -Hg-Br can be a realization of a resonant valence bond state.⁶²

CHAPTER 4. STUDY OF THE GROUND STATE OF κ -HG-BR

The quantum dipole liquid was suggested as one possible explanation of the origin of the spin liquid state in κ -(BEDT-TTF)₂Cu₂(CN)₃,⁶ however our work shows that this material does not demonstrate the fingerprints of this state. Its spectrum of magnetic excitations is well understood within a model of spin 1/2 on a triangular lattice with $J=250$ K (Fig.4.3, Ref.¹⁶). There is a recent suggestion⁶³ that κ -(BEDT-TTF)₂Cu₂(CN)₃ experiences a lowering of magnetic dimensionality due to destructive interference of magnetic interactions in one of the directions. A necessary test would be a comparison of magnetic excitation spectra of this model to available experimental Raman scattering data on magnetic excitations in κ -(BEDT-TTF)₂Cu₂(CN)₃ and antiferromagnetically ordered BEDT-TTF based material. At this point it is clear that the spectrum of collective excitations in κ -Hg-Br is very different from that of κ -(BEDT-TTF)₂Cu₂(CN)₃. Basing on that we can suggest, that κ -(BEDT-TTF)₂Cu₂(CN)₃ is a regular dimer Mott insulator with homogeneous distribution of charge on (BEDT-TTF)₂¹⁺ dimer on a relevant time scale. If the quantum dipole liquid model is relevant to κ -(BEDT-TTF)₂Cu₂(CN)₃ at all, it puts this compound quite far from a quantum phase transition into a dipole solid state. Tuning between quantum dipole solid and quantum dipole liquid can be done by a change of t_b/t_d ratio, where t_b is an overlap integral between the dimers, and t_d an intra-dimer one according to theoretical approach of Ref.⁶ Indeed, t_d is found to be larger for κ -(BEDT-TTF)₂Cu₂(CN)₃ than for κ -Hg-Cl.¹ The existing experimental data do not give a straightforward evidence of tuning from a dipole liquid to a dipole solid by hydrostatic and chemical pressure for κ -Hg-Br and κ -Hg-Cl. While a charge ordered state in κ -Hg-Cl is suppressed by external pressure of about

CHAPTER 4. STUDY OF THE GROUND STATE OF κ -HG-BR

1 kbar,⁶⁴ the unit cell of κ -Hg-Br is somewhat larger than that of κ -Hg-Cl. Calculation of electronic structure of these materials and its change with pressure, as well as further explorations of magnetic properties are necessary for further understanding of the phase diagram.

4.4 Conclusions

In conclusion, we demonstrated a quantum dipole liquid state in κ -Hg-Br, and found the frequency of dipole fluctuations at around 40 cm^{-1} both using vibrational spectroscopy and observing a collective mode associated with the fluctuations. While the frequency of the collective mode is similar to that of dipole fluctuations, a mixed charge-spin excitations are also a possible explanation. A presence of a linear term in heat capacity down to $100 \text{ } \mu\text{K}$ suggests a presence of spinon excitations in κ -Hg-Br. Magnetic Raman scattering in κ -(BEDT-TTF)₂Cu₂(CN)₃ suggests that this material can be well understood within dimer Mott insulator model and does not show the fingerprints of quantum dipole liquid.

CHAPTER 4. STUDY OF THE GROUND STATE OF κ -HG-BR

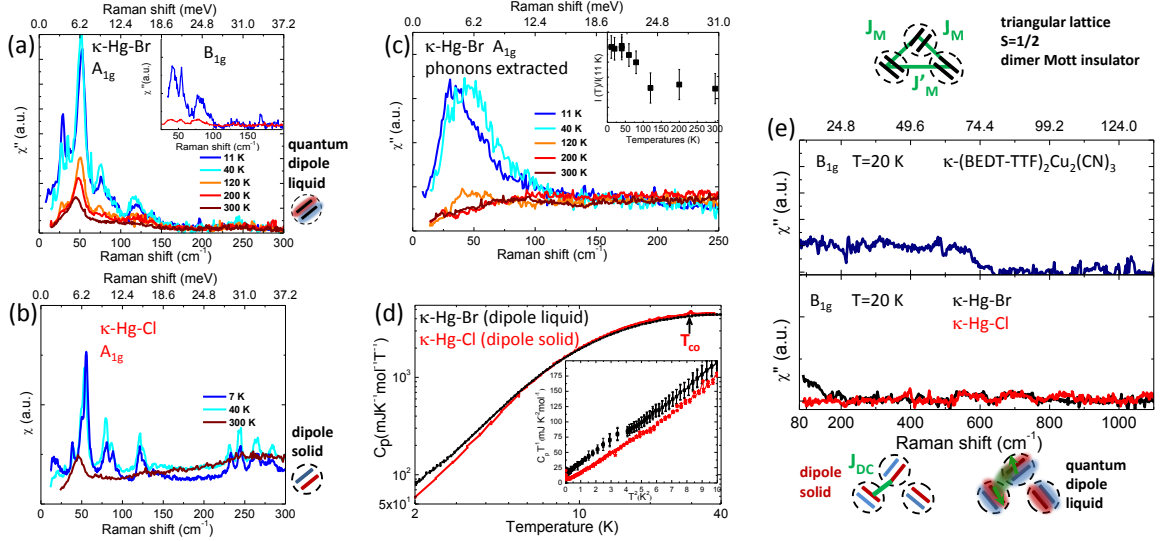


Figure 4.3: (a)-(b) Temperature dependence of low-frequency Raman spectra of (a) κ -Hg-Br and (b) κ -Hg-Cl in A_{1g} symmetry. Phonons are found at similar frequencies for both compounds. In the spectra of κ -Hg-Br a background develops at temperatures below 100 K. Spectra at 300 and 11 K for κ -Hg-Br for B_{1g} symmetry are shown in the inset in (a). The collective mode is observed in B_{1g} with more prominent coupling to the phonons. (c) Temperature dependence of the collective mode in A_{1g} symmetry for κ -Hg-Br determined by extracting phonons from the full Raman spectrum. The inset shows the temperature dependence of the normalized intensity of the collective mode. (d) Temperature dependence of heat capacity for κ -Hg-Cl (red line) and κ -Hg-Br (black line) below 40 K. C_p shows similar temperature dependence for these materials below 30 K. The difference in the behaviour is observed below approximately 6 K. The inset shows low temperature data with linear behaviour of heat capacity for κ -Hg-Br. (e) Raman spectra in B_{1g} polarization at 20 K in the range between 800 and 1100 cm^{-1} with phonons and luminescence background extracted for κ -(BEDT-TTF) $_2$ Cu $_2$ (CN) $_3$ (upper panel) and κ -Hg-Br and κ -Hg-Cl (lower panel). Schematic pictures of the relevant models with different charge distribution are shown. The spectra of the dimer Mott insulator on the triangular lattice κ -(BEDT-TTF) $_2$ Cu $_2$ (CN) $_3$ (upper panel) demonstrate magnetic excitations below approx. 600 cm^{-1} . This feature is absent in the spectra of both κ -Hg-Br (black) and κ -Hg-Cl (red). The increase of intensity in the spectra of κ -Hg-Br below 200 cm^{-1} is due to the collective mode fully shown in panel (a).

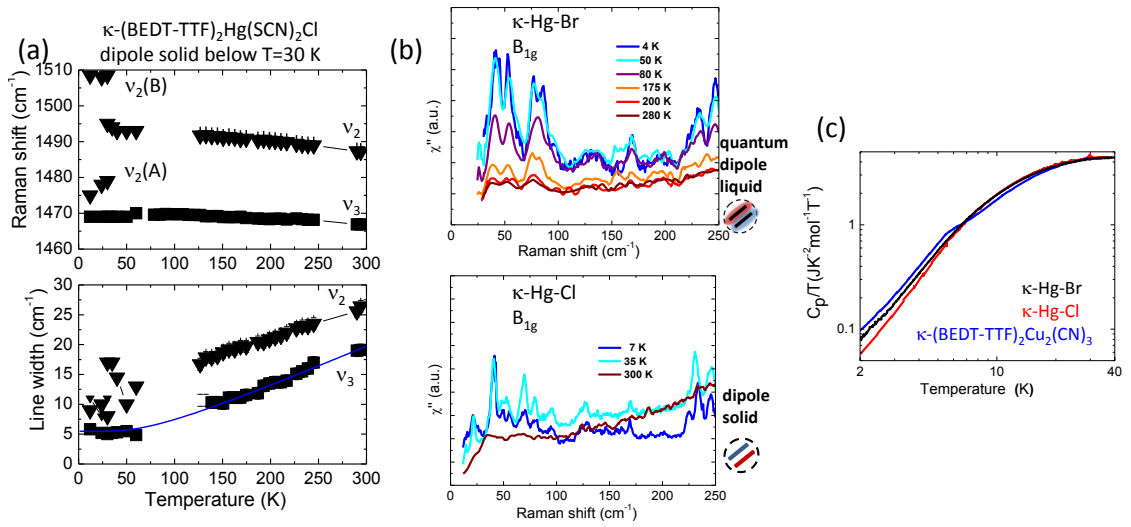


Figure 4.4: (a) Temperature dependence of parameters of ν_2 and ν_3 vibrational modes for κ -Hg-Cl. Blue line in the lower panel shows a fit of the width of ν_3 by $\Gamma(T) = \Gamma_0 + \alpha(e^{\frac{\hbar\omega_0}{k_B T}} - 1)^{-1}$, with $\Gamma_0=5.5$ cm⁻¹, $\alpha=15$, $\omega_0=150$ cm⁻¹. (b) Temperature dependence of (*bc*) spectra for κ -Hg-Br (upper panel) and κ -Hg-Cl(lower panel). Note a collective mode which appears at low frequencies in the spectra of κ -Hg-Br, similar to *bb* polarization. The phonons are widened by the interaction with the collective mode. (c) Comparison of temperature dependence of heat capacity of κ -Hg-Br and κ -Hg-Cl with that of κ -(BEDT-TTF)₂Cu₂(CN)₃.

CHAPTER 4. STUDY OF THE GROUND STATE OF κ -HG-BR

Table 4.1: List of the parameters used in the formula Eq. 1 SI for the calculations of the line shapes presented in Fig.4.2b of the paper.

$\omega_{EX}, \text{cm}^{-1}$	ω, cm^{-1}	Δ, cm^{-1}	Γ, cm^{-1}	a_p	a_R
0	1490	15.5	6	2.05	3.56
1	1490	15.5	6	2.05	3.56
5	1490	15.5	6	2.05	3.56
15	1490	15.5	6	2.05	3.56
30	1490	15.5	6	2.05	3.56
40	1490	15.5	7	2.05	3.56

Chapter 5

Ground state of κ -Hg-Cl

5.1 Introduction

organic conductors are the subject of intense study especially theoretically where a range of exotic ground states were proposed. Examples of new proposed ground states are pinball, three-fold charge metals and other states where charge frustration comes into play,³ Such materials have interesting phase diagrams with complex charge phases due to competitions between ground states. Such states are mostly described within the extended Hubbard model for quarter filled materials. In this chapter we observed a crossover to a new state as we lowered temperature of κ -Hg-Cl.

κ -Hg-Cl is a quasi-two dimensional material where there is minimal inter-layer interaction. The material is composed of alternating layers of cations and anions. The cation layer is made up of the ET molecule that defines the electronic and magnetic behavior of

CHAPTER 5. GROUND STATE OF κ -HG-CL

the material. Within the cation layer, the ET molecules are arranged in such a way to form κ -phase where every two molecules form a dimer and every dimer is considered a lattice site. Every two ET molecules give one electron to the Hg-Cl molecule. As a result, every lattice site has an unpaired hole on a dimer $(BEDT - TTF)_2^{+1}$. In systems where there is strong intradimer bond, a dimer is considered a lattice site and thus the system is considered half filled. There are 2 dimers (4 molecules) in a unit cell, where different parameters t_d, t_i, t_j, V_d, V_i and V_j control the behavior of the material. In such organic materials, electron-electron interaction is strong enough to prevent the double occupation of a state. Materials exhibiting such behavior are called Mott insulator. However, in cases of charge order where the charge doesn't distribute equally within a dimer, the system is treated like a quarter filled system.

κ -Hg-Cl exhibit MIT transition at 30 K that is driven by charge order. In the metallic state, the charge on $(BEDT - TTF)_2^{+1}$ is equally distributed on the two molecules within the dimer and is free to hop between dimers. As the material goes through phase transition, the charge on the molecules within a dimer deviate from 0.5e to 0.6e and 0.4e on charge rich and charge poor molecules in the insulating state. Such charge configuration give rise to electric dipoles that give rise to a ferro-electric state when these dipoles order. The configuration or long range order of the dipoles in theory could be either the degenerate chain stripe or the unique checkerboard stripe depending on the parameters V and V' , see fig. 5.1. Other configurations were proposed by²¹ such as paired electron crystal. However, it was proposed, Ref,¹ that the charge order is in the stripe configuration as shown in fig.3.5,

CHAPTER 5. GROUND STATE OF κ -HG-CL

Raman spectroscopy was used to probe the charge degree of freedom for κ -Hg-Cl. For every molecule there are 72 vibrational modes, the mode of interest is ν_2 because it is sensitive to the charge density on the central C=C molecular bond. As the material is cooled down this charge ordering is manifested by the splitting of the ν_2 band at 1490 cm^{-1} into two modes, $\nu_{2(A)}$ and $\nu_{2(B)}$ at 1475 and 1507 cm^{-1} . The charge on each molecule within the dimer could be inferred from the location of the new bands using a linear relation,¹³ The charge distribution was calculated to be $0.6e$ on the charge rich molecule and $0.4e$ on the charge poor one creating an electric dipole.

High resolution measurements were taken of ν_2 and ν_3 vibrational modes and of low frequency modes. The material showed consistently MIT transition at $\sim 30 \text{ K}$. We noticed that the transition took place at different temperatures, higher temperature on warming. However, such hysteresis was not observed in heat capacity measurements and that agrees with Ref. where they didn't detect any hysteresis in resistivity measurements. Such hysteresis could be attributed to worse thermal conductivity in the insulating state and thus higher temperature of transition. During the transition we noticed mixed state where we could see the gradual decrease in the intensity of ν_2 and increase in the intensity of $\nu_{2(A)}$ and $\nu_{2(B)}$. The frequency of $\nu_{2(B)}$ starts with smaller value and then as the temperature is lowered its intensity increases and its frequency stabilizes at 1498 cm^{-1} , see fig. 5.2. From the frequency we calculated the charges to be $0.6e$ and $0.4e$.

As the temperature is lowered below 10 K , charge order starts to disappear and a redistribution of spectral weight takes place, see fig. 5.2. This behavior is observed on warming

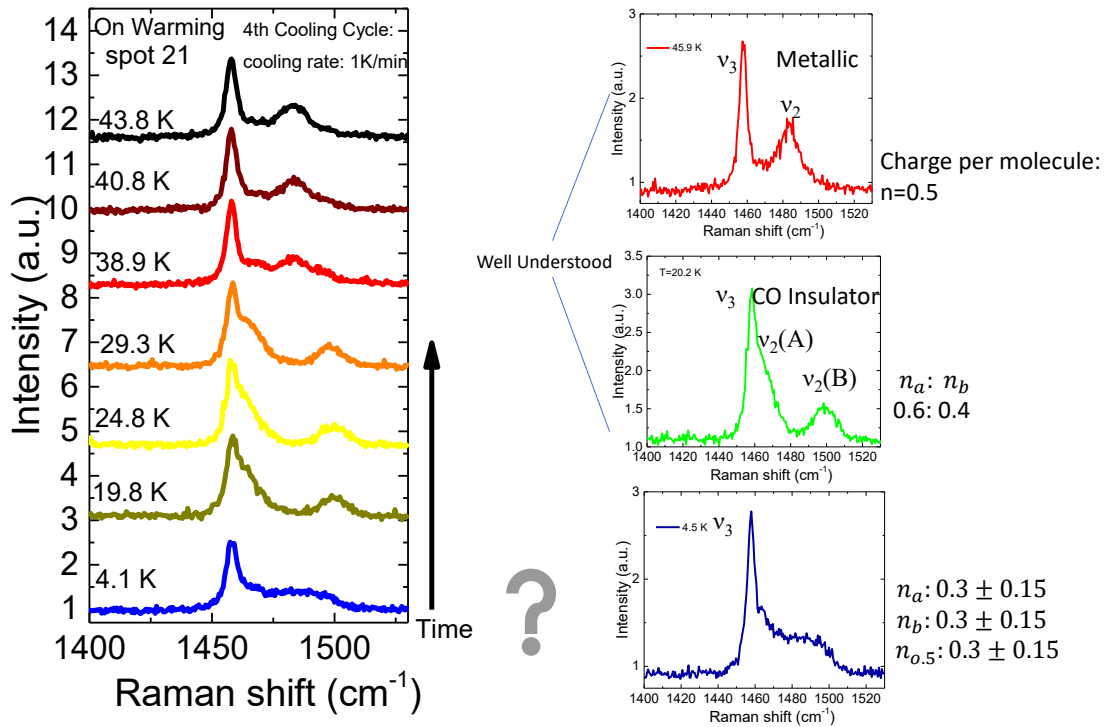


Figure 5.2: a) Temperature dependence of ν_2 , the measurement was taken on warming. b) Shows the three states of κ -Hg-Cl: metallic state in red, charged ordered state in green and new re-entrant state in blue.

and cooling. Also, different cooling rates, 10K/min, 1K/min and 0.2 K/min, produced the same result. Also, we have noticed that some locations below 10K showed less spreading and spectral distribution closer to that of CO; this suggest that the ground state consists of domains. Also, the emv-coupled mode at $\sim 1400 \text{ cm}^{-1}$ was sensitive to such crossover; at MIT transition the intensity of corresponding band increases abruptly but as the temperature is lowered below 10 K its intensity decreases, see Fig. 5.3 a). Similar behavior was detected at $\sim 450 \text{ cm}^{-1}$, see Fig.5.3 b). The significance of these two bands and how they are sensitive to charge redistribution is still under investigation.

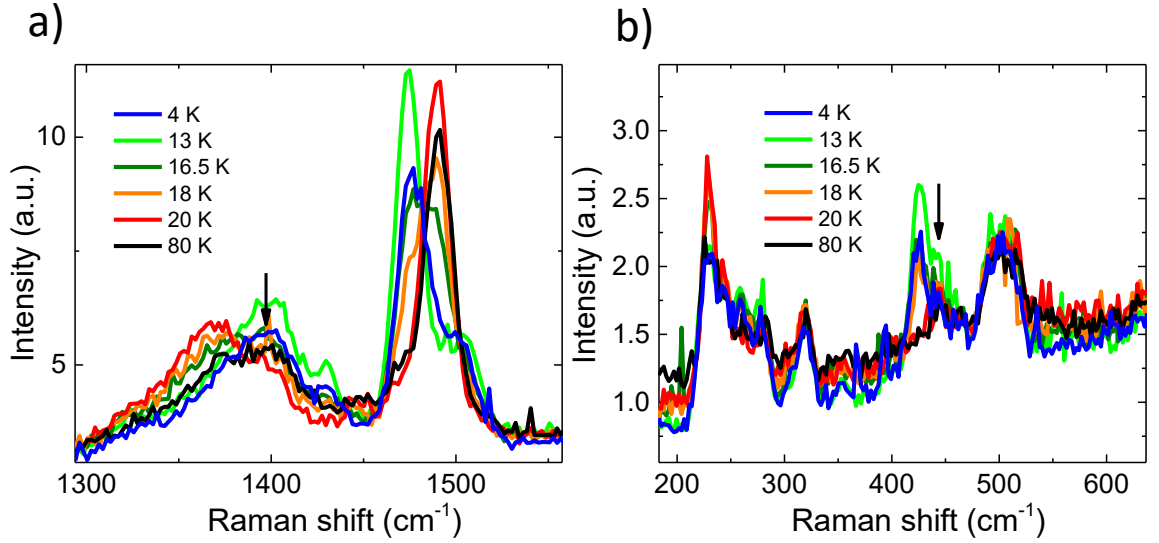


Figure 5.3: a) Temperature dependence of the emv-coupled mode at 1400 cm^{-1} . b) Temperature dependence of the low frequency mode at 450 cm^{-1}

5.3 Discussion

Fitting charge sensitive bands shows that $\nu_{2(A)}$ frequency increases and that of $\nu_{2(B)}$ decreases, suggesting that the charge disproportionation starts to change from $0.6e$ and $0.4e$ to closer to $0.5e$. Also, the mode ν_2 starts to appear again where a significant spectral weight accumulates below 10K . There are few similarities and differences between this new state and the mixed state at the MIT transition; the frequency of $\nu_{2(B)}$ decreases as the temperature is lowered below 10 K which is same behavior at the mixed state where the CO states starts to form. The spectral weight of ν_2 starts to increase gradually but also with increasing width. Unlike in the mixed state, ν_2 , $\nu_{2(A)}$ and $\nu_{2(B)}$ merge together to form a very broad peak. In the mixed state the three bands stay separate. All this suggests that a crossover is taking place at very low temperature.

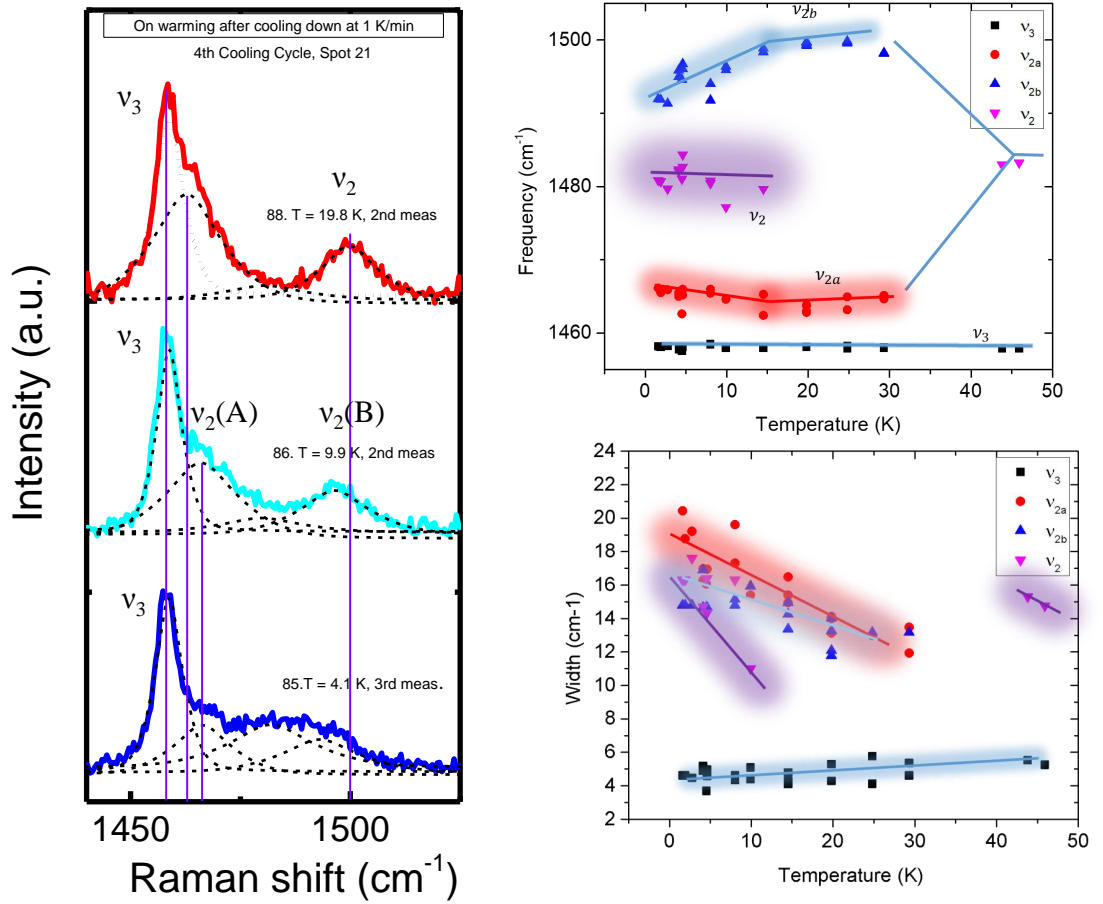


Figure 5.4: a) Raman spectra with Lorentzian fits to the peaks. b) Temperature dependence of the frequency and widths of ν_2 , $\nu_{2(A)}$ and $\nu_{2(B)}$ peaks.

Plots of the frequencies and widths of ν_2 , $\nu_{2(A)}$ and $\nu_{2(B)}$ vs temperature are shown in figure 5.4. $\nu_{2(A)}$ and $\nu_{2(B)}$ bands represent equal number of charge rich and charge poor molecules, but have different spectral weights. To better understand the behavior and configuration of the charges we computed the percentage of the molecules contributing to the intensities of the bands. We fitted the bands to a Lorentzian peaks and then calculated the area of those peaks using the equation $1.59 \times w \times h$ where w is the full width at half maximum and h is the intensity. We then normalized the areas of ν_2 , $\nu_{2(A)}$ and $\nu_{2(B)}$ using that

CHAPTER 5. GROUND STATE OF κ -HG-CL

of ν_3 . Taking the at 19 K the system is in pure charged ordered state and at 50K it is in pure metallic state; we used those spectra to calibrate the spectra and calculate the percentage of molecules with 0.5e, 0.4e and 0.6e at 4 K, see fig. 5.5. We assumed that 100% of molecules contribute to the spectral weight of ν_2 at 50K, and 50% of molecules are charge rich that contribute to the spectral weight of $\nu_{2(A)}$ at 19K. Similarly, 50% of molecules are charge poor that contribute to the spectral weight of $\nu_{2(B)}$ at 19K. By adjusting for the difference in spectral weight we calculated the percentage of molecules contributing to the three bands at 4K. We used the fit in fig.5.5 to calculate such percentages and found that the three charge densities, 0.6e, 0.4e and 0.5e are equally distributed among molecules in the material with each constituting one third of the total number of molecules.

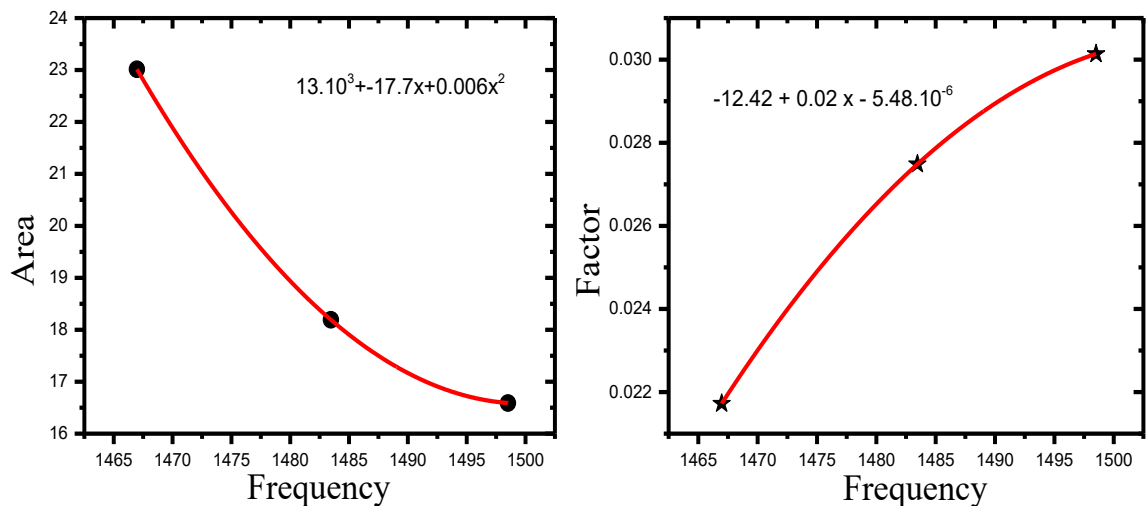


Figure 5.5: a) Fitting the area under the ν_2 , $\nu_{2(A)}$ and $\nu_{2(B)}$ peaks to a polynomial function. b) Fitting the efficiency factors to to calculate the ratio of molecules with certain charge.

There are few theories that could explain the behavior that we are still investigating.

CHAPTER 5. GROUND STATE OF κ -HG-CL

First, it could be charge glass with the charge densities range from $0.4e$ to $0.6e$ randomly distributed among molecules. The redistribution of charges could suggest a re-entrant charge glass. The existence of domains also implies the coexistence of re-entrant charge glass and charge order. However, there was no evidence of Bose peak to imply glassy state. In addition, heat capacity measurements do not show any behavior at very low temperatures other than the lattice contribution $\sim T^3$. Fig. 5.6 shows that heat capacity at cooling rates 0.5K/min and 10K/min are identical which would not be the case if the ground state was a glassy state; i.e. no deviation from the $\sim T^3$ behavior at low temperature after fast cooling. We would expect glassiness or disorder affect Raman and heat capacity at low temperatures especially at very high cooling rates but that behavior was consistently absent.

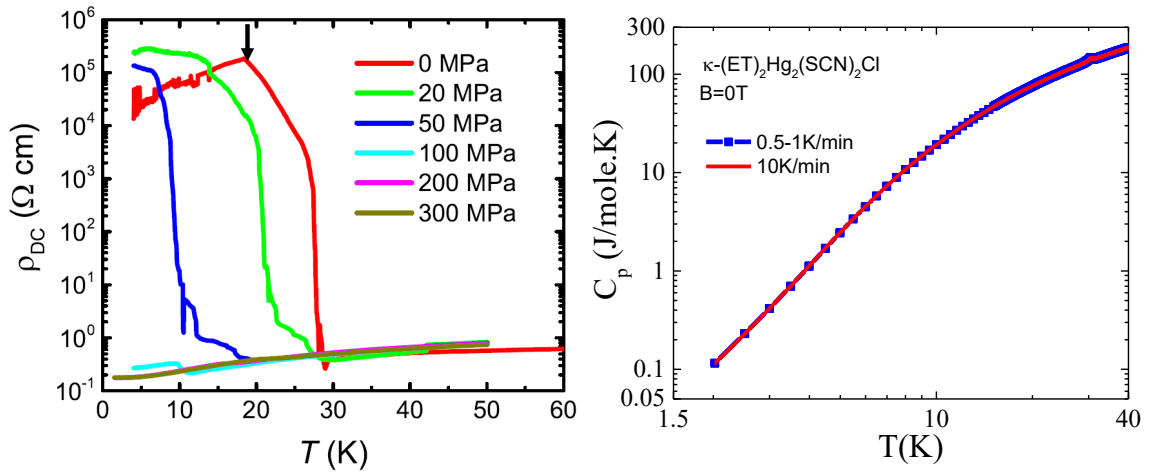


Figure 5.6: a) RT plot of κ -Hg-Cl from Ref.⁸ b) Heat capacity measurement of κ -Hg-Cl under different cooling rates, 0.5K/min (blue) and 10K/min (red)

Another interesting explanation is that charge ordered state crosses over to an exotic metallic state, as suggest by ref.,³ due to charge frustration in quarter filled organic com-

CHAPTER 5. GROUND STATE OF κ -HG-CL

pounds that destroys charge order leading to the coexistence of solid and liquid components of charges. In such ground state, pinball liquid, only third of the charges contribute to the charge order (solid part) and the rest of the charges are mobile (liquid). Such states are ground states in the special case of $V' = V$ due to the higher degeneracy than the charged ordered states. Such exotic metals due to charge frustrations are less conductive than normal metals. This could be suggested as the mechanism of the crossover in our material if we took the resistivity measurements in ref.⁸ into consideration where the resistivity showed a slight decrease at around 10K, see Fig. 5.6. However, heat capacity at low temperatures still doesn't show any deviation from T^3 behavior.

A third possibility is that in the charge ordered state the dipoles are static without any fluctuations within the dimer. As we lower the temperature, the charge starts to fluctuate leading to the decreased difference between frequencies and the emergence of ν_2 . The broad peak could take place due to the large range of exchange frequency ω_{ex} from 0 to 40 cm^{-1} similar to κ -Hg-Br. That possibility is still under investigation.

In conclusion, we took high resolution Raman measurement of κ -Hg-Cl and detected the well understood MIT transition at ~ 30 K. However, as we lower the temperature we detect a re-entrant state where the charge ordered state is destroyed. Our calculations suggest a rough estimate of equal charge distribution among molecules with each third of the molecules have charges 0.5e, 0.4e and 0.6e. Thermal expansion measurement from Ref.⁸ did not detect any change in the crystal constants at the crossover temperature 10K. Similarly, our heat capacity measurement didn't detect any sign of phase transition at 10

CHAPTER 5. GROUND STATE OF κ -HG-CL

K. Also, lattice contributions to heat capacity did not show any change under cooling rates. These measurements suggest that the crossover is not due to change in lattice structure but rather due to frustration because of quantum effects. This, however, is under study; it could be argued that the entropy change is too small to be seen in heat capacity measurements especially for these 2D charge transfer materials.

Chapter 6

Heat Capacity Measurements

Heat capacity of three different materials was measured to compare similarities in phonon contribution and detect any differences. Heat capacity of iso-structures κ -Hg-Cl and κ -Hg-Br were taken at different cooling rates and magnetic fields. Also, measurements of spin liquid compound κ -(BEDT-TTF)₂Cu₂(CN)₃ were taken to compare to literature values of phonon and spinon contributions. The main result is that all three compounds share almost same phonon contribution but have very different low temperature behavior. κ -Hg-Cl had $\sim T^3$ behavior at at very low temperatures while κ -Hg-Br and κ -(BEDT-TTF)₂Cu₂(CN)₃ have comparable values of Sommerfeld coefficient. However, the linear term of κ -Hg-Br changes a little with magnetic field and cooling rates. Below are the results in more detail.

6.1 Results and Discussion

6.1.1 κ -(ET)₂ Cu₂ (CN)₃

We conducted heat capacity measurements on the spin liquid compound κ -(ET)₂ Cu₂ (CN)₃ to verify that the results agree with literature and to compare to heat capacity of our new compounds. The measurements were done using Quantum Design setup based on the relaxation method. We took the first measurement in zero and 5 T field on warming. The sample (0.38 mg) was cooled down at $0.5K/min$ in zero field. Results for κ -(ET)₂ Cu₂ (CN)₃, are shown in fig.6.1, fig.6.2 and fig. 6.3. Fig.6.1 a) is a plot of heat capacity vs temperature; the figure shows the same kink detected by other experiments at 6 K.²⁰ The explanation of that kink is highly speculative and possible interpretations include the onset of spin liquid state. Fig.6.1 b) is a plot of C_p/T vs T^2 for temperature in the range 1.8 K to 3.8 K to show the linear contribution. The red line shows a linear fit to the low temperature portion of the data. The fit to the data is a line with slope that represents cubic contribution due to lattice phonons, and intercept that represent linear contribution to the heat capacity. The coefficient of the linear term (Sommerfeld coefficient) is of the same order of that detected in literature²⁰ with a value around $8.5mJK^{-2}mol^{-1}$ compared to $12mJK^{-4}mol^{-1}$. The lattice contribution $\beta = 21mJK^{-4}mol^{-1}$ is measured by fitting the data to βT^3 and agrees perfectly with values found in literature.

Fig.6.2 shows the effect of magnetic field on the heat capacity. Fig. 6.2 a) is log-log plot of heat capacity vs temperature in zero field (blue curve) and 5T (red curve). The data

CHAPTER 6. HEAT CAPACITY MEASUREMENTS

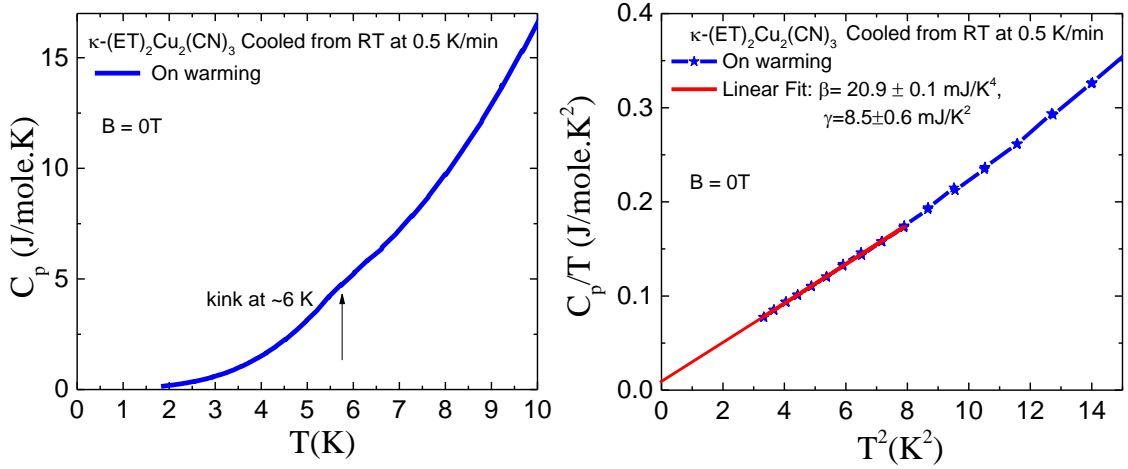


Figure 6.1: a) Plot of C_p vs T of κ -(ET)₂ Cu₂ (CN)₃. There is kink at 6 K that is detected in Ref.²⁰ b) Plot of C_p/T vs T^2 , the linear fit is shown in red.

doesn't show any change in the kink shape or location due to field. In fig. 6.2 b) The black line shows a linear fit to the low temperature portion of the data shown in red (5 T) and blue (0 T) curves. The Sommerfeld coefficient was not suppressed by applying magnetic field which agrees with previous experiments.

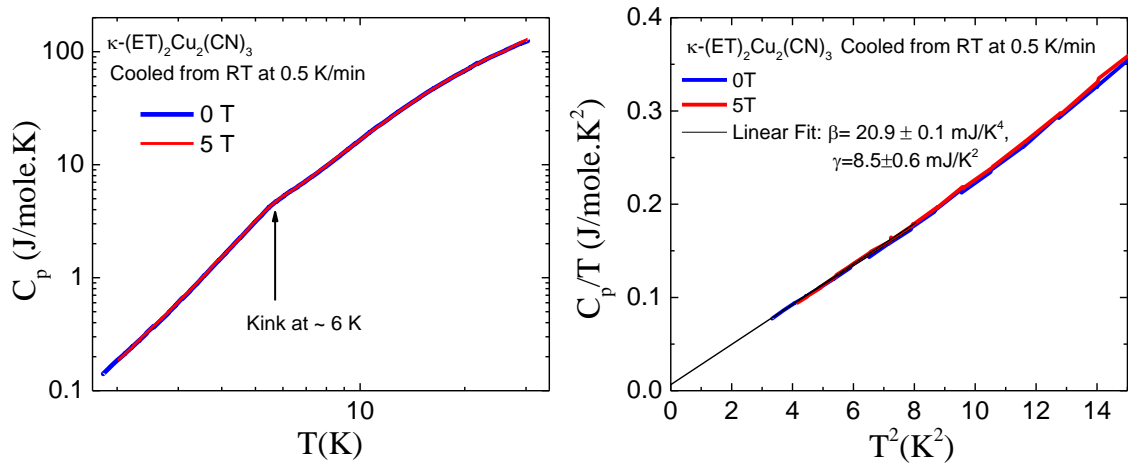


Figure 6.2: a) Plot of C_p vs T of κ -(ET)₂ Cu₂ (CN)₃ at two fields. b) Plot of $C_p T^{-1}$ vs T^2 at low temperatures. The data was fitted to a line with the slope equals to the lattice contribution, β , and the intercept is the Sommerfeld coefficient, γ

CHAPTER 6. HEAT CAPACITY MEASUREMENTS

Fig.6.3 shows the effect of cooling rates on the different contributions to heat capacity. Heat capacity was measured on warming after cooling samples at rates 0.1 K/min, 0.5K/min and 2 K/min. Measurements at cooling rates 0.1 K/min and 2 K/min were measured using a 0.2 mg sample from 2K to 60 K. A larger sample, 0.38 mg, was used in the cooling cycle at 0.5 K/min. All measurements were taken at 0 Oe. Fig 6.3 a) is a plot of C_p/T vs T to show the effect of cooling rates on the general shape of the heat capacity curve. The plot doesn't show any variation in the shape or location of the kink. Also, no variation in the curve shape means no change in the lattice contribution. The inset is a plot of C_p/T^3 vs T to magnify the kink at 6K; there is a slight change in the 0.5K/min cooling rate. However, because there is no change between the data taken at cooling rates 0.1 K/min and 2K/min, such change could be considered within error bars. Fig. 6.3 b) shows the low temperature contribution for different cooling rates as C_p/T vs T^2 . The low temperature data was fitted to a line with slope equal to the cubic term (lattice contribution), and intercept equal to the linear term corresponding to spinon contribution. The lattice contribution in all three cooling rates is equal to $\sim 25mJ/mole.K^4$. The linear term due to the spinon contribution agree within the error at cooling rates 0.1K/min and 2K/min. The value however, is lower than that reported in literature.²⁰ However, at 0.5K/min, the linear term is larger than other measurements. However, since there is no pattern whether increasing or decreasing values for the linear term with cooling rates, no conclusion could be derived. DR measurements at different cooling rates could help draw conclusive results.

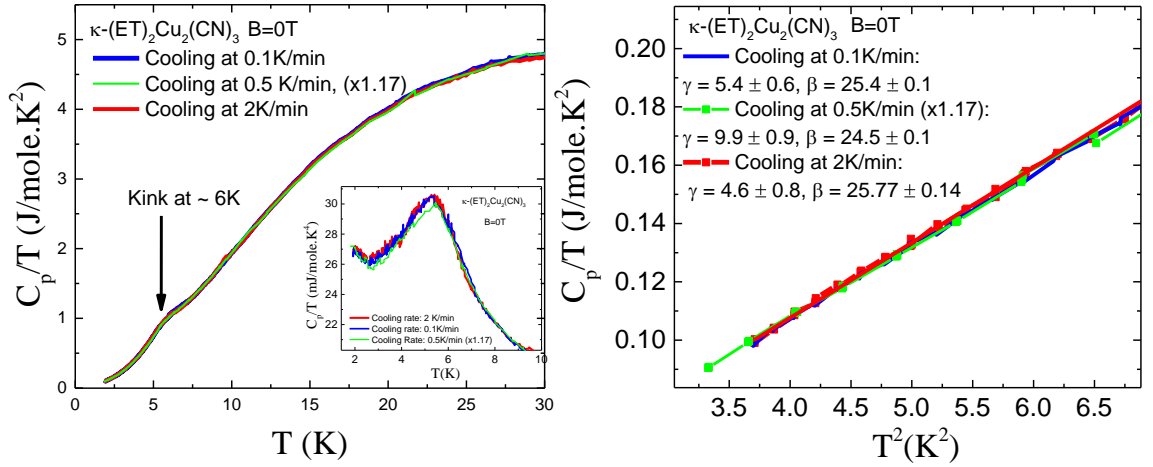


Figure 6.3: a) Plot of C_p/T vs T of $\kappa\text{-(ET)}_2\text{Cu}_2(\text{CN})_3$ at cooling rates: 0.1 K/min (blue), 0.5 K/min (green) and 2 K/min (red). Inset is a plot of C_p/T^3 vs T . b) Plot of C_p/T vs T^2 at cooling rates 0.1 K/min (blue), 0.5 K/min (green) and 2 K/min (red). No significant difference is detected.

6.1.2 $\kappa\text{-(ET)}_2\text{Hg(SCN)}_2\text{Br}$

We took heat capacity measurements of three samples of $\kappa\text{-(ET)}_2\text{Hg(SCN)}_2\text{Br}$. The three samples had masses 0.8 mg, 0.6 mg and 0.92 mg. Measurements were taken on warming at fields 0 T and 5T. Also different cooling rates were tested. Fig. 6.4 a) is a plot of C_p/T vs T at 0 Oe of samples cooled at 0.5K/min in zero field. The inset is a magnification of the feature (anomaly) at 80 K where MIT takes place. This anomaly is expected to be due to the phase transition. Further testing of the phase transition was taken using a technique on ppms where much longer heat pulse was used. Fig. 6.4 b) is a plot of C_p/T vs T^2 at 0 T for a sample cooled at 0.5 K/min. The coefficient of the linear term (Sommerfeld coefficient) is around $7.6\text{mJK}^{-2}\text{mol}^{-1}$ compared to $9\text{mJK}^{-4}\text{mol}^{-1}$ in $\kappa\text{-(ET)}_2\text{Cu}_2(\text{CN})_3$. The lattice contribution $\beta = 18.4\text{mJK}^{-4}\text{mol}^{-1}$ was measured by fitting the data to βT^3 term.

CHAPTER 6. HEAT CAPACITY MEASUREMENTS

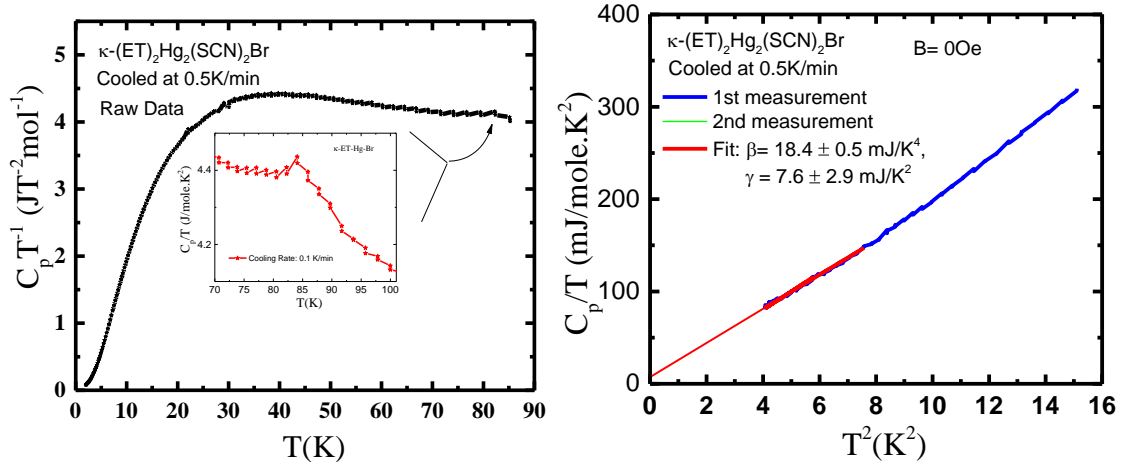


Figure 6.4: a) Plot of C_p/T vs T of $\kappa\text{-(ET)}_2\text{Hg}(\text{SCN})_2\text{Br}$. Inset is a magnification of the kink at $\sim 80\text{K}$. b) Plot of $C_p T^{-1}$ vs T^2 at low temperatures. The data was fitted to a line with the slope equals to the lattice contribution, β , and the intercept is the Sommerfeld coefficient, γ

Fig. 6.5 is plot of the heat capacity of $\kappa\text{-(ET)}_2\text{Hg}(\text{SCN})_2\text{Br}$ under 0T and 5T to compare effect of field on different contributions. Fig. 6.5 a) is a log-log plot of C_p vs T and no significant change is taking place. Fig. 6.5 b) is a plot of C_p/T vs T^2 at 0T and 5T . Because few data points were taken, no conclusion could be derived. DR measurements however, shows the effect of field on the linear terms that correspond to spinon excitations.

Fig. 6.6 shows the effect of cooling rate on the lattice contribution, spinon contribution and phase transition. Fig. 6.6 a) is plot of C_p/T vs T at cooling rates 0.1K/min (blue), 0.5K/min (green) and 2K/min (red). The phase transition at around 80K doesn't show any change in shape or temperature at either 0.1K/min or 2K/min . Fig. 6.6 b) is a log-log plot of C_p vs T that shows a change in the low temperature data between 2K and 5K where at higher cooling rates, there is an additional contribution that is fitted in Fig. 6.6 c). The inset of Fig. 6.6 b) is a plot of C_p/T^3 vs T that also confirms the same result; slight change

CHAPTER 6. HEAT CAPACITY MEASUREMENTS

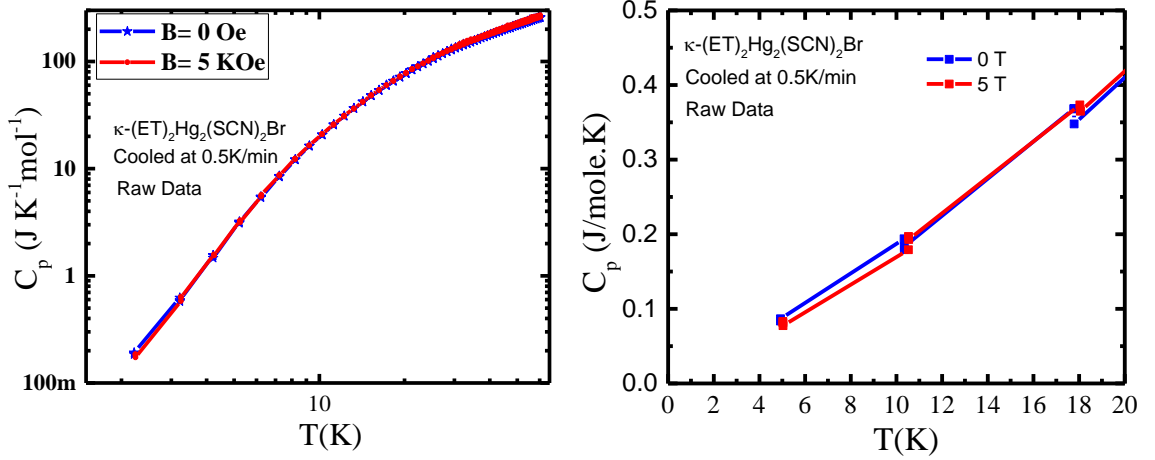


Figure 6.5: a) Log-Log plot of C_p vs T of $\kappa\text{-(ET)}_2\text{Hg}_2(\text{SCN})_2\text{Br}$ at two fields. b) Plot of $C_p T^{-1}$ vs T^2 at low temperatures. The data was fitted to a line with the slope equals to the lattice contribution, β , and the intercept is the Sommerfeld coefficient, γ

in the low temperature behavior. A plot of low temperature data from $T=2\text{K}$ to $T=4.5 \text{ K}$ is shown in Fig. 6.6 c). The plot of C_p/T vs T^2 is fitted linearly to extract the lattice contribution (slope) and spinon excitation (intercept). The intercept value does get larger with increasing the cooling rate from 1 mJ/mole.K^2 at 0.1 K/min to 13.4 mJ/mole.K^2 at 2 K/min . The lattice term doesn't show any change and has value of $\sim 19 \text{ mJ K}^{-4} \text{mol}^{-1}$.

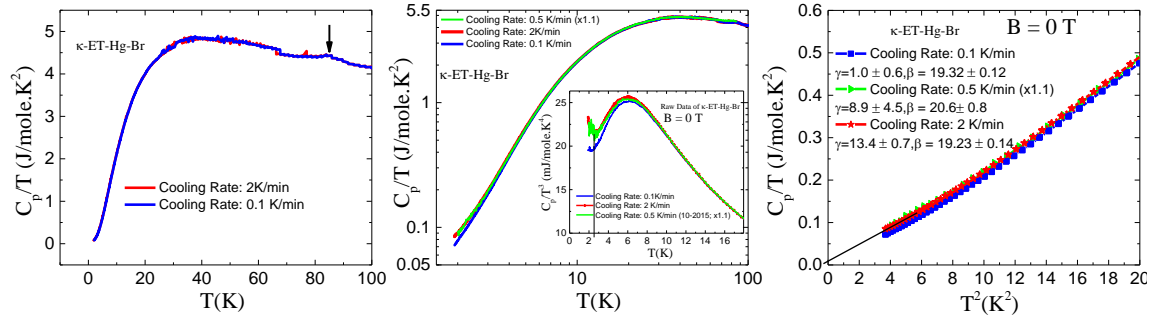


Figure 6.6: a) Plot of C_p/T vs T of $\kappa\text{-(ET)}_2\text{Hg}_2(\text{SCN})_2\text{Br}$ at cooling rates 2 K/min (red) and 0.1 K/min (blue). b) Log-Log plot of C_p/T vs T for cooling rates 0.1 K/min (blue), 0.5 K/min (green) and 2 K/min (red). The inset is a plot of C_p/T^3 vs T . c) Low temperature plot of C_p/T vs T^2 . The data was fitted to a line with the slope equals to the lattice contribution, β , and the intercept is the Sommerfeld coefficient, γ .

6.1.3 κ -(ET)₂ Hg(SCN)₂ Cl

We measured heat capacities of few samples of κ -(ET)₂ Hg(SCN)₂ Cl with masses 0.56 mg, 1.11 mg and 0.93 mg at different cooling rates and under few values of magnetic field. The results of C_p/T vs T are shown in fig.6.7a). There is an anomaly at 30 K (circled) that is a sign of a MIT phase transition. Interestingly the same feature at 80K found in the heat capacity of κ -(ET)₂ Hg(SCN)₂ Br also appears in κ -(ET)₂ Hg(SCN)₂ Cl and this could be attributed to CH₂ ordering. The inset magnifies both features. Fig.6.7b) is a plot of C_p/T vs T^2 at low temperate that was fitted linearly. The fit showed consistently that κ -(ET)₂ Hg(SCN)₂Cl has no linear term and the low temperature behavior is dominated by lattice contributions $\sim T^3$.

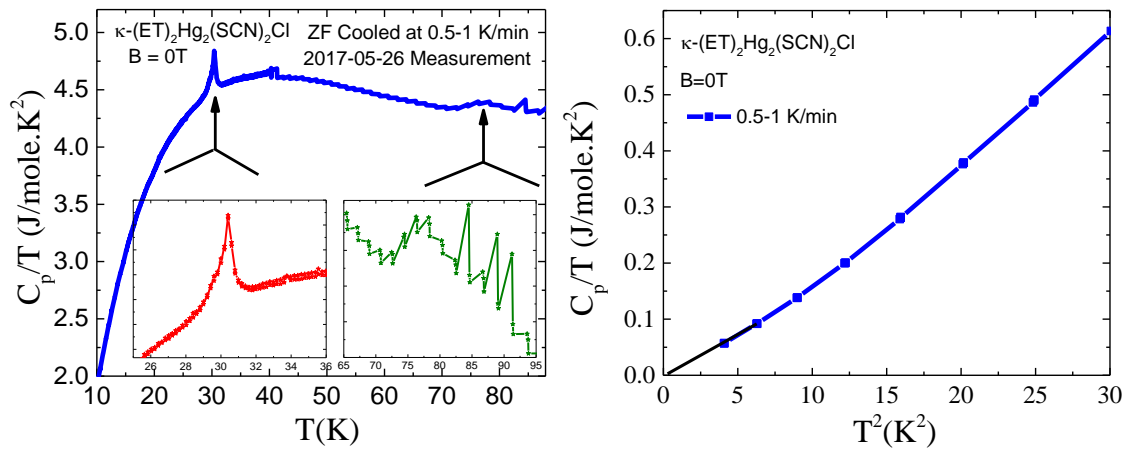


Figure 6.7: a) Plot of C_p/T vs T of κ -(ET)₂ Hg(SCN)₂Cl. Inset is a magnification of the anomaly at 30K and ~ 80 K. b) Plot of $C_p T^{-1}$ vs T^2 at low temperatures. The data was fitted to a line with the slope equals to the lattice contribution, β , and the intercept is the Sommerfeld coefficient, γ

Fig.6.8 a) and b) are plots of the anomaly due to phase transition at 30K. The measurements were done on warming (red) and cooling (blue) to check for hysteresis. No

CHAPTER 6. HEAT CAPACITY MEASUREMENTS

hysteresis was detected whether the sample was cooled down at 10 K/min (plot a) or at 0.1 K/min (plot b). Fig. 6.9 is a plot of the heat capacity of κ -(ET)₂ Hg(SCN)₂Cl under 0T

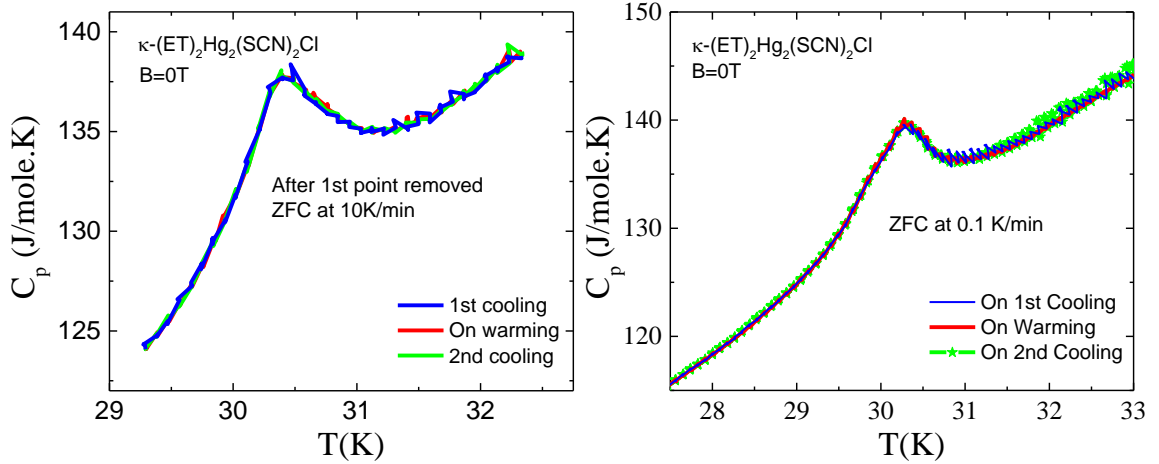


Figure 6.8: a) Plot of C_p vs T of κ -(ET)₂ Hg(SCN)₂Cl at cooling rate 10K/min. Measurements were done on cooling (blue) and warming (red). b) Plot of C_p vs T of κ -(ET)₂ Hg(SCN)₂Cl at cooling rate 0.1K/min.

(blue), 5T (green) and 9T (red) to study effect of magnetic field on different heat capacity components. Fig. 6.9 a) is a log-log plot of C_p vs T and no significant change is taking place. Fig. 6.9 b) is a plot of C_p/T vs T^2 at 0T, 5T and 9T. No changes was detected due to field at low temperature, with $\sim T^3$ behavior dominating the contribution to heat capacity.

Fig. 6.10 shows the effect of cooling rate on the lattice contribution and phase transition. Fig. 6.10 a) is plot of C_p/T vs T at cooling rates 10K/min (blue) and 0.5K/min (red). The phase transition at around 30 K shows slight change in shape. The effect is magnified in inset of Fig. 6.10a). Fig. 6.10b) is a log-log plot of C_p vs T that shows no change in the low temperature behavior. The inset of Fig. 6.10 b) is a plot of C_p/T^3 vs T that also confirms the same result with no change in phonon contribution. A plot of low temperature data

CHAPTER 6. HEAT CAPACITY MEASUREMENTS

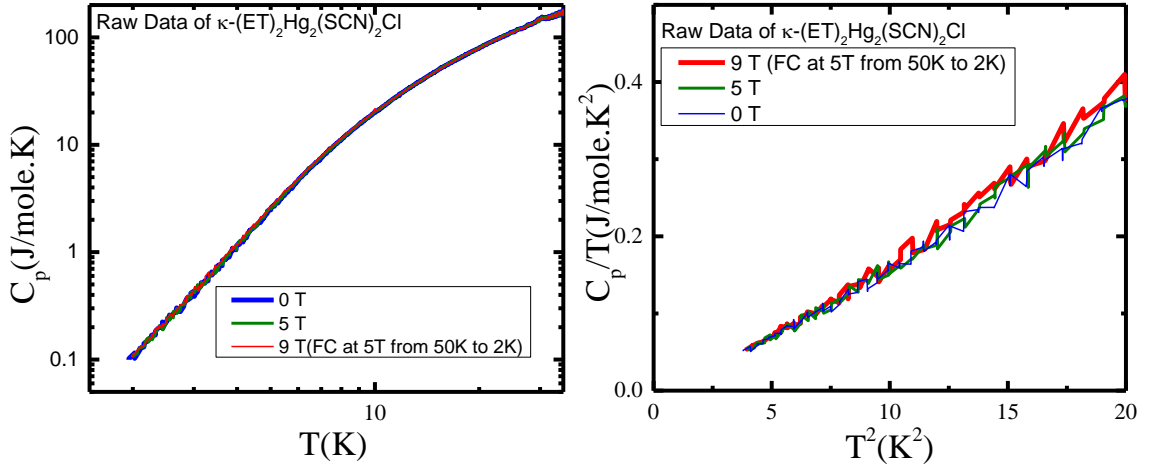


Figure 6.9: a) Log-Log plot of C_p vs T of κ -(ET)₂ $\text{Hg}(\text{SCN})_2\text{Cl}$ at two fields. b) Plot of $C_p T^{-1}$ vs T^2 at low temperatures. The data was fitted to a line with the slope equals to the lattice contribution, β , and the intercept is the Sommerfeld coefficient, γ

from $T=2\text{K}$ to $T=4.5\text{ K}$ is shown in Fig. 6.10 c). The plot of C_p/T vs T^2 is fitted linearly to extract the lattice contribution (slope) and any linear contribution if existed. The intercept value is zero at all cooling rates that might imply that no disorder or glassiness takes place.

The lattice term doesn't show any change and has value of $\sim 20\text{mJ}K^{-4}\text{mol}^{-1}$.

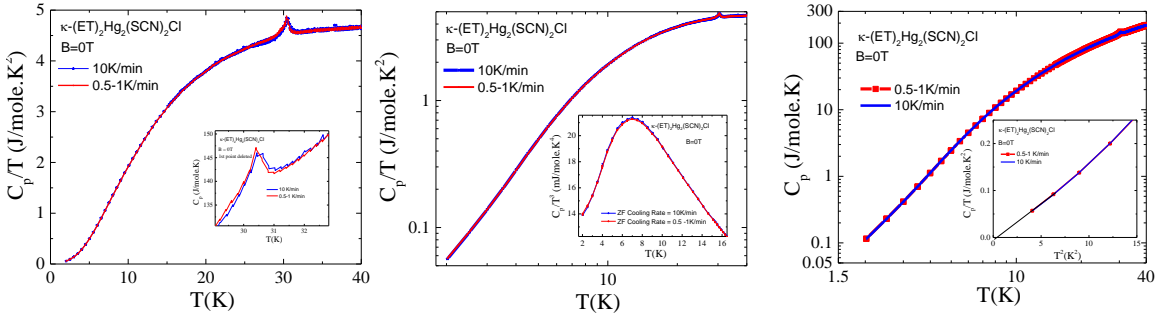


Figure 6.10: a) Plot of C_p/T vs T of κ -(ET)₂ $\text{Hg}(\text{SCN})_2\text{Cl}$ at cooling rates 0.5K/min (red) and 10 K/min (blue). The inset is a close up of the anomaly due to phase transition at 30 K. b) Log-Log plot of C_p/T vs T for cooling rates 0.5K/min (red) and 10 K/min (blue). Inset is a plot of C_p/T^3 vs T for cooling rates 0.5K/min (red) and 10K/min (blue). c) Low temperature plot of C_p/T vs T^2 . The data was fitted to a line with the slope equals to the lattice contribution, β , and the intercept is the Sommerfeld coefficient, γ .

CHAPTER 6. HEAT CAPACITY MEASUREMENTS

Fig.6.11a) is a plot of C_p vs T to compare the shape of the anomaly at 30 K at different cooling rates; 10K/min (red curve) and 0.1 K/min (black curve). There is a slight shift in the temperature and shape of the anomaly that is still under investigation. Fig.6.11b) is a plot where one of the curves was shifted in temperature to superimpose the two curves; there is slight change at temperatures higher than the MIT transition. Also, it is obvious that the anomaly has a complex shape with what looks like a double peak. The implication of which is still under study.

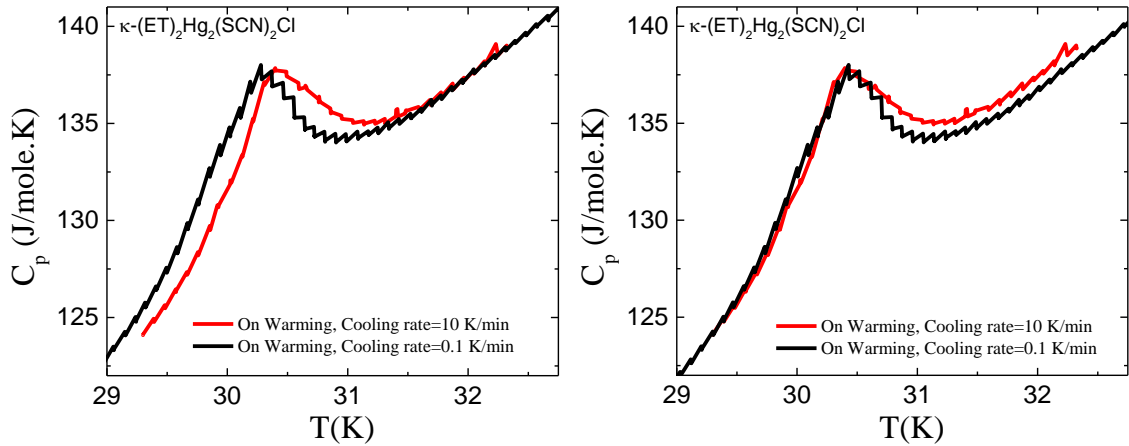


Figure 6.11: a) Plot of C_p vs T of κ -(ET)₂ Hg(SCN)₂ Cl of the anomaly at 30 K at cooling rates 10K/min (red) and 0.1K/min (black). b) Same plot as a) with the two curves superimposed.

6.2 Conclusion

In this section I will compare the results of heat capacity measurements of the three materials: κ -(ET)₂ Hg(SCN)₂Br (blue), κ -(ET)₂ Hg(SCN)₂Cl (green) and κ -(ET)₂ Cu₂ (CN)₃ (red). Heat capacity of these materials generally have $\sim T^3$ dependence at low tempera-

CHAPTER 6. HEAT CAPACITY MEASUREMENTS

ture. It was shown that all three materials have similar lattice contribution in the range of $\beta = 18.4 - 24mJK^{-4}mol^{-1}$. The heat capacity curve was fit using two kinds of Debye phonons at two Debye temperatures: $T_{D1} \sim 440K$ and $T_{D2} \sim 101K$. In fig. 6.12 a) the anomaly at 6K distinguishes κ -(ET)₂ Cu₂ (CN)₃ from the isostructural materials κ -(ET)₂ Hg(SCN)₂Br and κ -(ET)₂ Hg(SCN)₂Cl. It is hypothesized that the kink at 6K signifies the onset of spin liquid state. Heat capacity of κ -(ET)₂ Hg(SCN)₂Cl shows the anomaly at 30K due to the transition from metallic state to charge ordered insulating transition. Both κ -(ET)₂ Hg(SCN)₂Br and κ -(ET)₂ Hg(SCN)₂Cl have an anomaly at $\sim 80K$ that could be attributed to CH_2 ordering. Fig. 6.12b) shows a feature at around 10 K that is still under investigation.

Fig. 6.12 c) compares the linear term of all three materials; κ -(ET)₂ Hg(SCN)₂Br and κ -(ET)₂ Cu₂ (CN)₃ show pronounced linear term at very low temperatures. The coefficient of the linear term (Sommerfeld coefficient) is around $7.6mJK^{-2}mol^{-1}$ compared to $9mJK^{-4}mol^{-1}$ in κ -(ET)₂ Cu₂ (CN)₃. Generally, conduction electrons are the major source of a linear term in heat capacity measurements, however, because these compounds are Mott insulators at such low temperatures, conduction electron contribution is ruled out. Another reason for this linear term is believed to be due to spinons. The linear term doesn't change under the effect of magnetic field in both materials. However, κ -(ET)₂ Hg(SCN)₂Br shows more pronounced decrease of the Sommerfeld coefficient as the cooling rate is decreased, see fig.6.13b) and c). That could indicate more disorder or glassiness at low temperatures.

CHAPTER 6. HEAT CAPACITY MEASUREMENTS

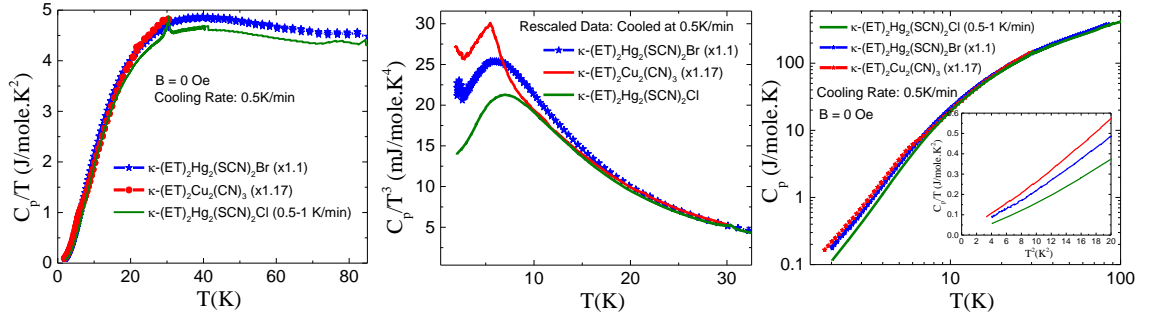


Figure 6.12: a) Plot of C_p/T vs T of κ -(ET)₂ Hg(SCN)₂Br (blue), κ -(ET)₂ Hg(SCN)₂Cl (green) and κ -(ET)₂ Cu₂(CN)₃ (red). b) Plot of C_p/T^3 vs T of all three materials. c) Log-Log plot of C_p vs T of all three materials; the inset is a plot of C_p/T vs T^2 at very low temperatures.

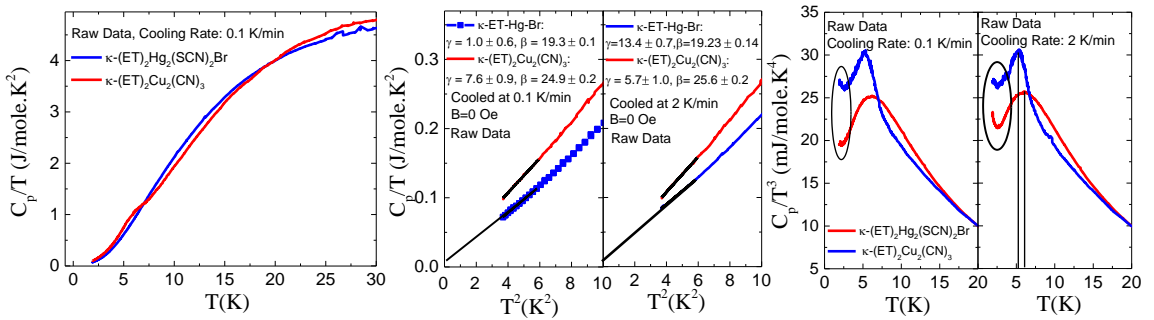


Figure 6.13: a) Plot of C_p/T vs T of κ -(ET)₂ Hg(SCN)₂Br (blue) and κ -(ET)₂ Cu₂(CN)₃ (red). b) plot of C_p/T vs T^2 at very low temperatures of both materials cooled at 0.1K/min (left panel) and at 2K/min(right panel). c) Plot of C_p/T^3 vs T of both materials cooled at 0.1K/min (left panel) and at 2K/min(right panel)

Chapter 7

Summary

We studied two isostructural materials to determine their ground states and understand the mechanism of such states. Both materials belong to the larger class of organic Mott insulators. However, their MIT transition proved elusive and much more interesting than simple Mott transition. The Materials are quasi-two-dimensional materials with triangular lattice that renders them very interesting to study effects of frustration and correlation. We studied their charge degree of freedom using Raman spectroscopy and phase transition using heat capacity. Raman proved to be the best way to study the charge dynamics of these systems; for κ -Hg-Br, we detected charge fluctuations within dimers below 80 K that lead to the increase in the width of the charge sensitive vibrational mode ν_2 . By fitting our data to two-site jump model we could calculate the frequency of the dipole fluctuations. At that frequency we detected evidence of collective behavior of charge fluctuations that further supports our analysis of ν_2 . Our results proved to be the first experimental finding

CHAPTER 7. SUMMARY

of quantum dipole liquid. Also, that behavior of charge fluctuation could explain the lack of evidence of magnetic ordering. Our Raman analysis of the low frequency behavior didnt detect any signs of magnetic ordering in the form of wide bands within range of 80-400 cm^{-1} . This could be explained by the assumption that charge and spins are coupled and as a result, the charge fluctuation/dynamics suppresses any ordering of spins. Also, our heat capacity measurement detected an interesting linear term at very low temperature. That linear term could be explained as spinon excitations in light of our Raman results.

κ -Hg-Cl proved to be very interesting; first it is unusual for the dimerized κ -phase to be charge ordered. Second, we recently discovered that at very low temperatures the material crosses over from a charge ordered state to re-entrant new phase. Raman spectrum at low temperatures shows that the charge sensitive mode ν_2 gain spectral weight as we lower the temperature. Also, the difference between the frequencies of the charge rich mode ν_{2A} and charge poor mode ν_{2B} gets smaller, implying that the charge disproportionation gets lesser. The fits suggest that we have at least three charges on the lattice instead of two charges (0.6e and 0.4e) in the charge ordered state. Such state is still under investigation with very interesting possible explanations in light of new results from other experiments. Heat capacity measurements did not detect signs of phase transition at the crossover temperature. No cooling rate dependence was detected whether in Raman or heat capacity measurements. Also, magnetic Raman studies didnt detect any evidence of magnetic ordering which is supported by very recent results.³⁴ All these results point towards frustration effects.

In conclusion, Raman was very useful in studying charge degree of freedom and mag-

CHAPTER 7. SUMMARY

netic behavior of these systems; we detected new ground states that could illuminate new mechanism by which magnetic frustration takes place. κ -Hg-Br was found to be a quantum dipole liquid and its iso-structure shows signs of frustration at very low temperature that disrupts the charge ordered state. The fact that κ -Hg-Cl and κ -Hg-Br are isostructural materials could help us understand the consequence of chemical pressure and thus, effect of transfer integrals and other parameters on frustration. That could help understand different mechanism of frustration and exotic new phases of matter, and advance future material design.

Bibliography

- [1] N. Drichko, R. Beyer, E. Rose, M. Dressel, J. A. Schlueter, S. A. Turunova, E. I. Zhilyaeva, and R. N. Lyubovskaya, “Metallic state and charge-order metal-insulator transition in the quasi-two-dimensional conductor κ -(bedt-ttf)₂hg(scn)₂cl,” *Phys. Rev. B*, vol. 89, p. 075133, Feb 2014. [Online]. Available: <http://link.aps.org/doi/10.1103/PhysRevB.89.075133>
- [2] H. C. Kandpal, I. Opahle, Y.-Z. Zhang, H. O. Jeschke, and R. Valentí, “Revision of model parameters for κ -type charge transfer salts: An ab initio study,” *Phys. Rev. Lett.*, vol. 103, p. 067004, Aug 2009,
- [3] C. Hotta, “Theories on frustrated electrons in two-dimensional organic solids,” *Crystals*, vol. 2, no. 3, pp. 1155–1200, 2012.
- [4] L. Balents, “Spin liquids in frustrated magnets,” *Nature*, vol. 464, no. 7286, pp. 199–208, 2010,
- [5] M. Holt, B. J. Powell, and J. Merino, “Spin-liquid phase due to competing classical

BIBLIOGRAPHY

- orders in the semiclassical theory of the heisenberg model with ring exchange on an anisotropic triangular lattice,” *Physical Review B*, vol. 89, no. 174415, 2014.
- [6] C. Hotta, “Quantum electric dipoles in spin-liquid dimer mott insulator κ - $\text{et}_2\text{cu}_2(\text{cn})_3$,” *Physical Review B*, vol. 82, no. 24, p. 241104, 2010.
- [7] Drichko, “Synthesis, crystal structure and properties,” *Synth. Met.*, vol. 1905, pp. 55–57, 1993.
- [8] E. Gati, J. K. Fischer, P. Lunkenheimer, D. Zielke, S. Khler, F. Kolb, H.-A. Krug von Nidda, S. M. Winter, H. Schubert, J. A. Schlueter, H. O. Jeschke, R. Valent, and M. Lang, “Evidence for electronically driven ferroelectricity in a strongly correlated dimerized bedt-ttf molecular conductor,” *Phys. Rev. Lett.*, vol. 120, p. 247601, 2018.
- [9] B. J. Powell and R. H. McKenzie, “Strong electronic correlations in superconducting organic charge transfer salts,” *Journal of Physics: Condensed Matter*, vol. 18, no. 45, 2006.
- [10] T. Ivek, R. Beyer, S. Badalov, M. Čulo, S. Tomić, J. A. Schlueter, E. I. Zhilyaeva, R. N. Lyubovskaya, and M. Dressel, “Metal-insulator transition in the dimerized organic conductor $\kappa - (\text{BEDT-TTF})_2\text{Hg}(\text{SCN})_2\text{Br}$,” *Phys. Rev. B*, vol. 96, p. 085116, Aug 2017. [Online]. Available: <https://link.aps.org/doi/10.1103/PhysRevB.96.085116>
- [11] P. Vandenabeele, *Practical Raman spectroscopy: An Introduction*. Wiley, 2013.

BIBLIOGRAPHY

- [12] K. Yakushi, “Infrared and raman studies of charge ordering in organic conductors, bedt-ttf salts with quarter-filled bands,” *Crystals*, vol. 2, no. 3, pp. 1291–1346, 2012.
- [13] T. Yamamoto, M. Uruichi, K. Yamamoto, K. Yakushi, A. Kawamoto, and H. Taniguchi, “Examination of the charge-sensitive vibrational modes in bis (ethylenedithio) tetrathiafulvalene,” *The Journal of Physical Chemistry B*, vol. 109, no. 32, pp. 15 226–15 235, 2005,
- [14] W. Hayes and R. Loudon, *Scattering of Light by Crystals*. Dover, New York, 2004.
- [15] M. E. Valentine, “Inelastic light scattering signatures of magnetic ordering and topological properties in strongly-correlated electron systems,” *PhD dissertation*, 2017.
- [16] Y. Nakamura, N. Yoneyama, T. Sasaki, T. Tohyama, A. Nakamura, and H. Kishida, “Magnetic raman scattering study of spin frustrated systems, κ -(bedt-ttf)₂ x,” *Journal of the Physical Society of Japan*, vol. 83, no. 7, p. 074708, 2014,
- [17] F. Vernay, T. Devereaux, and M. Gingras, “Raman scattering for triangular lattices spin-1/2 heisenberg antiferromagnets,” *Journal of Physics: Condensed Matter*, vol. 19, no. 14, p. 145243, 2007,
- [18] J. M. D. Coey, *Magnetism and Magnetic Materials*. Cambridge University Press, NY, 2009.
- [19] Q. Design, *Physical Property Measurement System: Heat Capacity Option Users Manua*. Quantum Design, 2004.

BIBLIOGRAPHY

- [20] S. Yamashita, Y. Nakazawa, M. Oguni, Y. Oshima, H. Nojiri, Y. Shimizu, K. Miyagawa, and K. Kanoda, “Thermodynamic properties of a spin-1/2 spin-liquid state in a κ -type organic salt,” *Nature Physics*, vol. 4, no. 6, pp. 459–462, 2008,
- [21] S. Dayal, R. T. Clay, H. Li, and S. Mazumdar, “Paired electron crystal: Order from frustration in the quarter-filled band,” *Phys. Rev. B*, vol. 83, p. 245106, Jun 2011,
- [22] B. J. Powell, “An introduction to effective low-energy hamiltonians in condensed matter physics and chemistry,” *arXiv:0906.1640v7*, 2010.
- [23] P. W. Anderson, “Resonating valence bonds: A new kind of insulator?” *Mater. Res. Bull.*, vol. 8, no. 2, 1973.
- [24] ———, “The resonating valence bond state in La_2CuO_4 and superconductivity,” *Science* 235 (4793), vol. 235 (4793), no. 11961198, 1987.
- [25] B. Bernu, C. Lhuillier, and L. Pierre, “Signature of nel order in exact spectra of quantum antiferromagnets on finite lattices,” *Phys. Rev. Lett.*, vol. 69, no. 2590-2593, 1992.
- [26] L. Capriotti, A. E. Trumper, and S. Sorella, “Long-range nel order in the triangular heisenberg model,” *Phys. Rev. Lett.*, vol. 82, no. 3899-3902, 1999.
- [27] Y. Kurosaki, Y. Shimizu, K. Miyagawa, K. Kanoda, and G. Saito, “Mott transition from a spin liquid to a fermi liquid in the spin-frustrated organic conductor κ -(bedt-ttf) $_2\text{Cu}_2(\text{cn})_3$,” *Phys. Rev. Lett.*, vol. 95, p. 177001, Oct 2005,

BIBLIOGRAPHY

- [28] F. Pratt, P. Baker, S. Blundell, T. Lancaster, S. Ohira-Kawamura, C. Baines, Y. Shimizu, K. Kanoda, I. Watanabe, and G. Saito, “Magnetic and non-magnetic phases of a quantum spin liquid,” *Nature*, vol. 471, no. 7340, pp. 612–616, 2011,
- [29] Y. Shimizu, K. Miyagawa, K. Kanoda, M. Maesato, and G. Saito, “Spin liquid state in an organic mott insulator with a triangular lattice,” *Physical review letters*, vol. 91, no. 10, p. 107001, 2003.
- [30] A. Lebed, *The Physics of Organic Superconductors and Conductors*. Springer Series in Materials Science, 2008, vol. 110.
- [31] H. O. Jeschke, H. C. .Kandpal, I. Opahle, Y.-Z. Zhang, and R. Valenti, “First principles determination of the model parameters in κ -et₂cu₂(cn)₃,” *Physica B*, vol. 405, no. S224S228, 2010.
- [32] M. Aldoshina, R. Lyubovskaya, S. Konovalikhin, O. Dyachenko, G. Shilov, M. Makova, and R. Lyubovskii, “A new series of et-based organic metals: synthesis, crystal structure and properties,” *Synthetic metals*, vol. 56, no. 1, pp. 1905–1909, 1993.
- [33] S. Yasin, E. Rose, M. Dumma, N. Drichko, M. Dressel, J. A. Schlueter, E. I. Zhilyaeva, S. Torunova, and R. N. Lyubovskaya, “Electronic and magnetic studies of κ -(bedt-ttf)₂hg(sc_n)₂cl,” *Physica B*, vol. 407, p. 16891691, 2012.
- [34] “Private communications at grc 2018.”

BIBLIOGRAPHY

- [35] M. Hemmida, H. A. K. von Nidda, B. Miksch, L. L. Samoilenko, A. Pustogow, S. Widmann, A. Henderson, T. Siegrist, J. A. Schlueter, A. Loidl, and M. Dressel, “Weak ferromagnetism and glassy state in κ -(bedt-ttf)₂hg(scn)₂br,” *arXiv:1710.04028v2 [cond-mat.str-el]*, 2018.
- [36] M. Dressel, , and N. Drichko, “Optical properties of two-dimensional organic conductors: Signatures of charge ordering and correlation effects,” *Chemical Reviews*, vol. 104, no. 11, pp. 5689–5716, 2004,
- [37] N. Drichko, R. Hackl, and J. A. Schlueter, “Antiferromagnetic fluctuations in a quasi-two-dimensional organic superconductor detected by raman spectroscopy,” *Phys. Rev. B*, vol. 92, p. 161112, Oct 2015,
- [38] T. P. Devereaux and R. Hackl, “Inelastic light scattering from correlated electrons,” *Reviews of modern physics*, vol. 79, no. 1, p. 175, 2007,
- [39] D. Halliday and R. Resnick, *Fundamentals of Physics*. Wiley, 2013.
- [40] C. A. Kennedy, M. Stancescu, R. A. Marriott, and M. A. White, “Recommendations for accurate heat capacity measurements using a quantum design physical property measurement system,” *Cryogenics*, vol. 47, p. 107112, 2007.
- [41] M. Naka and S. Ishihara, “Quantum melting of magnetic order in an organic dimer mott-insulating system,” *Phys. Rev. B*, vol. 93, p. 195114, May 2016. [Online]. Available: <http://link.aps.org/doi/10.1103/PhysRevB.93.195114>

BIBLIOGRAPHY

- [42] N. Y. Yao, M. P. Zaletel, D. M. Stamper-Kurn, and A. Vishwanath, “A quantum dipolar spin liquid,” *arXiv preprint arXiv:1510.06403*, 2015.
- [43] S. Rowley, L. Spalek, R. Smith, M. Dean, M. Itoh, J. Scott, G. Lonzarich, and S. Saxena, “Ferroelectric quantum criticality,” *Nat. Phys.*, vol. 10, pp. 367–372, 2014.
- [44] S.-P. Shen, J.-C. Wu, J.-D. Song, X.-F. Sun, Y.-F. Yang, Y.-S. Chai, D.-S. Shang, S.-G. Wang, J. F. Scott, and Y. Sun, “Quantum electric-dipole liquid on a triangular lattice,” *Nature communications*, vol. 7, 2016.
- [45] K. Yakushi, K. Yamamoto, T. Yamamoto, Y. Saito, and A. Kawamoto, “Raman spectroscopy study of charge fluctuation in the spin-liquid candidate κ -(bedt-ttf)₂cu₂(cn)₃,” *Journal of the Physical Society of Japan*, vol. 84, no. 8, p. 084711, 2015,
- [46] K. Sedlmeier, S. Elsässer, D. Neubauer, R. Beyer, D. Wu, T. Ivek, S. Tomić, J. A. Schlueter, and M. Dressel, “Absence of charge order in the dimerized κ -phase bedt-ttf salts,” *Phys. Rev. B*, vol. 86, p. 245103, Dec 2012. [Online]. Available: <http://link.aps.org/doi/10.1103/PhysRevB.86.245103>
- [47] R. Lyubovskii, R. Lyubovskaya, and O. Dyachenko, “Physical properties of some et-based organic metals and superconductors with mercury containing anions,” *Journal de Physique I*, vol. 6, no. 12, pp. 1609–1630, 1996,
- [48] Y. Kim, X. Chen, Z. Wang, J. Shi, I. Miotkowski, Y. Chen, P. Sharma,

BIBLIOGRAPHY

- A. Lima Sharma, M. Hekmaty, Z. Jiang *et al.*, “Temperature dependence of raman-active optical phonons in Bi_2Se_3 and Sb_2Te_3 ,” *Applied Physics Letters*, vol. 100, no. 7, p. 071907, 2012.
- [49] A. Girlando, M. Masino, J. A. Schlueter, N. Drichko, S. Kaiser, and M. Dressel, “Charge-order fluctuations and superconductivity in two-dimensional organic metals,” *Phys. Rev. B*, vol. 89, p. 174503, May 2014. [Online]. Available: <http://link.aps.org/doi/10.1103/PhysRevB.89.174503>
- [50] M. Maksimuk, K. Yakushi, H. Taniguchi, K. Kanoda, and A. Kawamoto, “The c-c stretching vibrations of κ -(bedt-ttf) $_2\text{Cu}[\text{N}(\text{CN})_2]\text{Br}$ and its isotope analogues,” *Journal of the Physical Society of Japan*, vol. 70, no. 12, pp. 3728–3738, 2001.
- [51] N. Perkins and W. Brenig, “Raman scattering in a heisenberg $s = \frac{1}{2}$ antiferromagnet on the triangular lattice,” *Phys. Rev. B*, vol. 77, p. 174412, May 2008,
- [52] Y. Nakamura, T. Hiramatsu, Y. Yoshida, G. Saito, and H. Kishida, “Optical properties of a quantum spin liquid candidate material, κ -(bedt-ttf) $_2\text{Ag}_2(\text{CN})_3$,” *Journal of the Physical Society of Japan*, vol. 86, no. 1, p. 014710, 2016.
- [53] N. Drichko, M. Dumm, D. Faltermeier, M. Dressel, J. Merino, and A. Greco, “Drude weight in quasi-two-dimensional organic conductors close to the mott transition: Optical studies of the bandwidth, filling and temperature dependence,” *Physica C: Superconductivity and its applications*, vol. 460, pp. 125–128, 2007.

BIBLIOGRAPHY

- [54] J. Merino, A. Greco, R. H. McKenzie, and M. Calandra, “Dynamical properties of a strongly correlated model for quarter-filled layered organic molecular crystals,” *Phys. Rev. B*, vol. 68, p. 245121, Dec 2003. [Online]. Available: <http://link.aps.org/doi/10.1103/PhysRevB.68.245121>
- [55] M. Dressel, N. Drichko, J. Schlueter, and J. Merino, “Proximity of the layered organic conductors α -(BEDT-TTF)₂mHg(SCN)₄ ($m = \text{K}, \text{NH}_4$) to a charge-ordering transition,” *Phys. Rev. Lett.*, vol. 90, p. 167002, Apr 2003. [Online]. Available: <http://link.aps.org/doi/10.1103/PhysRevLett.90.167002>
- [56] S. Caprara, C. Di Castro, M. Grilli, and D. Suppa, “Charge-fluctuation contribution to the raman response in superconducting cuprates,” *Phys. Rev. Lett.*, vol. 95, p. 117004, Sep 2005. [Online]. Available: <http://link.aps.org/doi/10.1103/PhysRevLett.95.117004>
- [57] V. Malinovsky and A. Sokolov, “The nature of boson peak in raman scattering in glasses,” *Solid state communications*, vol. 57, no. 9, pp. 757–761, 1986.
- [58] G. Chen, L. Balents, and A. P. Schnyder, “Spin-orbital singlet and quantum critical point on the diamond lattice: fesc₂s₄,” *Phys. Rev. Lett.*, vol. 102, p. 096406, Mar 2009. [Online]. Available: <http://link.aps.org/doi/10.1103/PhysRevLett.102.096406>
- [59] Y. Zhou, K. Kanoda, and T.-K. Ng, “Quantum spin liquid states,” *Reviews of Modern Physics*, vol. 89, no. 2, p. 025003, 2017.

BIBLIOGRAPHY

- [60] M. Naka and S. Ishihara, “Magnetoelectric effect in organic molecular solids,” *Scientific reports*, vol. 6, 2016.
- [61] Y. Nakazawa and S. Yamashita, “Thermodynamic properties of κ -(bedt-ttf) 2x salts: Electron correlations and superconductivity,” *Crystals*, vol. 2, no. 3, pp. 741–761, 2012.
- [62] P. Anderson, G. Baskaran, Z. Zou, and T. Hsu, “Resonating–valence-bond theory of phase transitions and superconductivity in La_2CuO_4 -based compounds,” *Physical review letters*, vol. 58, no. 26, p. 2790, 1987.
- [63] B. Powell, E. Kenny, and J. Merino, “Dynamical reduction of the dimensionality of exchange interactions and the spin-liquid phase of κ -(bedt-ttf) 2x,” *Physical Review Letters*, vol. 119, no. 8, p. 087204, 2017.
- [64] A. Löhle, E. Rose, S. Singh, R. Beyer, E. Tafra, T. Ivek, E. Zhilyaeva, R. Lyubovskaya, and M. Dressel, “Pressure dependence of the metal-insulator transition in κ -(bedt-ttf) 2hg (scn) 2cl: optical and transport studies,” *Journal of Physics: Condensed Matter*, vol. 29, no. 5, p. 055601, 2016.

Vita

Nora M. Hassan was born and raised in Egypt. She received a B.S. degree in Computer Science from the American University in Cairo, graduating summa cum laude. She then enrolled in the PhD program of the department of Physics and Astronomy at Johns Hopkins University. Her thesis work has focused on organic Mott Insulators within the context of strongly correlated electron systems. The main experimental technique used was Raman Spectroscopy.